IMAGE RECONSTRUCTION IN ELECTRICAL IMPEDANCE MAMMOGRAPHY

Mengxing TANG

BEng **(Biomed. Eng.) &** ***MPhil*** **(Biomed. Eng.)**

A thesis submitted for the degree of Doctor of Philosophy

3D Imaging & Biomedical Engineering Group
Faculty of Computing Science and Engineering
De Montfort University

March 2003

To my father, mother and beloved wife Li

献给我的父亲，母亲和深爱的妻子凌黎

ABSTRACT

Breast cancer continues to be a leading cause of death in Western countries. One of the most important approaches to reduce this mortality is to detect the cancer as early as possible. Although current diagnostic imaging modalities are able to give useful information for diagnosis, development of new imaging technique is highly desirable in order to detect breast cancer in an earlier stage. This is the motive of the present study of Electrical Impedance Mammography (EIM), which applies Electrical Impedance Tomography (EIT) to image human breasts.

The overall aim of the whole project is to develop impedance imaging techniques and system for early detection of breast cancer. The aim of the studies reported in this thesis is twofold, to investigate methods of improving EIT image quality and the feasibility of EIT in breast cancer detection.

Focusing on these aims the following work is reported:

1) The study of three different image reconstruction algorithms is described. In this work the image reconstruction results are compared and the most appropriate algorithm was chosen for the subsequent study of breast imaging.

2) An investigation of two important factors in EIT image reconstruction, the number of electrodes (NOE) and the number of conductivity basis functions (NOCBF) whose effects on EIT images have yet been studied in detail so far, are described. In this work the image reconstruction is analysed with different combinations of NOE and NOCBF using Singular Value Decomposition (SVD) and spectrum expansion theory. Finally suggestions are given on which configuration could offer better image quality in breast imaging;

3) A comprehensive investigation is reported regarding compatibility of different types of prior information and its effect on an iterative image reconstruction algorithm, based on which a novel method is proposed to improve EIT image quality. This method selects compatible prior information by observing the convergence behaviour of an image reconstruction algorithm. The principle, implementation, and results are detailed. Results indicate the effectiveness of this method.

4) A two-dimensional breast imaging simulation system is introduced. In this work several breast models with different physiological and pathological conditions are made, based on clinical *in vitro* measurements and Cole-Cole model. Images with different current frequencies are reconstructed and analysed. Results indicate the potential of detecting and identifying breast abnormality by EIT.

5) A preliminary study on 3D EIT and 3D electrode placement has been conducted. The mathematic principle and implementation of 3D EIT are described, followed by a study on the sensitivity of boundary measurements to the conductivity changes in a cylindrical object with 2 different types of electrode placement. Suggestions are given on optimal electrode placement in EIT breast imaging.

Finally suggestions are given for future work. These include a) investigating appropriate electrode placement for different applications and corresponding current & voltage patterns; b) incorporating more prior information into EIM image reconstruction; c) designing a more precise 3D breast forward model; and d) investigating appropriate regularization for image reconstruction.

ACKNOWLEDGEMENTS

I would like to express my sincere gratitude to Dr. Wei Wang and Professor Malcolm McCormick for all the help and encouragement they have given so freely during the course of this work.

I would like to convey my special thanks to Dr. Amar Aggoun, Ms. Liya Jiang, Mr. James Wheeler, Mr. Jieqiu Yang, Dr. Li Wang, Mr. Cris Sims, and all other members within 3D Imaging & Biomedical Engineering Group of De Montfort University for their help and assistance.

I would like to express my sincere gratitude to Professor Xiuzhen Dong and Professor Mingxin Qin, School of Biomedical Engineering, Fourth Military Medical University (China) for their continuous moral support on my study.

I'm indebted to Dr. Xinkai Li, Institute of Simulation Sciences, De Montfort University and Dr. Bill Lionheart, Department of Mathematics, UMIST for their invaluable suggestions and help.

I also acknowledge the financial support of De Montfort University and University-UK.

Finally, I am eternally grateful to my family: my father, mother, grand parents, parents-in-law, and especially my wife, whose great love, care, and support accompanied me throughout my time in Leicester.

DECLARATION

The work presented within this thesis is the exclusive work of the author, Mengxing Tang, except where otherwise acknowledged. Furthermore the work presented has not been published or otherwise distributed by any person other than the author.

Mengxing Tang

August 2002

TABLE OF CONTENTS

	PAGE NO.
ABSTRACT	II
ACKNOWLEDGEMENTS	IV
DECLARATION	V
CHAPTER 1 INTRODUCTION	
1.1 Breast Cancer and Current Detection Techniques	1
1.1.1 X-ray Mammography	1
1.1.2 Ultrasound Scan	3
1.1.3 Other imaging modalities	3
1.2 Electrical Impedance Mammography (EIM)	5
1.2.1 What is EIT	6
1.2.2 Advantages of EIT	6
1.2.3 Current problems with EIT breast Imaging	8
1.3 Aims and Objectives	9
1.4 Outline of the thesis	10
CHAPTER 2 PROJECT BACKGROUND	
2.1 Human Breast and Breast Carcinoma	12
2.1.1 Human Breast	12
2.1.2 Breast disease and breast cancer	12
2.1.3 Electrical properties of breast tissue	14
2.2 Image Reconstruction in EIT	15
2.2.1 Mathematical model	16
2.2.2 Current patterns	17
2.2.3 Reconstruction algorithms	19
2.2.4 FEM method	21
2.3 History and Clinical Application of EIT	22
2.3.1 History of EIT	22

2.3.2 Clinical applications of EIT 24
2.4 Summary 28

CHAPTER 3 IMAGE RECONSTRUCTION ALGORITHMS: IMPLEMENTATION AND COMPARISON

3.1 Introduction 30
3.2 Two dimensional FEM Forward Solver 31
3.3 Image Reconstruction Algorithms: Principle and Implementation 34
3.3.1 Back Projection algorithm(BP) 34
3.3.2 General Inversion algorithm(GI) 37
3.3.3 Modified Newton-Raphson algorithm(N_R) 39
3.4 Image Reconstruction Algorithms: Performance Comparison 41
3.4.1 Simulation settings 42
3.4.2 Imaging results with noise-free data 43
3.4.3 Imaging results with noise added data 46
3.4.4 Comparison 49
3.5 Summary 52

CHAPTER 4 THE NUMBER OF ELECTRODES AND BASIS FUNCTIONS IN EIT IMAGE RECONSTRUCTION

4.1 Introduction 53
4.2 Singular Value Decomposition(SVD) and Spectrum Expansion 55
4.3 Theoretical Analysis 57
4.3.1 Image reconstruction algorithm 57
4.3.2 Theoretical analysis with different NOE and NOCBF 58
4.4 Simulation Study 60
4.4.1 Simulation target 60
4.4.2 Other simulation settings 61
4.5 Results and Discussion 64
4.5.1 Results of singular values, reconstructed images, and errors across ROI 64

4.5.2 Discussion 67
4.6 Conclusions 70
4.7 Summary 71

CHAPTER 5 SELECTING COMPATIBLE PRIOR INFORMATION IN EIT IMAGE RECONSTRUCTION

5.1 Introduction 72
5.2 Principle 74
5.2.1 Image reconstruction and its sensitivity to noise 74
5.2.2 Errors introduced by incompatible prior information 75
5.2.3 Convergence behaviour of the algorithm 82
5.3 Simulation Study 83
5.3.1 Simulation objects 83
5.3.2 Coarse mesh design 84
5.3.3 CF index 85
5.3.4 Forward problem 86
5.3.5 Image reconstruction 86
5.4 Results 87
5.4.1 Noise free simulation results 87
5.4.2 Simulation with noise added 92
5.5 Discussion and Conclusions 95
5.6 Summary 97

CHAPTER 6 AN ELECTRICAL IMPEDANCE MAMMOGRAPHY SIMULATION SYSTEM AND PRELIMINARY RESULTS

6.1 Introduction 98
6.2 Clinical *in vitro* measurements and Cole-Cole model 99
6.2.1 Clinical *in vitro* measurement 99
6.2.2 Cole-Cole model 100
6.3 Simulation breast model 102
6.3.1 Construction of breast models with the generated

Cole-Cole parameters 102
6.3.2 Development of boundary voltages using FEM method 103
6.4 Image reconstruction Results 104
6.4.1 Static imaging results 104
6.4.2 Difference imaging results 106
6.5 ROI Analysis 108
6.5.1 ROI setting 108
6.5.2 ROI analysis results 109
6.6 Conclusion 114
6.7 Summary 115

CHAPTER 7 THREE DIMENSIONAL ELECTRICAL IMPEDANCE TOMOGRAPHY AND ELECTRODE PLACEMENT

7.1 Introduction 116
7.2 Three Dimensional FEM Forward Solver 117
7.2.1 Principles 117
7.2.2 For the matrix K 120
7.2.3 For the matrix I 123
7.2.4 Solving the equation in the forward problem 123
7.3 Image Reconstruction Algorithm 124
7.4 Sensitivity Analysis: a comparative study between two electrode placement configurations 126
7.4.1 Simulation study 126
7.4.2 Results of sensitivity analysis 130
7.4.3 Results of image reconstruction 135
7.4.4 Discussion and conclusion 136
7.5 Summary 139

CHAPTER 8 CONCLUSIONS AND FUTURE WORK

8.1 Conclusions 140
8.2 Future work 142

REFERENCES 145

APPENDICES: Publication list during PhD study 155

CHAPTER 1 INTRODUCTION

This chapter gives a brief introduction to the background of Electrical Impedance Mammography and the content of this thesis.

Section 1.1 briefly reviews breast cancer and current detection techniques. In section 1.2 Electrical Impedance Mammography is introduced. Section 1.3 describes the aims and objectives of the present study, followed by the outline of the thesis in section 1.4.

1.1 Breast cancer and current detection techniques

Breast cancer continues to be a leading cause of premature death in women in the western countries. This is despite a concerted effort to reduce mortality through the detection of cancers by organised x-ray screening programmes. According to the National Statistics [Quinn 2001], in 1996 there were 36100 cases of breast cancer in UK, and in 1998 it claimed 13200 lives. On in twelve British women will develop breast cancer in their lifetime, and every half an hour there is a British woman who dies from breast cancer.

One way to effectively reduce the mortality is to detect cancer at an early stage. The earlier it can be detected, the better the chance of a cure. The following section gives a brief introduction to several major imaging modalities used for detection of breast cancer.

1.1.1 X-ray mammography

X-ray mammography is the firstline technique for detection of breast cancers. It is a specific type of imaging that uses a low-dose x-ray system and high-contrast, high-resolution film for examination of breasts. The image of the breast is produced as a result of some of the x-rays being absorbed (attenuated) while others pass through the breast to

expose the film. Obviously this technique relies upon the relative opacity of different breast tissues when they are exposed to x-ray radiation.

Although x-ray mammography is widely accepted as a firstline method for breast cancer detection, it still has the following problems:

1) The detectability for young patients is poor. In breasts glandular and fibrous tissues absorb the x-ray beam equally, whereas adipose tissue is more radiolucent and provides the necessary subject contrast. The breasts of young women have less adipose tissue, therefore high levels of radiographic density reduce the contrast of different tissue and therefore reduce the usefulness of X-ray mammography for this group;

2) It exposes the patients to radiation. This is harmful and there is increased risk of inducing cancers by this radiation. Some scientists [Epstein 2001] describe this as "dangerous";

3) The diagnostic information is limited to that which can be inferred from the location, architecture, and opacity of the abnormality, as the image is based upon relative radio-opacity. This normally requires further surgical procedures to be carried out to determine the exact nature of the abnormality. These include Fine Needle Aspiration (FNA) and Core Biopsy. FNA consists of a small needle being inserted into the lesion to remove fluid, in the case of a cyst, or a small number of cells for histological analysis. The Core Biopsy is similar except that the procedure is carried out using a much wider bore needle. Local anaesthesia is used and the removed cells are being similarly histologically analysed.

1.1.2 Ultrasound scan

An alternative mammographic method is that of ultrasonography. Ultrasound as a diagnostic technique for breast cancer depends on the acoustic properties of breast tissue. While normal breast tissue scatters and attenuates sound, solid masses within the breast strongly reflect sound, producing ultrasonic echos. Thus ultrasound enables visual imaging of lesions in the breast. Ultrasound is especially helpful in distinguishing between abnormalities that are solid or filled with liquid (a cyst). At the same time it can be used as a guide for interventional procedures such as aspiration and biopsy. However, one unusual characteristic of the breast is that relative to the parenchyma, fat in the breast is hypoechoic. This poses some problems for ultrasound because generally breast cancers are hypoechoic. A significant number of breast cancers are difficult if not impossible to be seen using ultrasound because they are isoechoic with fat or breast tissue. Additional limitations are due to operator experience and interpretation difficulties. Normally this method is limited to being an adjunct to the x-ray mammography.

Certain types of ultrasound machine can show the blood supply to the lump and this may help to distinguish between a cancer and a benign lump by imaging the relatively high number of blood vessels associated with later stage lesions. This, although not permitting detection at an earlier stage, may permit the use of the technique in radiologically difficult breasts, such as those of younger women, for which x-ray mammography is not suited.

1.1.3 Other imaging modalities

Magnetic Resonance Imaging

MRI imaging of the breast has undergone two cycles of investigation and development [Kopans 1998]. In the initial testing it was found that the differences in the relaxation times between benign and malignant tissues overlapped and were frequently insufficient to

provide any clinical benefit as a diagnostic procedure. Many breast cancers were even indistinguishable from normal breast tissue. When a contrast agent, called Gd-DTPA, became available, a second round of breast MRI investigation began leading toward potentially clinically useful applications. With the contrast agent, the vast majority of malignancies demonstrate enhancements. Unfortunately, some benign entities also enhance. The use of enhancement to separate the normal from the abnormal is somewhat complicated by the fact that normal breast parenchyma also causes enhancements. Therefore at present, MRI is primarily used in solving some specific breasts problems such as the evaluation of silicone implant rupture, distinguishing scar from cancer recurrence, and local staging of breast cancer.

Near-Infrared Imaging(NIR)

Light in the near infrared portion of the spectrum can pass through human tissues such as breast tissues. Just as with x-rays, this can be used to form shadows of the internal structure of the breast. Unfortunately, an extremely small amount of light passes directly through the breast. The vast majority is scattered and diffused, reducing or eliminating the signal relative to the noise. This made multispectral diffuse transillumination of the breast to be shown to have no value in the detection or diagnosis of breast cancers [Alveryd *et al* 1990].

In recent years NIR tomography of breasts has been investigated [Boas *et al* 2001] [Schweiger *et al* 1999]. This is based on the fact that tumours generally are more highly vascularized than surrounding tissue, thus leading to differential light absorption properties. However, it is generally still at the laboratory stage and the clinical efficiency is yet to be proved.

T-Scan

A new technique has been licensed for use as an adjunct to x-ray mammography by the Food and Drug Administration (FDA) in the US. The device, called 'TransScan T-Scan', uses a low frequency voltage source to determine the relative impedance of an area that is mammographically abnormal [Assenheimer *et al* 2001]. The impedance, being normalised to the remaining areas of the breast, provides additional indicators to the exact nature of the lesion. An imaged 'bright spot' is indicative of a malignant lesion. This method is only to be used on patients who have a suspicious mammography record. Any further diagnostic information is not available.

It can be concluded that the current diagnostic imaging modalities are able to give useful information for diagnosis. However, every modality has its own shortcomings. Even the combination of several techniques is unable to satisfactorily solve all the problems. This is especially true in terms of the detection and identification of cancer in the early stage and in young women. Therefore development of a new imaging technique able to detect and identify breast cancer at an earlier stage is highly desirable.

1.2 Electrical Impedance Mammography (EIM)

EIM is the application of Electrical Impedance Tomography (EIT) technique to breast imaging. In the remainder of the thesis, "EIT" is used as a general term for the technique involved except for the special case related to breast imaging where the term "EIM" is used.

1.2.1 What is EIT

In EIT currents are applied to the body through electrodes that are attached on the surface and the corresponding surface voltages are measured. Based on these boundary measurements the distribution of the internal electrical property of the body can be reconstructed. The electrical property can be impedivity or admitivity, both of which are complex values. In order to simplify the problem, most of the current studies consider only the real parts, which are resisitivity or conductivity respectively.

A typical EIT system is shown in Figure 1.1. It usually consists of three major functional parts: data acquisition, image reconstruction, and image display and analysis.

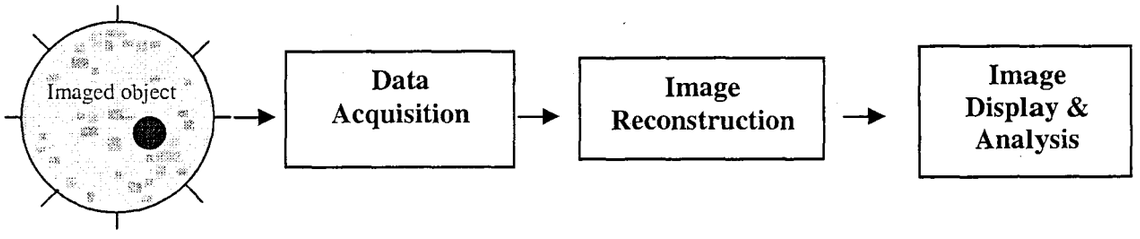

Figure1.1 Block Diagram of a typical EIT system

1.2.2 Advantages of EIT

EIT, as a new medical imaging method, has many advantages:

1) EIT is the only currently available imaging technology which is able to directly image the electrical properties of the tissue in the body;

2) EIT is a functional imaging method;

Different types of tissue have different electrical properties. Even the same type of tissue, when under different physiological condition, may have different electrical properties [Cole *et al* 1941] [Foster *et al* 1989]. Therefore, EIT is a functional imaging method which has the potential to show the physiological and pathological information. Particularly, it has the potential to detect abnormal tissue such as cancerous tissue from normal tissue.

3) EIT has no ionising effect. It uses tiny injected currents and is harmless to both patients and operators;

4) Due to the simple measurement system (up to now it uses either electrodes or coils to inject and measure signals), EIT is a low cost technology;

5) The electrical properties of human tissue change when the current frequency changes. Every type of tissue corresponds to an impedance spectrum, which could possibly be used as a "fingerprint" to characterise and identify different tissues.

Therefore, compared with other imaging modalities, these advantages make EIT an imaging technique which not only has the potential to detect and identify abnormal tissue from normal tissue but is more acceptable to both patients and hospitals.

Although EIT technique can be applied to different parts of human body, application to breast imaging is considered more promising. This is because breasts can be easily deformed to a regular shape to facilitate measurement and breasts are near the periphery of the body and therefore can possibly offer a better measurement sensitivity.

1.2.3 Current problems with EIT in breast imaging

Application of the EIT technique to breast cancer detection currently suffers from a major problem, that of the poor image quality obtained. The image resolution is very low, comparing with CT or Ultrasound. The resolution for a typical EIT system is 5%~20% of the diameter of the object [Holder 1993][Wheeler *et al* 2002]. How to improve the image quality is crucial to its further application in clinical diagnosis.

The image quality of EIT depends on two aspects, provided that the performance of the data acquisition system (or the noise level of the acquisition system) is fixed. These are:

- The amount of information contained in the measurements. This information is determined by several factors including the number of electrodes, electrode configurations, and current injection and signal measurement strategy;

- Image reconstruction techniques. These include image reconstruction algorithms, conductivity basis functions, regularization methods, and prior information in image reconstruction.

Furthermore, although there are studies showing limited results of *in vivo* breast imaging, the feasibility of using EIT to detect and identify breast cancer is still largely an open question.

1.3 Aims and objectives

The overall aim of the whole project in the biomedical engineering group of DMU is to develop impedance imaging techniques and system for early detection of breast cancer.

The specific aims of the research work reported in this thesis are to investigate methods of improving EIT image quality and to establish the viability of using EIT in breast cancer detection.

The aims are to be achieved by satisfying the following objectives:

1) The implementation and comparison of different image reconstruction algorithms;

2) The investigation of two important factors in image reconstruction, the number of electrodes and the number of conductivity basis functions, and their effects on the quality of reconstructed images;

3) The investigation of methods incorporating compatible prior information in EIT image reconstruction to improve the image quality;

4) Setting up breast models based on *in vitro* tissue impedance measurements and setting up a breast impedance imaging simulation system for feasibility study of EIM;

5) Consideration of three-dimensional EIM image reconstruction and optimal electrode placements.

1.4 Outline of the thesis

The work is organised into the following chapters.

Chapter 2 details the background to the technique involved in this study. This includes sections of introduction to the main features of breast and breast cancer, the background to EIT technique, and history and clinical applications of EIT.

Chapter 3 presents the investigation of several candidate image reconstruction algorithms. Three different image reconstruction algorithms aree introduced and implemented. Their performance is compared and one is chosen as a more appropriate algorithm for the subsequent study on breast imaging.

The most of novel work conducted during the course of the doctoral research is largely concentrated on the research work presented from Chapter 4 to 7.

Chapter 4 is devoted to two important factors in EIT image reconstruction: the number of electrodes (NOE) and the number of conductivity basis functions (NOCBF). The image reconstruction is analysed with different combinations of NOE and NOCBF using Singular Value Decomposition (SVD) and spectrum expansion theory. Final suggestions are given on which configuration can offer better image quality in breast imaging.

Chapter 5 investigates compatibility of different types of prior information and its effect on an iterative image reconstruction algorithm, based on which a novel method is proposed to improve EIT image quality. This method selects compatible prior information by observing the convergence behaviour of the image reconstruction algorithm. The principle, implementation, and results are presented.

In Chapter 6 clinical *in vitro* measurements of different breast tissue and Cole-Cole model are described, based on which a two-dimensional breast imaging simulation system is introduced. Several breast models with different physiological and pathological conditions are made. Images with different current frequencies are reconstructed and the results are analysed.

Chapter 7 extends the finite element model and the image reconstruction from two dimensions to three dimensions. The mathematical principle and implementation are described. The sensitivity of boundary measurements to the conductivity changes in a cylindrical object is analysed with two different types of electrode placement, ring placement or plane placement. 3D images are reconstructed and discussed. Finally suggestions are given on optimal electrode placement in a breast imaging system.

The thesis concludes with Chapter 8 in which general conclusions and the success of the research are discussed, together with suggestions for further work.

CHAPTER 2 PROJECT BACKGROUND

This chapter addresses the background to the EIM technique in detail. Initially an introduction is given in section 2.1 to the physiology of human breasts and breast carcinoma, followed by an introduction of EIT image reconstruction techniques in section 2.2. The history and applications of EIT are briefly reviewed in section 2.3, and section 2.4 contains a summary.

2.1 Human Breast and Breast Carcinoma

2.1.1 Human Breast

The breast is composed of glandular tissue, adipose tissue, ducts, and connective tissue. The glandular tissue consists of 15–20 lobes containing numerous lobules, linked by ductules as shown in figure 2.1. The ductules combine to form the lactiferous ducts, which open into the lactiferous sinuses and empty through the nipple. The glandular tissue, ducts, and connective tissue are collectively known as stroma. Beneath the skin lies a layer of fat, and there is also fat between the glandular structures. Most breast cancers appear to originate in the ducts, although there are those that appear to be derived from the glandular tissue [Kopans 1998].

2.1.2 Breast disease and breast cancer

Benign breast disease

Benign breast disorders can be broadly divided into two categories [Harris 1991]: (1) so-called fibrocystic disease, a wastebasket term that encompasses a variety of changes,

including cysts, stromal fibrosis, and epithelial proliferative lesions, singly or in combination; and (2) specific entities, such as fibroadenomas.

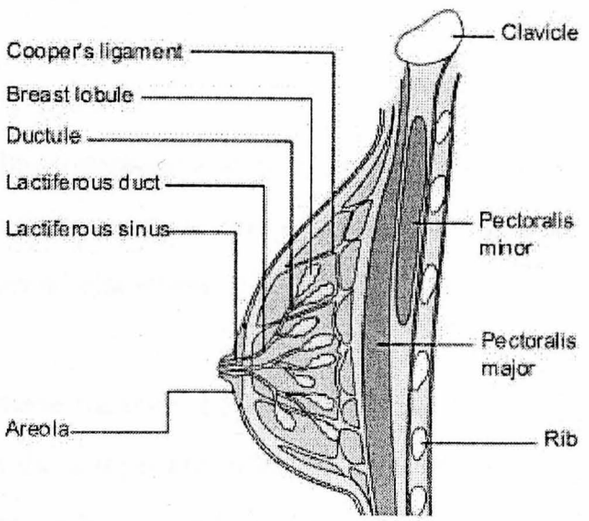

Figure 2.1 - Structures of the normal breast (courtesy of www.minervation.com)

Breast cancer

Breast cancer is one of the best studied human tumours, but it remains poorly understood. What has become fairly certain is that, as with all solid tumours, breast cancer is the result of DNA alterations (damage or mutation) that lead to uncontrolled cell proliferation. It can be categorized by the position from where it arose, generally the cells of the ducts or the components of the lobules.

Staging of breast cancer

The stage of a cancer [Kopans 1998] is a term used to describe its size and whether it has spread beyond its original site. Generally breast cancer is divided into 4 stages as follows:

Stage 1 cancers: these measure less than or equal to two centimetres. The lymph glands in the armpit are not affected and there are no signs that the cancer has spread elsewhere in the body.

Stage 2 cancers: these measure between two and five centimetres, or the lymph glands in the armpit are affected, or both. However, there are no signs that the cancer has spread further.

Stage 3 cancers: these are larger than five centimetres and may be attached to surrounding structures such as the muscle or skin. The lymph glands are usually affected, but there are no signs that the cancer has spread beyond the breast or the lymph glands in the armpit.

Stage 4 cancers: these are of any size, but the lymph glands are usually affected and the cancer has spread to other parts of the body. This is secondary breast cancer.

2.1.3 Electrical properties of breast tissue

The human body is a volume conductor of electricity. Tissues in the body are composed of cells, surrounded by extra-cellular fluid within both of which are contained ions. In the presence of an electric field, current is conveyed by the transport of ions. The movement of ions, however, does not proceed unhindered, since the cell's membranes represent a partial

barrier to ionic conduction. In addition to the flow of ions, bound changes are also present within tissues so dielectric effects are also exhibited and give rise to displacement currents when an electric field is applied.

Studies on electrical properties of breast tissue have been reported since the early 20th century. For example, Fricke and Morse [Fricke *et al* 1926] found significantly higher permittivity of the tumour tissue at 20kHz as compared to the normal or non-malignant tissues. England and Sharples [England *et al* 1949] examined several samples of breast carcinoma at 10 GHz. Surowiec [Surowiec *et al* 1988] measured relative permittivity of infiltrating breast carcinoma and the surrounding tissue. Although large spread of data for the same type of tissue was present, it was found that permittivity and conductivity of breast carcinoma tissues (20 kHz to 100 MHz) were both higher than those of normal breast tissues. A recent study by Jossinet [Jossinet *et al* 1998] also suggested significant difference between carcinoma and other tissues, although all the measurements had large standard deviation.

A comprehensive review in tissue electrical properties can be found in [Foster and Schwan 1989].

In summary, all the studies suggested that normal tissue and cancerous tissue have different electrical properties. However, the measurements conducted in different studies spread over a large range and the consistency was low.

2.2 Image Reconstruction in EIT

Image reconstruction is one of the key components of the EIT technique, in which the boundary measurements are used, together with the knowledge of the boundary shape of the object, the position of the electrodes, and the injected current, to reconstruct the impedance distribution of the imaged object. The following sections give a general

introduction to several key aspects in image reconstruction including the mathematical model, current patterns, the image reconstruction algorithm, and the finite element method.

2.2.1 Mathematical model

In EIT, the electric field is governed by the equation

$$\nabla \cdot \sigma \nabla u = 0 \tag{2.1}$$

with boundary conditions

$$u = \bar{u} \qquad \text{voltage distribution on } \partial A \tag{2.2}$$

$$\sigma \frac{\partial u}{\partial n} = J \qquad \text{current density on } \partial A \tag{2.3}$$

Here σ is the conductivity distribution. u is the voltage distribution. J is the current density. ∂A is the boundary of the region to be imaged.

EIT involves solving two different problems: forward problem and inverse problem. In the forward problem, given conductivity distribution σ and boundary current density J, the voltage and current density distributions are sought. In the inverse problem, given voltage distribution u and current density distributions J, conductivity distribution σ is sought.

In EIT boundary voltages and current distribution are generally known and it is the conductivity distribution that is sought. Therefore it is an inverse problem. In particular, it is also called a boundary value problem, as only the voltage and current distribution along the boundary are known. Generally, during the solving of the inverse problem, the forward

problem has to be solved, i.e. solving forward problems is an integral part of solving inverse problems in EIT. Detailed explanation about this is found in chapter 3.

2.2.2 Current patterns

Current patterns define how the currents are injected through electrodes into the object being imaged. Therefore it determines the boundary condition in equation (2.3) and plays an important role in EIT. Generally, current patterns fall into two categories depending on the number of current electrodes used simultaneously in the current injection process. In the first category the current is injected using one pair of electrodes, while in the other current is injected using more than 2 electrodes.

Current patterns with one pair of electrodes are generally used, as it is a simple way to inject current, one electrode for inward current and another for outward current. As only one current source is needed the hardware design and system control are easier and costs are less. Typical current patterns using one pair of electrodes are the adjacent and the polar pattern. The adjacent pattern uses adjacent pair of electrodes to inject current, while the polar pattern uses polar pair of electrodes.

For a system with L electrodes, an example of an adjacent pattern is shown in Figure2.2 and can be mathematically presented as:

$$I_m = \begin{cases} 1 & m = 1 \\ -1 & m = 2 \\ 0 & otherwise \end{cases} \qquad (2.4)$$

where I_m is the current on the m^{th} electrode($m=1\sim L$).

An example of the polar pattern is given by:

$$I_m = \begin{cases} 1 & m = 1 \\ -1 & m = L/2+1 \\ 0 & otherwise \end{cases} \quad (2.5)$$

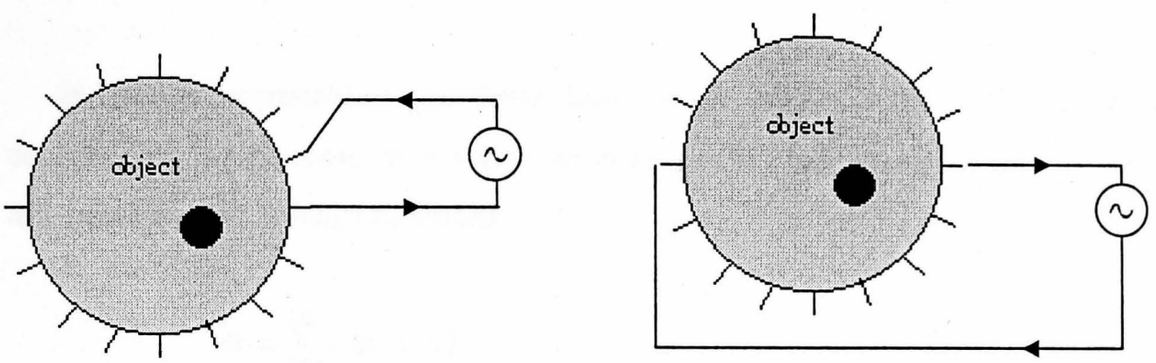

(a) (b)

Figure 2.2 Current patterns

(a) An example of adjacent pattern. *(b) An example of polar pattern.*

Some studies use more than one pair of electrodes to inject current. A typical example would be the trigonometric current patterns which are given by:

$$I_m = \begin{cases} Cos(\ m*2*\pi/L) & m = 1 \sim L/2 \\ Sin((m-L/2)*2*\pi/L) & m = L/2+1 \sim L \end{cases} \quad (2.6)$$

In these current patterns, every electrode is used to inject current. Previous study by [*Isaacson 1986*] showed that these current patterns are able to produce optimal results under certain circumstance.

2.2.3 Reconstruction algorithms

In EIT image reconstruction, given the boundary voltage and current density distributions, the conductivity distribution σ within the whole region is reconstructed by the so-called image reconstruction algorithm. It is one of the key elements in the EIT technique.

In image reconstruction, a finite-dimensional model is defined to approximate the conductivity distribution. It is called an image reconstruction model and can be presented as a combination of basis functions:

$$\sigma = \sum_{i=1}^{m} c_i \omega_i(x, y) \qquad (2.7)$$

Here σ is the conductivity distribution. m is the degrees of freedom. ω_i is the conductivity basis function.

Piecewise constant basis functions are usually used for image reconstruction, because they are simple cases of conductivity basis functions. They are easy to implement and fast in terms of calculation. There is a mesh corresponding to these piecewise basis functions and the conductivity image is reconstructed based on this mesh. A typical mesh is shown in Figure2.3.

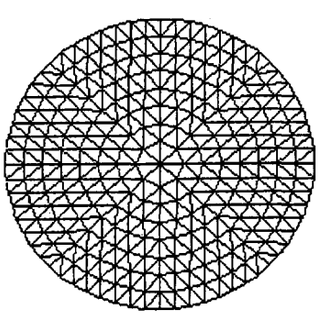

Figure 2.3 An example of a mesh

If the particular mesh shown in Figure2.3 is used for image reconstruction with piecewise constant functions, it indicates that the imaged plane is circular and the conductivity distribution within every triangle of the mesh is uniform, while the conductivity of different triangles can be different.

EIT image reconstruction algorithms generally fall into distinct categories. The first is called difference imaging algorithm, which reconstructs the impedance change between a background and a foreground. It is generally a one-step method based on linear approximations. In this type of algorithms it is assumed that the foreground conductivity does not differ significantly from the background conductivity. The input to this algorithm is the measurement difference between the background and the foreground, and the output is the impedance difference between the foreground and background. Examples of linear methods are the back-projection algorithm [Barber *et al* 1984] and general inversion algorithm [Tang *et al* 1998].

Another class of image reconstruction algorithms are termed static imaging algorithms. This type of algorithms reconstruct absolute value of impedance distribution. Generally they are iterative algorithms. Firstly an initial impedance distribution is assumed, and then the corresponding boundary voltages are calculated. Following this a modification is made in the assumed impedance distribution to minimise the difference between the calculated boundary voltages and the measured boundary voltages. Several iterations of the procedure are carried out to produce an acceptable solution. An example of this type of technique is the Newton-Raphson based algorithm reported by [Yorkey *et al* 1987] and [Edic *et al* 1998].

It should be noted that after some modification, algorithms used to reconstruct static images could be used to reconstruct difference images and vice versa.

2.2.4 FEM method

For reconstruction of conductivity images, forward problem needs to be solved. Since it is difficult to analytically solve the forward problem for an arbitrary resistivity distribution, a numerical technique such as the Finite Difference Method (FDM) or Finite Element Method (FEM) is the most suitable to use.

It is well known that FEM is better than FDM for arbitrary shaped boundaries. In addition, FEM gives a piecewise approximation to the governing equation whereas FDM gives a pointwise approximation. Therefore, most reconstruction algorithms in EIT use FEM in solving the forward problem. Some details about the FEM method are reported in Chapter 3. In FEM the region is discretised into a finite element mesh, like the one shown in Figure2.3. However its usage is different from the one for image reconstruction. The mesh used for image reconstruction corresponds to the conductivity basis functions, while the FEM mesh corresponds to the basis functions of the finite element method used for solving forward problem.

However, in many studies just one mesh is used both for forward solver and for image reconstruction. This is a simple way to operate and solve EIT problems. However the drawback is that because the mesh for image reconstruction can only have a relatively small number of elements due to the heavy computing overhead and the ill-posed condition, the forward solver with the same mesh would be less accurate.

2.3 History and Clinical Application of EIT

2.3.1 History of EIT

The history for impedance imaging can be traced back to 1978, when the first impedance images were published by Henderson and Webster [Henderson *et al* 1978]. However, they produced images of the thorax that were not tomography images but transthoracic impedance images.

The inventors of impedance tomography – that is the first people to propose applying EIT as a tool for medical diagnosis – are Barber and Brown, of the University of Sheffield, who opened up this new field of investigation by presenting the first tomographic image of an arm in 1983 [Barber *et al* 1983]. They used the back-projection algorithm, which is the first one to produce *in vivo* images.

This innovation was embodied in the first patent related to the technique known as applied potential tomography (APT). The 1980s saw the emergence of an increasing number of impedance imaging research projects, the first results of which were presented at the European Community Workshops on Electrical Impedance Tomography in Sheffield, UK and Lyon, France in 1986 and 1987, respectively. More recently, three Annual EPSRC Network Meetings on EIT were held in UCL, London from 1999 to 2001 and there will be an EIT workshop in USA in August 2002.

Difference Imaging and Static Imaging

The first difference imaging method, which was successful in obtaining *in vivo* images, was that of Barber [Barber *et al* 1983]. Difference imaging uses the difference of two sets of measurement, therefore some common system errors in both sets of measurement can be eliminated. This makes difference images relatively easy to obtain.

At the early stage of EIT, obtaining static images was difficult because static imaging requires accurate modelling of the system under investigation and is sensitive to errors & noises. However, the development of EIT hardware system design reduced the system errors and the accuracy of modelling of the system was also improving. These therefore gave rise to successful static imaging. The first static imaging method to achieve widespread attention was that of Isaacson [Isaacson 1986]. This method consists in choosing optimum current patterns, which are distributed around the boundary of the object.

Multi-frequency Imaging

In early the 80s currents were applied at a single frequency – typically some tens of kilohertz in the static and difference imaging methods. However, human tissues do not behave simply like resistances, but also exhibit a reactive component due to the presence of cell membranes. As the reactive component is another important part of tissue electrical properties, this led to variable frequency methods being developed to construct images of different frequencies. The corresponding methods are often termed multi-frequency EIT.

The work that really initiated multi-frequency EIT was published by Griffiths [Griffiths *et al* 1987] from the University Hospital of Wales, initially with a view to mitigating the problems encountered in making static images *in vivo*. Images were obtained by use of a current with two frequencies(100kHz and 150kHz) in a 16 electrode system. Subsequent to this first approach, Griffiths *et al* [Griffiths *et al* 1989] obtained experimental multi-frequency images of conductivity *in vitro* and *in vivo* at 40.96kHz and 91.92kHz. Complex *in vitro* multi-frequency images were presented by Jossinet and Trillaud [Jossinet *et al* 1991] at the frequencies of 250kHz and 31.25kHz. More recently, Wilson et. al. developed the Sheffield Mk3.5 EIT/EIS system which measures both the real and imaginary part of impedance at 30 frequencies between 2k Hz and 1.6 MHz. [Wilson *et al*

2001]. Hartov et. al. described their considerations for an EIT system which covers the frequency range of 0 to 10MHz [Hartov *et al* 2001].

Three-dimensional Imaging

Two-dimensional images are usually constructed from measurements made with electrodes arranged in a single plane, but the object under investigation, and consequently the electrical fields within it, are three-dimensional. Currents cannot be constrained to flow in a plane, and hence, off-plane impedance changes mean that 2D measurements are liable to introduce errors. Therefore 3D imaging is playing an increasingly important part in EIT research. The first attempt to produce 3D conductivity images was presented by Goble and Isaacson, at the IEEE-EMBS conference in 1990 [Goble *et al* 1990]. *In vitro* measurements were made with 64 electrodes arranged in four planes on a cylindrical tank. Metherall [Metherall *et al* 1996] having published the first landmarking *in vitro* 3D EIT images presented a comparison of simulated and real images of change in the conductivity in a saline-filled phantom. More recently, some groups have published 3D *in vivo* images of lungs [Mueller *et al* 2001] and breasts [Cherepenin *et al* 2001].

2.3.2 Clinical applications of EIT

After Barber and Brown designed a prototype system in 1983, EIT began to be used in various clinical applications, for example lung imaging, brain imaging, heart imaging, digestive system imaging, and breast imaging.

In the application of EIT to lung imaging, experiments have been conducted for: respiratory volumetric measurements, ventilatory defects, acute pneumothorax, patients undergoing mechanical ventilation, pulmonary perfusion, pulmonary edema, pulmonary embolus, emphysematous bulla, and absent perfusion.

Harris *et al* [Harris *et al* 1987] published *in vivo* EIT images reconstructed from data obtained during a series of inspiratory manoeuvres which showed the lung conductivity changing considerably with ventilation in a reproducible fashion. Sahalos *et al* [Sahalos *et al* 1992] considered that the percentage change in the measured impedance from that theoretically predicted value was a good predictive index of the state of the lung in 60 subjects of whom 37 had a pulmonary disease and 23 had no lung disease. Lionheart [Lionheart *et al* 1997] studied high-speed *in vivo* chest impedance imaging using their third-generation EIT system developed at Oxford Brookes University. This system, based on the adaptive current method, applies current simultaneously through 32 current electrodes, and measures voltages on the 32 voltage electrodes in a frequency range from 10kHz to 160kHz. Hahn *et al* [Hahn *et al* 1995] performed experiments with the aim of checking the suitability of EIT in imaging regional thoracic impedance variations during lung ventilation under predefined conditions and compared EIT with established reference techniques. Experiments results, according to the authors, revealed an overall agreement between the spirometric and impedance data in all breathing patterns performed. Smit *et al* [Smit *et al* 2002] used EIT to monitor dynamic changes in the pulmonary vascular bed. The authors concluded that EIT is a reliable method to measure blood volume changes due to pharmacologically induced vasodilatation in the pulmonary bed.

Since the conductivity of blood is higher than that of most tissues, variations in blood perfusion through an organ should appear in dynamic images. But these changes differ according to the organs, and Eyuboglu succeeded in identifying in impedance images different regions of the human thorax corresponding to ventricles, aorta, lungs, atria, and pulmonary arteries. The target was to calculate the amount of blood flow through each organ, but this was not yet achievable. In particular, measurements of stroke volume and cardiac output suppose 3D acquisition and an image resolution that permits adequate separation of the cardiac chamber. Eyuboglu *et al* [Eyuboglu *et al* 1987] have shown that the different contributions of cardiac-related thoracic impedance variations can be separated by using ECG gated images, and they observed the movement of blood from the ventricles

to the lungs and vascular system and back to the heart. More recently, Newell *et al* [Newell *et al* 2002] has produced real time three-dimensional images of human chests. In these images phasic changes throughout the cardiac cycle are seen to be markedly different at the heart compared to lung region, both above and beside it, although image resolution is low.

The first interesting EIT results for brain imaging were published by Tarassenko *et al* [Tarassenko *et al* 1984] and Murphy *et al* [Murphy *et al*1987] who detected bleeding into the right ventricle in a one day old baby. Subsequently McArdle [McArdle *et al* 1988] obtained images of the conductivity changes in the adult brain during the cardiac cycle. The ECG gated images were reproducible for the same subject but with wide variations among the 12 adults imaged. The images were severely distorted by the presence of the skull.

Variations of 10% of cerebral impedance occur during conditions such as stroke, cerebral ischemia, or epilepsy, which are largely due to cell swelling. Such changes have been imaged during the related cortical spreading depression phenomenon in rabbits with the Sheffield Mark 1 EIT system. Spreading depression was produced by cathodic stimulation using the electrode ring. Outward spread of the disturbance in the ipsilateral hemisphere could also be seen in EIT images.

Rao *et al* [Rao *et al* 1996] succeeded in producing, for the first time, images during sensory- or visual-evoked responses in the anaesthetized rabbit, using cortical electrodes with a Sheffield Mark 1 system. They demonstrated that reproducible conductivity changes occur in the cortical region where the evoked potentials are largest and therefore appear to be physiological in origin.

More recently, studies by Tidswell *et al* [Tidswell *et al* 2001] produced images of the human head. The 19 adult subjects were fitted with 16 scalp electrodes and data were collected before, during, and after visual and sensory stimulation. Reproducible impedance changes, with a similar time course to the simulus, were seen in all their experiments.

However, identification of the size and location of the impedance changes is difficult due to the poor image quality.

During motor activity such as gastric emptying or peristalsis, large movements of conductive fluids occur in the bowel, and the parameter of interest is mainly the timing of activity. Gastric emptying profiles are generally obtained with radioactive tracers, X-ray contrast media, and dye dilution by means of gastric intubation or serial blood measurement after drug administration. An electrically conductive meal will induce a decrease in resistivity on an EIT image at the level of stomach, and this variation will slowly disappear during emptying. Thus a curve as a function of time from a region of interest (ROI) analysis, derived from EIT images obtained from adult patients, has been found to be similar to those of the alternative techniques such as scintigraphy, dye dilution scintigraphy, or radiotelemanometry [Avill *et al* 1987]. Similar results were found in paediatric patients [Lamont *et al* 1988].

Impedance tomography offers the possibility of obtaining information about breast disease, and systems have been described by Skidmore *et al,*, who proposed a circular ring with 16 electrodes encompassing the breast, and by Jossinet [Jossinet *et al* 1988] who experimented with pneumatically actuated electrodes for fast positioning. The first electroimpedance mammography system results reported on a phantom were presented by Nowakowski [Nowakowski *et al* 1995] who was investigating the diagnosis of mastopathy on tumour tissues using electroimpedance measurements.

More recently, Kerner TE *et al* [Kerner *et al* 2002][Osterman *et al* 2000] have produced absolute 2D permitivity images of normal and abnormal human breasts using different current frequencies. In the experiments the breast is surrounded by a ring of electrodes. They successfully recovered meaningful images both *in vitro* and *in vivo* of 25 total individual breasts imaged including 12 normal, 2 malignant tumours, 2 benign tumours, 6 cysts, 3 with radiation therapy or lumpectomy. All 4 women with tumours were identified as abnormal with their system. The resulting images corresponded well with

given clinical information. However the system is not able to distinguish pathology (cysts, scars, benign tumours) from malignancies. Significant electrode artefacts were identified in the images.

For 3D breast imaging, Mueller *et al* [Mueller *et al* 1999] proposed a 3D EIT image reconstruction algorithm, given surface voltage data measured on a rectangular array of electrodes which may be a desirable electrode placement for breast impedance imaging.

A three-dimensional imaging system has been developed by Cherepenin *et al* [Cherepenin *et al* 2001] with 256 electrodes mounted on a 12cm by 12 cm pad which is pushed against the breast. Some physiologically meaningful images were obtained and the possibility of detecting breast cancer is under investigation. They also estimated the possibilities of electrical impedance mammography for investigation of the state of mammary glands among women with different hormonal status [Cherepenin *et al* 2002]. They found that electrical impedance mammograms have clear visual distinctions and statistically significant differences in mammary glands conductivity were observed in different groups that related to different physiological events, for example the menstrual cycle, pregnancy, lactation, and postmenopause.

2.4 Summary

This chapter addresses the background of EIM technique. Initially an introduction is given to breast and breast carcinoma. Then EIT image reconstruction techniques are described including mathematical model, reconstruction algorithms, current patterns, and finite element method. Finally the history of EIT development and clinical applications are described.

It can be seen that EIT has been significantly developed during the past two decades, from difference images to static images, from single frequency to multi-frequency, and

from 2D to 3D. Investigations in clinical applications of EIT have closely followed technical developments. The applications are primarily in the area of lung, heart, brain, gastric, and breast imaging. However, to date EIT has not been accepted as a routine diagnostic tool so far, mainly due to its poor image quality.

CHAPTER 3 IMAGE RECONSTRUCTION ALGORITHMS: IMPLEMENTATION AND COMPARISON

This chapter addresses the implementation and comparison of EIT image reconstruction algorithms.

Section 3.1 is a brief introduction. In section 3.2 the Finite Element Method (FEM) forward solver is introduced as an integral part of image reconstruction. The principle of three different image reconstruction algorithms and their implementation are explained in section 3.3. Finally, in section 3.4 the images reconstructed by different algorithms are shown and their performance is compared. Section 3.5 is a summary.

3.1 Introduction

The image reconstruction algorithm is one of the key elements in EIT. The algorithm performance, together with other factors, determines the quality of the reconstructed images.

Many image reconstruction algorithms have been reported in previous studies and performance comparisons have been carried out on some algorithms. However, different studies have addressed this problem from different angles and the image reconstruction settings were different one from another. Therefore, considering the specific aims of this study, the implementation and comparison of different algorithms is useful, provided adequate control is maintained allowing valid comparisons to be made.

The work reported in the following sections implements and compares several different algorithms, in order to choose an appropriate algorithm according to the requirement of

breast imaging. This study is a preparation and a foundation for subsequent studies described in the following chapters.

Before introducing image reconstruction algorithms, the principle of the FEM forward solver is firstly reviewed.

3.2 Two Dimensional FEM Forward Solver

The forward problem solves for the voltage distribution in the region given the conductivity distribution and the boundary condition. It is essential in EIT in that it is an integral part of image reconstruction.

In FEM method, the variational form of equation (2.1) is used, which can be defined as:

$$B(u, v) = f(v) \tag{3.1}$$

Where $u,v \in H^1(\Omega)$, $H^1(\Omega)$ is the associated Sobolev space. In the previous equation:

$$B(u,v) = \iint_{\Omega} \sigma \nabla u \cdot \nabla v \; dxdy \tag{3.2}$$

$$f(v) = \int_{\partial A} J \; v \; ds \tag{3.3}$$

The FEM is used to turn the continuous problem given above into a discrete formulation. First, we discretize the solution domain Ω into small elements and a mesh can be obtained. A typical mesh can be found in Chapter2 figure 2.3.

We approximate the potential distribution within the object with the finite sum:

$$u(x,y) = \sum_{i=1}^{N} u_i \Psi_i(x,y) \tag{3.4}$$

where the functions ψ form a basis for the finite dimensional subspace H' of $H^1(\Omega)$, N is the dimension of the finite subspace H', and u_i is the discretized potential distribution. Here if we discretize the domain into N triangles, then u_i is the potential on every node of the triangles. The FEM basis functions :

$$\psi_i(x,y) \neq 0\,, \quad when\ (x,y) \in \Omega_i$$

Ω_i consist of elements connected to node i.

The same for function v

$$v(x,y) = \sum_{j=1}^{N} v_j \Psi_j(x,y) \tag{3.5}$$

Then by inserting these 2 approximation functions into the variational equation, given that $B(u,v)$ and $f(v)$ are both linear, and v_i can be chosen arbitrarily, the following can be obtained,

$$\sum_{j=1}^{N} u_i \; B(\Psi_i, \Psi_j) \;=\; f(\Psi_i) \tag{3.6}$$

Therefore, we obtain a system of equations that can be written in matrix form as

$$K\,U = I \tag{3.7}$$

Where

$$K(i,j) = B(\Psi_i, \Psi_j) \tag{3.8}$$

$$U = u_i \qquad i=1\sim N$$
$$I = f(\Psi_i)$$

For matrix K, we need to calculate the following integration over the dissected elements (triangles).

$$K(i,j) = B(\psi_i, \psi_j) = \iiint_\Omega \sigma \quad \nabla\Psi_i \cdot \nabla\Psi_j \; dxdydz \qquad (3.9)$$

The integration can be done over every element firstly, and then the results can be summed up. Through transforming every actual element to a regular shape element (standard element), the integration can be easily implemented by computer. More explanation about this can be found in [Mitchell 1977].

The matrix I can be calculated by the following integration:

$$I = f(\psi_i) = \int_{\partial A} J\,\Psi_i \; ds \qquad (3.10)$$

To simplify the problem here every electrode is approximated as only a point. So current is injected through a point(s) into the object and the potential on these points is measured. The position of these points is defined to coincide with some of the boundary nodes in the finite element mesh. Under such assumption the vector I can be easily obtained as follows:

$I = 0$, for all the nodes which are not for current injection
$I =$ Current, for the nodes on which current is injected

This forward solver does not consider some practical factors including the size of the electrodes and the contact impedance. For a more comprehensive model, please refer to [Cheng *et al* 1989].

So far, a group of equations can be obtained like this:

$$K\,U = I \tag{3.11}$$

Here K is the coefficient matrix, U is the potential vector which we are seeking, and I is the current vector for all the nodes.

The easy way to solve this equation in Matlab is to calculate the inversion of matrix K, K^{-1}. Then:

$$U = K^{-1}\,I \tag{3.12}$$

3.3 Image Reconstruction Algorithms: Principle and Implementation

In this part the principle and implementation of three different image reconstruction algorithms are described.

3.3.1 Back Projection algorithm (BP)

Principle

Barber and Brown proposed this algorithm [Barber and Brown 1983] [Barber *et al* 1987] which is based on a linear relationship between the small change in impedance and the small change in boundary measurements.

It is deduced that when impedance change σ_p is small, Laplace equation

$$\nabla \cdot \sigma \nabla u = 0 \tag{3.13}$$

can be approximated as:

$$\nabla^2 u_p = \nabla \sigma_p \cdot \nabla u_\sigma \tag{3.14}$$

Here σ_p is the data set of impedance change, u_p is the data set of measurement change caused by impedance change, u_σ is the data set of measurement before impedance change.

This equation shows a linear relationship between change in impedance and corresponding change in measurements, and can be rewritten in a discrete form as:

$$u_p = S \cdot \sigma_p \tag{3.15}$$

Here S is the matrix denoting the forward linear relationship and is also called sensitivity matrix. Therefore, a linear method can be used to reconstruct impedance images with the boundary measurements. Based on this linearization, Barber and Brown back projects the boundary measurements along the equi-potential lines as an inversion of matrix S to reconstruct the impedance image, which can be presented as:

$$\sigma_p = B \cdot u_p \tag{3.16}$$

B is the back-projection matrix. This technique uses the pre-calculated equipotential lines in a homogeneous medium.

Implementation

A complete procedure of implementing this algorithm is as follows:

Firstly, current is injected between adjacent electrode pairs, one pair at one time. Assuming a homogeneous resistivity the equipotential contours (figure 3.1) ending on the voltage measuring electrodes are calculated.

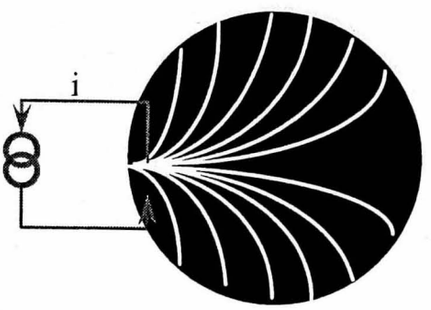

Figure 3.1 The equi-potential lines in a homogeneous region

Secondly, for each projection angle (current injection) two sets of voltages from the imaged object are measured; one as the background set u_σ, the other as the foreground set denoted by $u_\sigma + u_P$. u_P is the voltage difference.

Thirdly, the resistivity between the corresponding equi-potential lines in the computer model is multiplied by the ratio of voltage difference. Then this resistivity distribution estimate was stored. By using the normalised voltage difference to reconstruct images rather than using the absolute value, the author argued that some artefacts such as electrode positioning errors before and after the impedance change could be reduced.

The procedure is repeated for each projection angle always starting off each projection angle with a homogeneous resistivity estimate. After a complete data set is collected, all the previously calculated corrected images are averaged to obtain a composite final image.

Later on, a filter was designed and incorporated into this algorithm [Barber *et al* 1992], then the "filtered back-projection" image reconstruction can be written as:

$$\sigma_p = B(SB)^{-1} \cdot u_p \tag{3.17}$$

Here $(SB)^{-1}$ serves as the filter. It is also stated by Baber that the choice of back-projection matrix will not produce great difference in the final image [Barber *et al* 1992]. If the back-projection matrix B is replaced by sensitivity matrix S, equation (3.17) would be substantially similar to one step of the modified Newton-Raphson algorithm which is described in the following section 3.3.3.

In a special situation when matrix S and B are square, equation (3.17) is reduced to:

$$\sigma_p = S^{-1} \cdot u_p \tag{3.18}$$

This leads to a direct inversion of the sensitivity matrix, which is a specific form of the General Inversion algorithm described in the following section 3.3.2.

3.3.2 General Inversion algorithm(GI)

Principle

This algorithm is also a linearization-based one-step algorithm and based on the linearization relationship shown in 3.15. Generally, the sensitivity matrix S in equation (3.15) is not a square matrix. We define S^+ as the Moore-Penrose general inversion matrix of S. Matrix S has dimension of m*n, (here n<m). Then we get:

$$S^{+} \cdot S = E \tag{3.19}$$

(E is a unit matrix), using equation (3.15)

$$S^{+} \cdot u_p = S^{+} \cdot S \cdot \sigma_p \tag{3.20}$$

Considering equation (3.19) then:

$$S^{+} \cdot u_p = \sigma_p \tag{3.21}$$

It can be seen that by using the general inversion matrix of sensitivity matrix S, the distribution of impedance change σ_p from u_p can be obtained.

Due to the ill-posed condition in image reconstruction, some regularisation method has to be used. In the paper which proposed this algorithm [Tang *et al* 1998], the regularization was such that the singular value of the sensitivity matrix was modified by adopting a threshold α. Singular value smaller than α will be posed to α. This procedure equals using a better condition matrix to replace the ill-conditioned one. Although some information is lost, the ill condition is remedied to some extent.

Implementation

The implementation of GI algorithm firstly requires the calculation of the sensitivity matrix. The sensitivity matrix transforms the change in impedance distribution to the change in boundary voltage distribution. It can be obtained by perturbation method, in which the boundary voltage changes are calculated when there is a small perturbation in the impedance distribution. As a result forward problem is solved for many times with different perturbation in the impedance distribution. Another method for getting this matrix is to calculate the Jacobian matrix, which will be introduced in the latter section 3.3.3.

Secondly, the sensitivity matrix is decomposed and regularised, then inversed to get the image reconstruction matrix. This can be achieved, for example, by using Matlab functions pinv() or svd().

Thirdly, the voltage difference u_p is multiplied by the image reconstruction matrix, as shown in equation (3.21), to get the difference image of impedance distribution.

3.3.3 Modified Newton-Raphson algorithm(N_R)

Principle

The modified Newton-Raphson algorithm is a conventional method to solve non-linear problems. Its application in EIT was proposed by Yorky *et al* [Yorky *et al* 1987] to reconstruct impedance images. The principle is as follows:

If the impedance image reconstruction error is presented as:

$$\Phi = \tfrac{1}{2}(f(r) - u_0)^T(f(r) - u_0) \qquad (3.22)$$

Here f is the function to transfer the impedance distribution r to the voltage distribution f(r). u_0 is the boundary measurements. Then a point r^* which is at least a local minima of Φ can be a solution to the impedance imaging problem. To find a candidate value of r that minimises Φ, Φ is differentiated with respect to r and set the result equal to the zero vector, 0.

$$\Phi' = [f']^T[f - u_0] = 0 \qquad (3.23)$$

The term $\mathbf{f}'$ is known as the Jacobian matrix, an n by m matrix defined by

$$[\mathbf{f}']_{ij} = \frac{\partial \mathbf{f}_i}{\partial r_j} \tag{3.24}$$

Since equation (3.23) is still a nonlinear function of r, a Taylor series expansion of (3.23) is taken about an arbitrary point $r = r^k$ and keep the linear terms

$$\Phi' \approx \Phi'\left(r^k\right) + \Phi''\left(r^k\right)\Delta r^k \tag{3.25}$$

Where $\Delta r^k = r - r^k$

The term Φ'' is called the Hessian matrix, given by

$$\Phi'' = [\mathbf{f}']^T \mathbf{f}' + [\mathbf{f}'']^T \{[\mathbf{f} - u_0] \otimes I_m\} \tag{3.26}$$

where $\otimes$ is the Kronecker matrix product. The term f'' in equation (3.26) is difficult to calculate explicitly, but often it is negligible relative to the first item in equation (3.26). Therefore, the Hessian matrix can be approximated by

$$\Phi'' = [\mathbf{f}']^T \mathbf{f}' \tag{3.27}$$

and the following can be obtained:

$$\Delta r^k = -\left[[\mathbf{f}'(r^k)]^T \mathbf{f}'(r^k)\right]^{-1} [\mathbf{f}'(r^k)]^T [\mathbf{f}(r^k) - u_0] \tag{3.28}$$

This equation defines an iterative procedure to find r^*. At iteration k with the current estimate r^k, we solve equation (3.28) and update our estimate of r^* to

$$R_{k+1}=r_k + \Delta r_k \tag{3.29}$$

Implementation

The key part of implementing the N_R algorithm is the calculation of the Jacobian matrix. The Jacobian matrix f' here is calculated using the so called Standard Method. More detail is given else where.[Yorkey *et al* 1987]

If the Jacobian matrix is obtained, it is easy to update the impedance distribution iteratively using equation (3.29).

It should be noted that if Jacobian matrix J is square, equation (3.28) is reduced to the same form as in equation (3.18) or more generally, (3.21).

3.4 Image Reconstruction Algorithms: Performance Comparison

In order to choose an appropriate image reconstruction algorithm for EIT breast imaging, a comparison of different algorithms is desirable. How well the reconstructed image can reflect the resistivity distribution of the imaged object is of the most importance for breast imaging. In the following study, the image quality for the three algorithms is compared with different computer simulation objects, followed by the discussion of some other requirements by breast imaging.

3.4.1 Simulation settings

Four computer simulation objects (as shown in Figure 3.2) were made. Every of the first three objects has two abnormalities in a uniform background. The two abnormalities in object 1 are on the boundary and far away from each other. The distance of the 2 abnormalities in object 2 are closer than that of object 1. And in object 3, the two abnormalities are near the centre and are very close. The imaging results of such simulation objects help to give some idea on the distinguishbility of the two abnormalities when their relative position changes. The spatial resolution of EIT is generally space-variant, which means that abnormalities near the boundary (where the electrodes are located) can be well reconstructed while those near the centre cannot. Therefore, in simulation object 4 there are 3 abnormalities located at the centre, in the middle of the radius, and near the boundary respectively. This is a "difficult" object for the algorithms and gives further information on the performance of the algorithms.

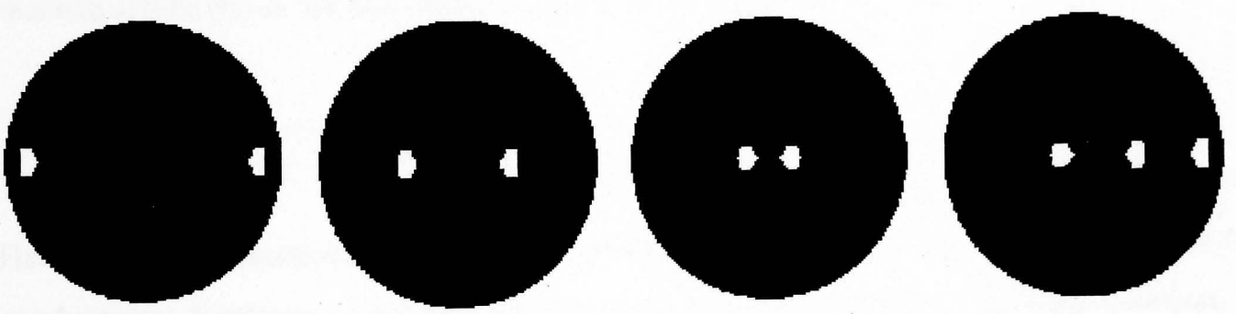

(a) *(b)* *(c)* *(d)*

Figure 3.2 Simulation objects

(a) Simulation object1; (b) Simulation object2; (c) Simulation object3; (c) Simulation object4;

Simulation measurements were calculated for each of the simulation objects with FEM method, using 32 equally-spaced electrodes each of which injects current as well as

measures the voltage. The current injection and the voltage measurement are carried out on the adjacent electrodes.

BP and GI algorithms produce difference images, which use the difference of two sets of data, one of which is background data and the other is the foreground data. In order to compare the results by different algorithms, we only do a one-step N_R iteration and use the Δr^k in equation (3.28) as the outcome image. Therefore all the images reconstructed are difference images and are comparable.

For the back-projection algorithm, the following study only uses the simple back-projection without the filter in that the filtered back-projection algorithm is substantially similar to one step N_R algorithm. Care was taken to apply the same regularization level to GI and N_R algorithms so that their results are comparable.

The images were reconstructed with both noise-free data and noise-added data. The reconstruction errors are calculated for each image, defined as follows:

$$Error = mean\ (\ \Sigma |\ (\rho i\ -\ \rho_0 i\ )\ |\ ) \qquad (i = 1 \sim N) \tag{3.30}$$

Here ρ is the normalised reconstructed conductivity distribution, ρ_0 is the normalised real conductivity distribution. N is the element number of the mesh for image reconstruction.

3.4.2 Imaging results with noise-free data

Firstly noise free data are used for image reconstruction. Results are shown in Figure 3.3 ~ 3.6.

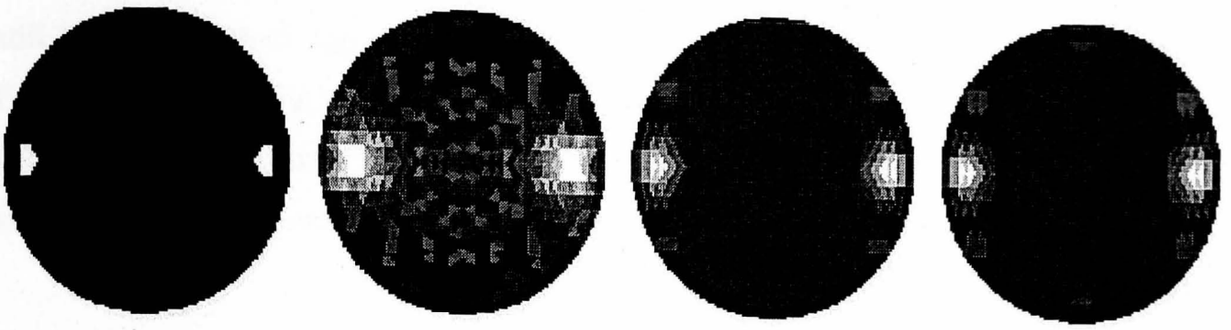

(a) *(b)* *(c)* *(d)*

Figure 3.3 Simulation object 1 and noise-free reconstructed images
(a) Simulation object1; (b) Image by BP; (c) Image by GI; (d) Image by Modified N_R.

From Figure 3.3 it can be seen that all the three reconstructed images are able to show the 2 abnormalities on the boundary. For the image by back-projection algorithm, there are some artefacts around the abnormalities. For the images by the other two algorithms, they look similar with less artefacts. These can be reflected by the image reconstruction errors for the 3 images (Figure 3.3 (b)(c)(d)), which are 0.7738, 0.2029, and 0.2136 respectively.

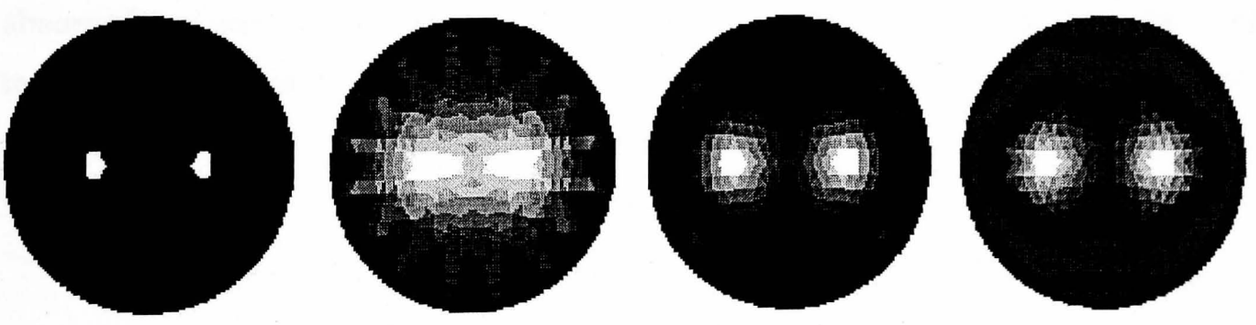

(a) *(b)* *(c)* *(d)*

Figure 3.4 Simulation object 2 and noise-free reconstructed images
(a) Simulation object2; (b) Image by BP; (c) Image by GI; (d) Image by Modified N_R.

From Figure 3.4 it can be seen that for all images, although the 2 abnormalities can still be distinguished, the ring artefacts around the abnormalities are greater than those in Figure 3.3, due to the fact that the two abnormalities are nearer to the centre. The image with BP algorithm has more artefacts than the other two, which can be reflected by the image reconstruction errors which are 0.7319, 0.1492, and 0.1910 respectively.

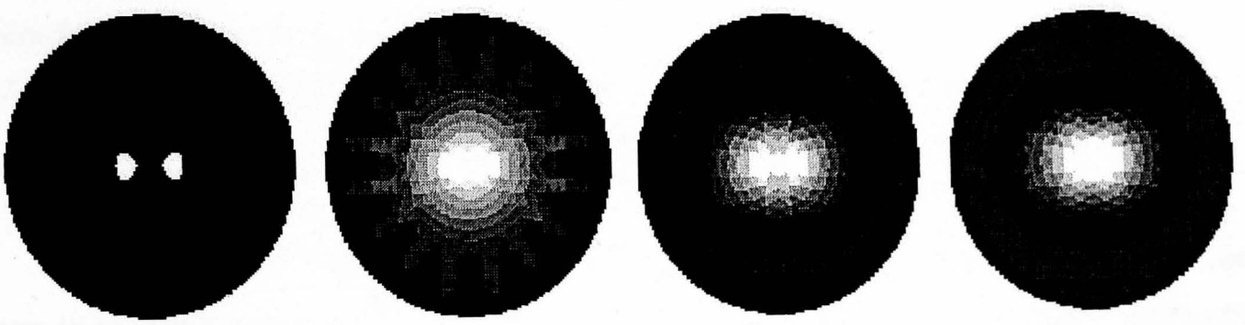

(a) *(b)* *(c)* *(d)*

Figure 3.5 Simulation object 3 and noise-free reconstructed images
(a) Simulation object 3; (b) Image by BP; (c) Image by GI; (d) Image by Modified N_R.

From Figure 3.5 it can be seen that all the images cannot distinguish the two abnormalities very well. All the images mix the two abnormalities together. The image reconstruction errors for the 3 images (Figure 3.5 (b)(c)(d)) are 0.8024, 0.1719, and 0.2071 respectively.

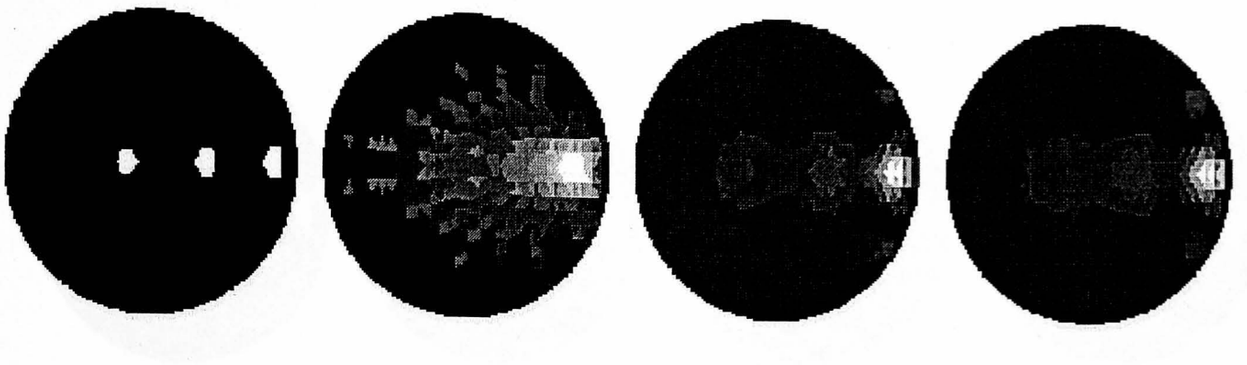

(a) *(b)* *(c)* *(d)*

Figure 3.6 Simulation object 4 and noise-free reconstructed images
(a) Simulation object 4; (b) Image by BP; (c) Image by GI; (d) Image by Modified N_R.

From Figure 3.6 it can be seen that in all the images the abnormality near the image centre is overshadowed by the presence of the abnormalities near the boundary. Although three images are still able to show the three abnormalities, the conductivity value for the 2 abnormalities near the image centre is very much attenuated, which shows the spatial variance property of the EIT image reconstruction. The image reconstruction errors for the 3 images (Figure 3.6 (b)(c)(d)) are 0.8075, 0.2034, and 0.2165 respectively.

3.4.3 Imaging results with noise added data

Images with noise added data are reconstructed and shown in Figure 3.7 ~ 3.10. The standard deviation of the noise (Gausian noise) is 0.1% of the minimum adjacent measurement.

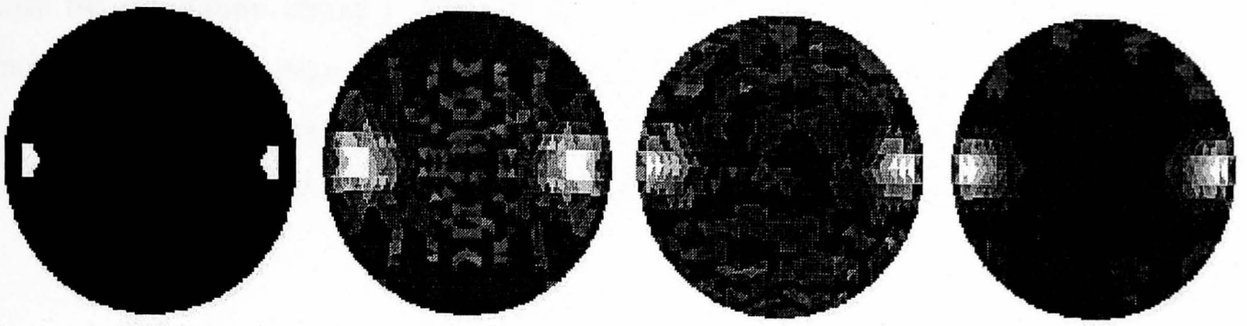

(a) (b) (c) (d)

Figure 3.7 Simulation object 1 and reconstructed images with 0.1% noise added
(a) Simulation object 1; (b) Image by BP; (c) Image by GI; (d) Image by Modified N_R.

From Figure 3.7 it can be seen that although all the images can distinguish the two abnormalities, they are all affected by the noise to some degree. The image by GI algorithm was mostly affected. The image reconstruction errors for the 3 images (Figure 3.7 (b)(c)(d)) are 0.7260, 0.2723, and 0.2388 respectively.

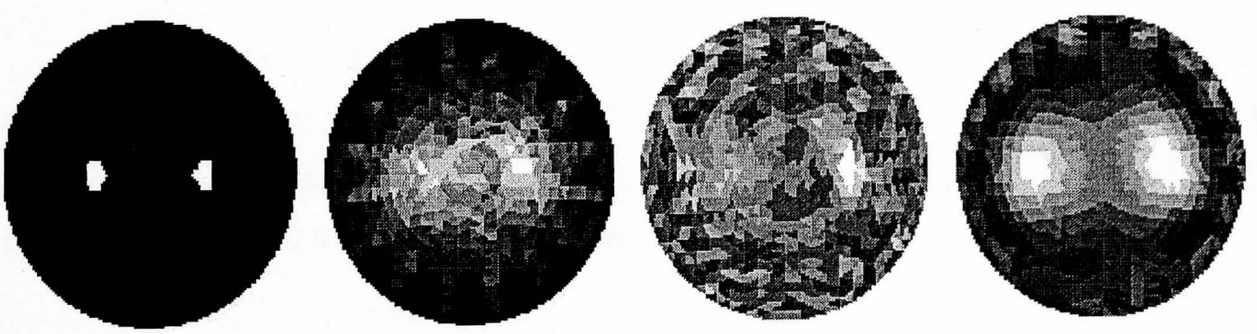

(a) (b) (c) (d)

Figure 3.8 Simulation object 2 and reconstructed images with 0.1% noise added
(a) Simulation object 2; (b) Image by BP; (c) Image by GI; (d) Image by Modified N_R.

From Figure 3.8 it can be seen that the images are all more affected by the noise than those for simulation object 1. This is because that the abnormalities near the centre have smaller sensitivities than those near the boundary. In the three images, only the one by modified N_R can show the 2 abnormalities very well. The image reconstruction errors for the 3 images (Figure 3.8 (b)(c)(d)) are 0.7216, 0.4819, and 0.3985 respectively.

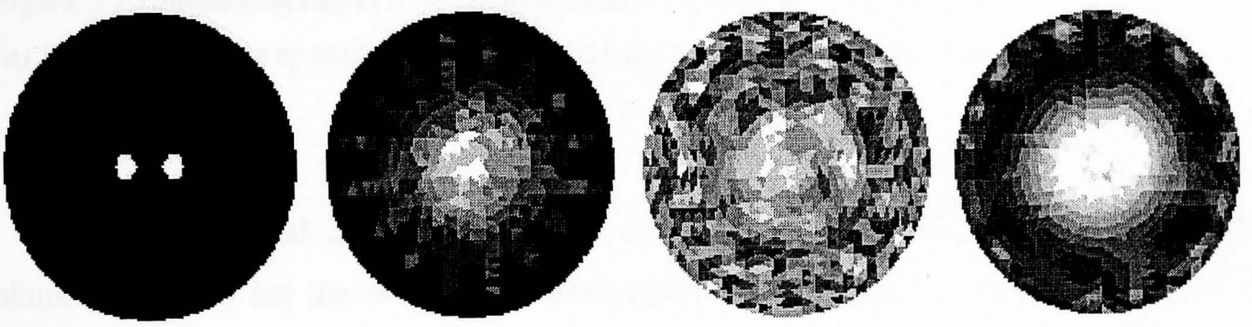

(a) *(b)* *(c)* *(d)*

Figure 3.9 Simulation object 3 and reconstructed images with 0.1% noise added
(a) Simulation object 3; (b) Image by BP; (c) Image by GI; (d) Image by Modified N_R.

From Figure 3.9 it can be seen that all the images cannot show the 2 abnormalities. In the three images, the image by modified N_R shows the best results. The image by GI is mostly affected by the noise. The image reconstruction errors for the 3 images (Figure 3.9 (b)(c)(d)) are 0.7714, 0.5670, and 0.4282 respectively.

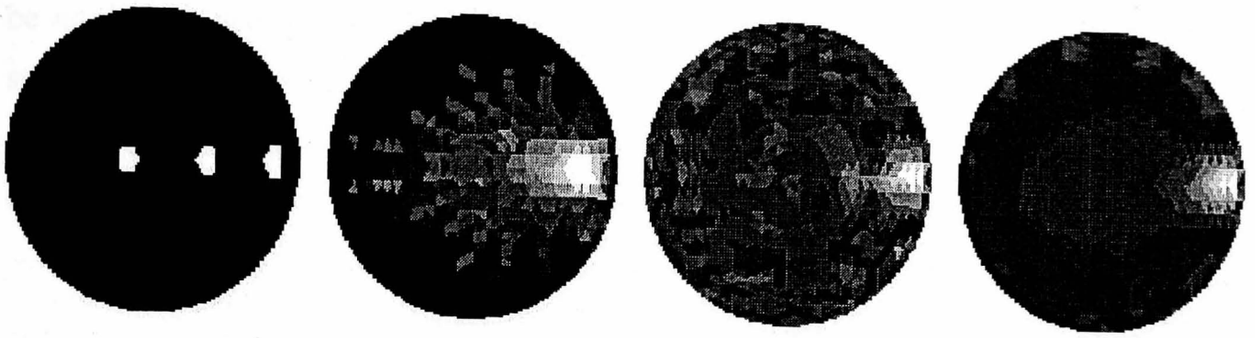

(a) (b) (c) (d)

Figure 3.10 Simulation object 4 and reconstructed images with 0.1% noise added
(a) Simulation object 4; (b) Image by BP; (c) Image by GI; (d) Image by Modified N_R.

From Figure 3.10 it can be seen that all the images are able to show the boundary abnormality, but for the other two abnormalities near the centre, none of them are. The image by GI is still the one affected most by noise, while the image by BP still has more artefacts. The image reconstruction errors for the 3 images (Figure 3.10 (b)(c)(d)) are 0.8056, 0.2995, and 0.2601 respectively.

3.4.4 Comparison

Table 3.1 shows the image reconstruction errors for the four simulation objects. From the table it can be seen that both the GI and the N_R algorithms show smaller errors whether noise is added in the data or not. The error for N_R is slightly bigger than GI for the noise-free data, but slightly smaller than GI for the noise-added data. This is likely due to the regularization. Although a similar regularization parameter is used for N_R and GI, the different formulation of these two algorithms can still result in difference in regularization. Increasing the regularization parameter for GI will make it more robust to noise. Therefore in this sense there is no significant difference between the images obtained from these two algorithms. The BP algorithm generally produces more artefacts around the abnormalities and therefore shows a bigger image reconstruction error. However, it should

be noted that due to the using of normalised data, BP algorithm is not very sensitive to some errors such as electrode placement error. This could offer BP algorithm advantage when imaging objects with irregular boundary such as human thorax or head where error in electrode placement is inevitable.

Table 3.1 Image reconstruction errors.

Reconstruction Errors		Simulation obj1	Simulation obj2	Simulation obj3	Simulation obj4
Noise free	BP	0.7738	0.7319	0.8024	0.8075
	GI	0.2029	0.1492	0.1719	0.2034
	N-R	0.2136	0.1910	0.2071	0.2165
Noise added	BP	0.7260	0.7216	0.7714	0.8056
	GI	0.2723	0.4819	0.5670	0.2995
	N-R	0.2388	0.3985	0.4282	0.2601

Besides the image reconstruction errors, other factors should also be considered for evaluating the algorithm performance including time consumption and other practical requirements such as memory requirement and current patterns.

For the time of image reconstruction, because all the algorithms were implemented in one step, and the matrix for image reconstruction can be calculated in advance, so the time required for image reconstruction is the same. N_R and GI algorithm can also be used to reconstruct images iteratively. In this case, N_R algorithm requires an inversion of a square matrix and GI requires a general inversion of a rectangle matrix. In Matlab the former is much quicker than the latter unless the rectangle matrix has one side significantly shorter than the other.

The other requirements, both the GI and N_R algorithms requires more computer memory to do the matrix inversion while the simple BP algorithm does not. But GI and N_R are flexible with the current injection & voltage measurement patterns, and can be

easily adopted in three-dimensional imaging, while BP algorithm requires some specific current patterns and its application to 3D imaging is still largely an open area. Another restriction for BP algorithm is that in its current form whether or not it can produce static images is still an open question.

For breast imaging, although the faster the image reconstruction the better, there is no need for real-time imaging so the image reconstruction time is not the top priority factor. The image quality has the priority.

After initial consideration the BP algorithm was ruled out for breast imaging. Although the BP algorithm has the advantage of being insensitive to electrode placement errors when imaging objects with irregular boundary such as human thorax or head where error in electrode placement is inevitable, for breast imaging the breast can be deformed into a regular shape and the electrode placement error will not be very significant. At the same time, breast imaging requires static images which show the static value of impedance distribution and enable analysis & modelling of the Region Of Interest in multi-frequency images. Since GI and N_R algorithms can produce static images, these two algorithms are considered.

The N_R algorithm was finally chosen as the dedicated algorithm for breast imaging due to the fact that:

1) General inversion in the GI algorithm generally requires more computation time than the inversion of the square matrix in N_R algorithm;

2) N_R algorithm is more generally used in EIT society and using this algorithm makes the results comparable to that of other groups.

3.5 Summary

This chapter described basic studies on image reconstruction algorithms, as a preparation and foundation for the subsequent studies.

The FEM method is firstly introduced and three different EIT image reconstruction algorithms are implemented and compared in order to select an appropriate algorithm dedicated for breast imaging. The comparison is focused on the quality of the reconstructed images, a property that is crucial to breast imaging. Finally other requirements are discussed and the modified N_R algorithm is chosen as the appropriate algorithm to be used for subsequent studies.

CHAPTER 4 THE NUMBER OF ELECTRODES AND BASIS FUNCTIONS IN EIT IMAGE RECONSTRUCTION

In this chapter two important factors in EIT image reconstruction: the number of electrodes (NOE) and the number of conductivity basis functions (NOCBF), are discussed.

In section 4.1, current problems with NOE and NOCBF are raised. Further information about SVD and spectrum expansion is briefly introduced in section 4.2; In section 4.3, theoretical analysis of different combination of NOE and NOCBF is described. In section 4.4, the configuration of simulation studies corresponding to the theoretical analysis is detailed, followed by section 4.5 in which image reconstruction results are presented and discussed. Finally, several conclusions are drawn in section 4.6, followed by a summary section 4.7.

4.1 Introduction

In EIT, many factors affect the image reconstruction results. Among them are the number of electrodes (NOE) and the number of conductivity basis functions (NOCBF) for image reconstruction. The NOCBF generally reflects the density of the mesh based on which image is reconstructed.

As is generally known, increasing the NOE will increase the number of independent measurements, provided that the relative noise level of the measurements remains unchanged. This increase should bring more impedance information to the measurements, as stated in [Dobson *et al* 1994]. However, there is no detailed analysis of how the increase in NOE improves the image reconstruction results. Some studies even suggest that in certain situations increasing NOE may result in a greater ill-posed condition [Gisser *et al* 1990].

For the number of conductivity basis function, it is common to use a number which is same as or less than the independent measurements [Vauhkonen *et al* 1997][Edic *et al* 1998][Wang *et al* 2001], because the degrees of freedom for the solution should be no more than the number of independent measurements. In a L-electrode system where all the electrodes are used for current injection as well as voltage measurement, there are a total of *L(L-1)/2* independent measurements available. Therefore in a 32 electrode system, NOCBF should be no more than 496. If piecewise constant basis functions are used, which is common practice [Edic *et al* 1998][Wang *et al* 2001][Yorkey *et al* 1987], the size of each image unit (element) is about 5% of the diameter of the whole image. Thus the images usually look rough and quantization errors are prominent. Whether the increase in NOCBF is able to improve the situation is a question that has not been studied in detail. It is stated in [Gisser *et al* 1990] that in certain situations increasing the NOCBF may result in a greater ill-posed condition.

In a method reported by [Gisser *et al* 1990] and [Isaacson *et al* 1986] it is suggested that the size of the smallest radial subdivision is chosen to be equal to the size of the smallest circular inhomogeneity that can be distinguished from a uniform background by measurements of precision ε. The number of angular subdivisions is then chosen to be equal to the number of electrodes. Subsequently an equation is derived to calculate the appropriate number of electrodes. This method, however, is only a heuristic method and difficult to apply generally because it is deduced on the basis of having one circular inhomogeneity with resistivity σ in the middle of a uniform background disk. In practice the resistivity distribution is generally much more complicated and the solution of EIT is spatially variant.

Therefore, what is needed is a guideline for how and to what extent do NOE and NOCBF affect the ill-posed condition in image reconstruction and the final images, so that an appropriate configuration can be chosen under this guideline to fit different cases.

Several studies have been done in analysing the ill-posed condition in EIT image reconstruction. The study in [Breckon *et al* 1988] used singular value decomposition (SVD) to analyse this problem when different electrode pairs are used for current injection. The studies in [Allers *et al* 1991][Dobson *et al* 1994] expanded the conductivity distribution in an orthogonal basis involving Zernike polynomials and performed a stability and resolution analysis of the problem, in which stability is addressed by analysing the ill-posed condition in image reconstruction. The study in [Zadehkoochak *et al* 1991] used spectral expansion theory to decompose the solution of the EIT problem into a set of orthogonal basis images. The singular values of the Jacobine matrix and corresponding basis images were then analysed.

The following study uses SVD and spectral expansion theory to analyse in theory the ill-posed problem when NOE and NOCBF are changed, followed by a computer simulation study in which the FEM method is used.

4.2 Singular Value Decomposition (SVD) and Spectral Expansion

Using the SVD technique, a m by n matrix A can be decomposed such that [Watkins 1991]:

$$A = U \Sigma V^T \tag{4.1}$$

Where U is an m by m orthogonal matrix whose columns are the eigenvectors of AA^T, T is the transpose operator, Σ is a m by n diagonal matrix whose non-zero elements are the positive square roots of the eigenvalues of AA^T (or A^TA), or the so-called singular values. The ratio of the largest singular value to the smallest is called the condition number of A. V is an n by n orthogonal matrix whose columns are the eigenvectors of A^TA.

The inverse of matrix A can be written as:

$$R = V \Sigma^{1} U^{T} \tag{4.2}$$

Where Σ^{1} is the inversion of Σ, and U^{T} is the transpose of U. Based on SVD, further analysis using spectral expansion theory can be carried out [Zadehkoochak *et al* 1991]. The method of spectral expansion enables us to expand the solution to the problem of electrical impedance tomography (i.e. the image, x) into a set of n orthogonal basis images ($x_1, x_2 \ldots, x_n$), where n is the number of measurements:

$$x = \sum_{i=1}^{n} a_i x_i \tag{4.3}$$

A key matrix in image reconstruction is the Jacobian matrix, J, or the so-called sensitivity matrix. It describes what changes are to be expected in the measurements as a result of conductivity changes in the object. We define J as an m by n matrix, m corresponds to the number of measurements and n corresponds to the number of elements in the mesh for image reconstruction.

As the procedure of image reconstruction generally involves the inversion of the Jacobian matrix, we firstly decompose it by SVD as shown in equation (4.1). According to the spectral expansion analysis in [Zadehkoochak *et al* 1991], the columns of matrix V (n by n) form n basis images, which have been ordered according to decreasing size of eigenvalues. The columns of U (or the data-space eigenvectors) specify how the data should be combined to produce the coefficients a_i in equation (4.3). Every diagonal element of Σ in SVD, i.e. the singular values, corresponds to a basis image and indicates how much this basis image is affected by the data noise.

It has been shown in [Zadehkoochak *et al* 1991] that the first basis image has all the structures very close to the periphery. As the basis image index increases, the structures become finer and more structures appear in the centre. This means smaller singular values correspond to the finer structures, especially in the image centre.

The problem is that the Jacobian matrix is generally ill-posed, i.e. some of the singular values are much smaller than others. When it is inverted, the reciprocals of these much smaller elements are much bigger and therefore play a dominant role in the image reconstruction. Using them in reconstruction results in the data noise being magnified.

4.3 Theoretical analysis

4.3.1 Image reconstruction algorithm

Before NOE & NOCBF are analysed and their roles in image reconstruction examined, a brief introduction of the image reconstruction algorithm used in this study; the Modified Newton-Raphson algorithm [Yorkey *et al* 1987][Ortega 1970], is given. In this algorithm, the conductivity distribution σ is updated by the following equation:

$$\sigma_{k+1} = \sigma_k + \Delta\sigma_k \tag{4.4}$$

$$\Delta\sigma_k = -[\,[J(\sigma_k)]^T J(\sigma_k)\,]^{-1}\,[J(\sigma_k)]^T\,[f(\sigma_k) - u_0] \tag{4.5}$$

Here f is a function that maps a conductivity distribution into a set of approximate voltage observations. J is the Jacobian matrix. σ^k is the conductivity distribution after k iterations. u_0 stands for the voltage measurements. Since in this algorithm it is not J but J^TJ which is inverted, the matrix J^TJ should be decomposed and analysed instead of J. Therefore the following analyses are all based on the decomposition of J^TJ, which is a square matrix. In fact, as far as the singular values are concerned, they have the same

number of non-zero singular values and the non-zero singular values for J^TJ are the square of those for J. Therefore the J^TJ is usually much more ill-posed than J.

4.3.2 Theoretical analysis with different NOE and NOCBF

The number of independent measurements are denoted by m and the number of elements in the reconstruction mesh by n. m can be calculated, as stated before, by $L(L-1)/2$ if the data noise is not considered. Five different situations regarding the values of m & n are now discussed.

When $m=n$

When $m=n$, the number of dimensions for the solution space is the same as the number of independent measurements. Under this situation, matrix J is square. After decomposition of J^TJ, the matrix V which defines the basis images is n by n. In principle the matrix J^TJ is not singular, but generally it is very near singular. So a regularization method has to be used. Regularization here can be deemed as a method to replace the ill-conditioned matrix by a better-conditioned one with some prior information about the solution. The result is that the higher frequency components of the basis images, which have finer structures near the image centre, are manipulated by the prior information. The reconstruction result mainly depends on the singular values and the prior information incorporated in the regularization.

When n remains the same and m is increased

When n remains the same and m is increased, *E.g.* by increasing the NOE, J is no longer square. But after decomposition of J^TJ, matrix V that defines the basis images is still

n by n. The size of Σ and the number of non-zero diagonal elements remain the same, but the singular values change according to the sensitivity changes. Therefore, the change in the imaging result mainly depends on the change in singular values. Improvement in the singular values earlier in the series results in more improvement in the image periphery and later in the series results in more improvement in the image centre. How the image changes is shown in the following simulation study.

When m remains the same and n is increased

When m remains the same as 3.1 and n is increased, E.g. by making the mesh finer, J is no longer square. Under this situation, if we continue the decomposition of J^TJ, matrix V that defines the basis images has a bigger dimension, in other words the results will be sought in a finer subspace. Although the size of Σ increases as well, the number of non-zero diagonal elements of Σ remains unchanged. This suggests 2 results: 1) The image in the periphery may be improved in that the basis images corresponding to the periphery are in a finer subspace. So the shape of the abnormality can be reconstructed more precisely. Although those basis images corresponding to the centre are also in a finer subspace, their corresponding singular value is very small or zero and these basis images cannot be utilised without regularization. 2) As there will be zeros on the diagonal of Σ, this makes the matrix singular and not invertible. However, in general the values of the last non-zero diagonal elements have already been very near zero, so there is no big difference between those non-zero and zero in singular values, therefore they all need to be regularized. In this case, the results depend more on the prior information incorporated in the regularization. Since the results are sought in a finer subspace, if the prior information is correct, the whole image can be improved.

When m is increased while $n>m$

If $n>m$, and then m is increased, but is still less than n. Then the dimension of V, Σ and U remains unchanged, but the number of non-zero diagonal elements (singular values) of Σ increases. The rank of J^TJ increases, which means the condition is improved. Therefore the image will be improved if the improvement in the matrix condition is beyond the regularization level. Here by improvement beyond the regularization level it is meant that there are less singular values greatly affected by regularization. Improvement in the singular values earlier in the series results in more improvement in the image periphery and later in the series results in more improvement in the image centre.

When n is increased while $n<m$

Similarly, if $n<m$, and then n is increased, but still less than m. In this case the dimensions of U, Σ and V all increase, and the number of non-zero diagonal elements (singular values) of Σ increases. The results will be sought in a finer subspace. Therefore the image will also be improved if there are more singular values beyond the regularization level. Similarly, improvement in the singular values earlier in the series results in more improvement in the image periphery and later in the series results in more improvement in the image centre.

4.4 Simulation study

4.4.1 Simulation target

A simulation imaged target with 3 abnormalities in a uniform background was made, as shown in Figure 4.1. Based on this simulation target, EIT images were reconstructed with different configurations of the NOE and NOCBF, which in this study is

the number of elements in the mesh for image reconstruction. In order that the simulation results correspond to the analysis in the previous section, the configurations are made as follows: 1) NOE=16, NOCBF=496; 2) NOE=16, NOCBF=1984; 3) NOE=32, NOCBF=496; 4) NOE=32, NOCBF=1984; 5) NOE=64, NOCBF=496; 6) NOE=64, NOCBF=1984.

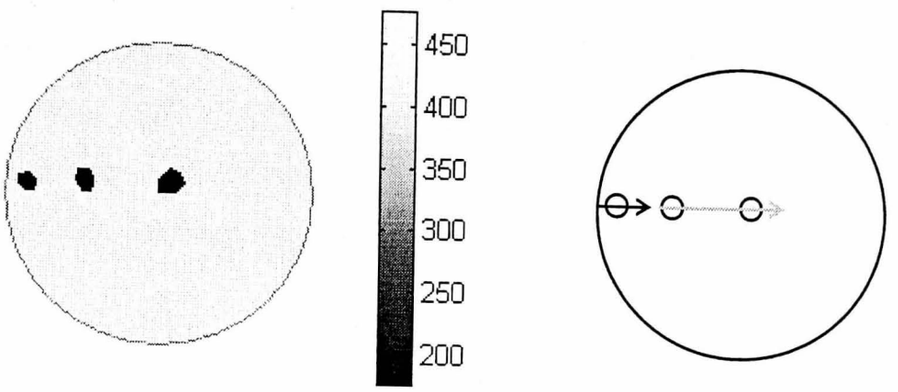

(a) *(b)*

Figure 4.1. Simulation imaged target and ROI profile (disc diameter=320mm)

(a) Simulation target with 3 abnormalities in a uniform background.
Background resistivity: 400 ohm.cm *Abnormality resistivity: 200 ohm.cm*

(b) Description of ROI profile: 2 arrows indicate the route of the ROI profile. first arrow(in black color) indicates the profile across the peripheral abnormality,the second arrow (in grey colour) indicates the profile across the 2 abnormalities near the centre.

4.4.2 Other simulation settings

The EIDORS system [Vauhkonen *et al* 2001] was used to generate the simulation target with different electrode configurations and to solve the forward and inverse problems. This system uses the complete electrode model and reconstructs images by the Modified Newton-Raphson algorithm. In order to isolate the issue of drive patterns from the number of electrodes, optimal current should be used. However, since in this study the

imaged target is almost circularly symmetric except for 3 small abnormalities and since trigonometric current patterns are deemed optimum patterns for a circularly symmetric distribution under certain constraints [Lionheart *et al* 2001][Cheney *et al* 1992], the trigonometric pattern is able to approximate the optimal current pattern in this case. Therefore the current pattern chosen in this study is the trigonometric current pattern, although currently most EIT systems use adjacent pair drives[Wilson *et al* 2001][Vauhkonen *et al* 1999]. The root mean square value of the injected current is the EIDORS system default value, 1. In all cases the forward problem is solved based on a FEM mesh with 1984 elements and 1121 nodes. The electrode covering rate, which is defined as the ratio of the length of electrodes over the length of the space between electrodes, is 50% for every image reconstruction.

In this simulation study only noise-contaminated data is used. The reason is that in EIT the imaging results are greatly affected by the data noise, and the data noise cannot be avoided in real measurements. If noise free data are used, the imaging results can be surprisingly good but of little use in real situations. Normally distributed noise was directly added into the data set in every image reconstruction. The standard deviation of the noise was 0.1% of the corresponding maximum value in one complete measurement set. The measurements were taken on adjacent electrodes. In order to make the comparison fair, for the same number of electrodes, exactly the same noise was used. This is because 2 sets of Gaussian noise which have the same mean and variance may result in significant differences in the final image, especially in the centre where it is most sensitive to noise.

The regularization parameter plays an important role in image reconstruction. Generally, decreasing the regularization parameter may result in better resolution, but can introduce more noise to the image. Further reduction of the regularization parameter can cause the solution to diverge. Choosing the right regularization depth is sometimes quite empirical. In order to make the analysis as scale invariant as possible, the regularization parameter here is quoted as the fraction of the first singular value of the corresponding matrix to be regularized, which is $J^T J$ in equation (4.5). In this study we empirically chose

the regularization parameter as 0.00005. The regularization is a standard Tikhonov regularization with an identity regularization matrix, which has the implicit prior assumption that the conductivity distribution σ is small [Vauhkonen *et al* 1998]. It should also be noted that the choice of basis functions is itself another form of regularization, as used in the paper [Vauhkonen *et al* 1997].

In order to make a fair comparison among different configurations, the elements of each mesh for image reconstruction should have the same size, because differences in the structure of the mesh result in a different ill-posed condition [Tang *et al* 1998]. In this study, all the elements in the mesh are almost the same size except those at the boundary.

The error of the conductivity profile across the Region of Interest (ROI) has been used to quantify the imaging quality. A diagram of the ROI profile is shown in Figure 4.1(b). Here the ROI profile is broken into 2 parts, as shown in Figure 4.1(b). The first part corresponds to the peripheral abnormality, while the second part corresponds to the other 2 abnormalities. This allows us to evaluate the different effects on the image periphery and image centre when NOE and NOCBF are changed. The error of the conductivity distribution across the ROI profile is defined as follows:

$$Error = mean\left(\Sigma \left| \left(\sigma_i - \sigma 0_i \right) / \sigma 0_i \right| \right) \qquad (i = 1 \sim N) \qquad (4.6)$$

Where $\sigma 0$ is the original conductivity distribution along the ROI profile, σ is the reconstructed distribution along the ROI profile, and N is the number of elements (pixels) along the ROI profile. It should be noted that the ROI profile is evaluated on the same mesh which has 1984 triangle elements, despite some images being reconstructed on a mesh of smaller scale.

4.5 Results and discussion

4.5.1 Results of singular values, reconstructed images, and errors across ROI

Although the condition number can be used to evaluate the ill-posed condition of a matrix, we found it here not very useful in that for each NOE and NOCBF configuration, the condition number is very big (at the level of 1e20). Here we display the first 496 singular values for each NOE and NOCBF configuration in Figure 4.2, on a logarithmic scale. The singular values which are not displayed are very small and can hardly affect the

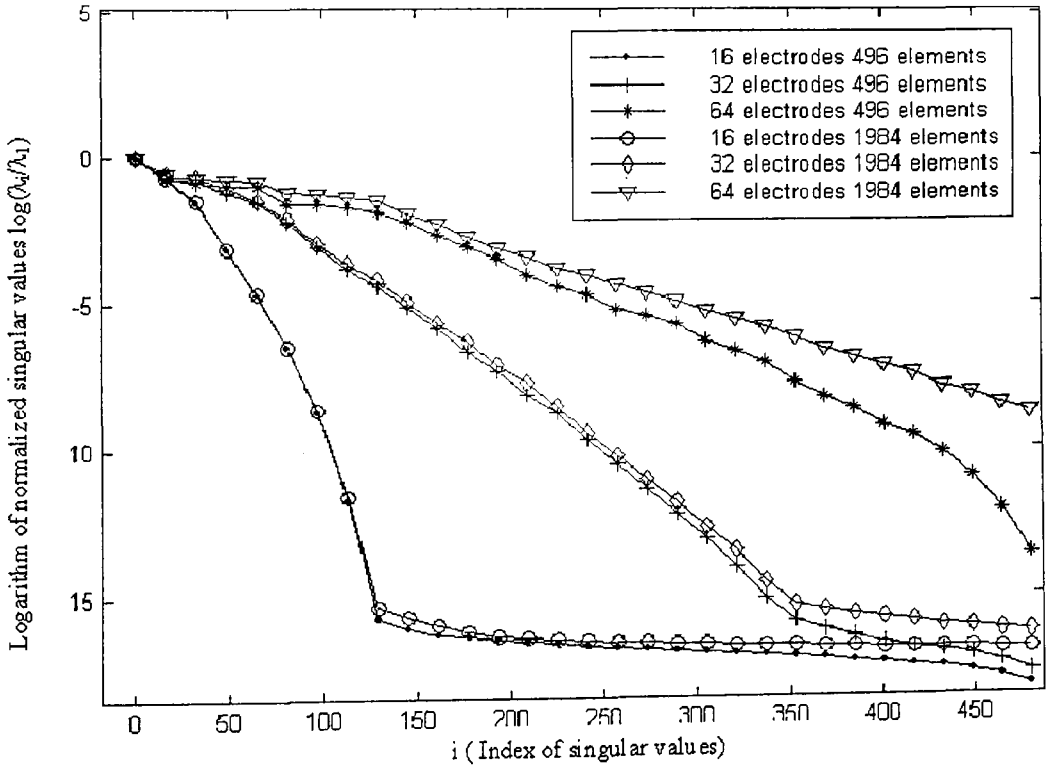

Figure 4.2. First 496 singular values for different configurations of NOE and NOCBF

imaging results. Because the relative ratio of the singular values rather than absolute value decides the condition of the matrix, in Figure 4.2 every set of singular values are firstly normalised by the amximum value within the set.

The singular values displayed here are from the decomposition of matrix J^TJ. In this study the singular values of the matrix J^TJ hardly change during the iterations of Gauss-Newton image reconstruction, therefore the singular values from the first iteration is representative. Consequently only the singular values during the first iteration of image reconstruction are displayed and analysed.

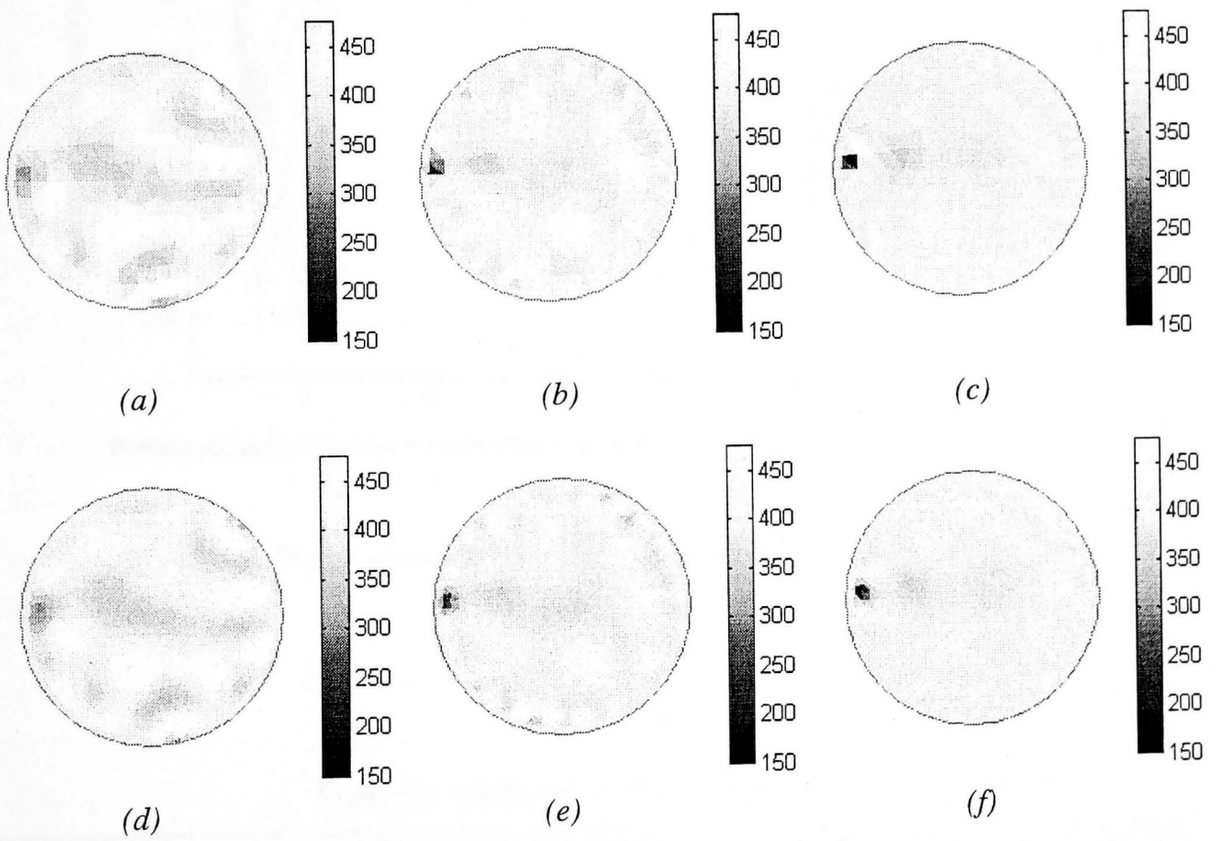

Figure 4.3. Image reconstruction results of different number of electrodes
(Resistivity unit: ohm.cm)
(a) 16 electrodes, 496 elements; (b) 32 electrodes, 496 elements;
(c) 64 electrodes, 496 elements; (d) 16 electrodes, 1984 elements;
(e)32 electrodes, 1984 elements; (f) 64 electrodes, 1984 elements

Figure 4.3 shows the corresponding imaging results. The profile across ROIs is shown in Figure 4.4, while corresponding errors are calculated and shown in Table 4.1.

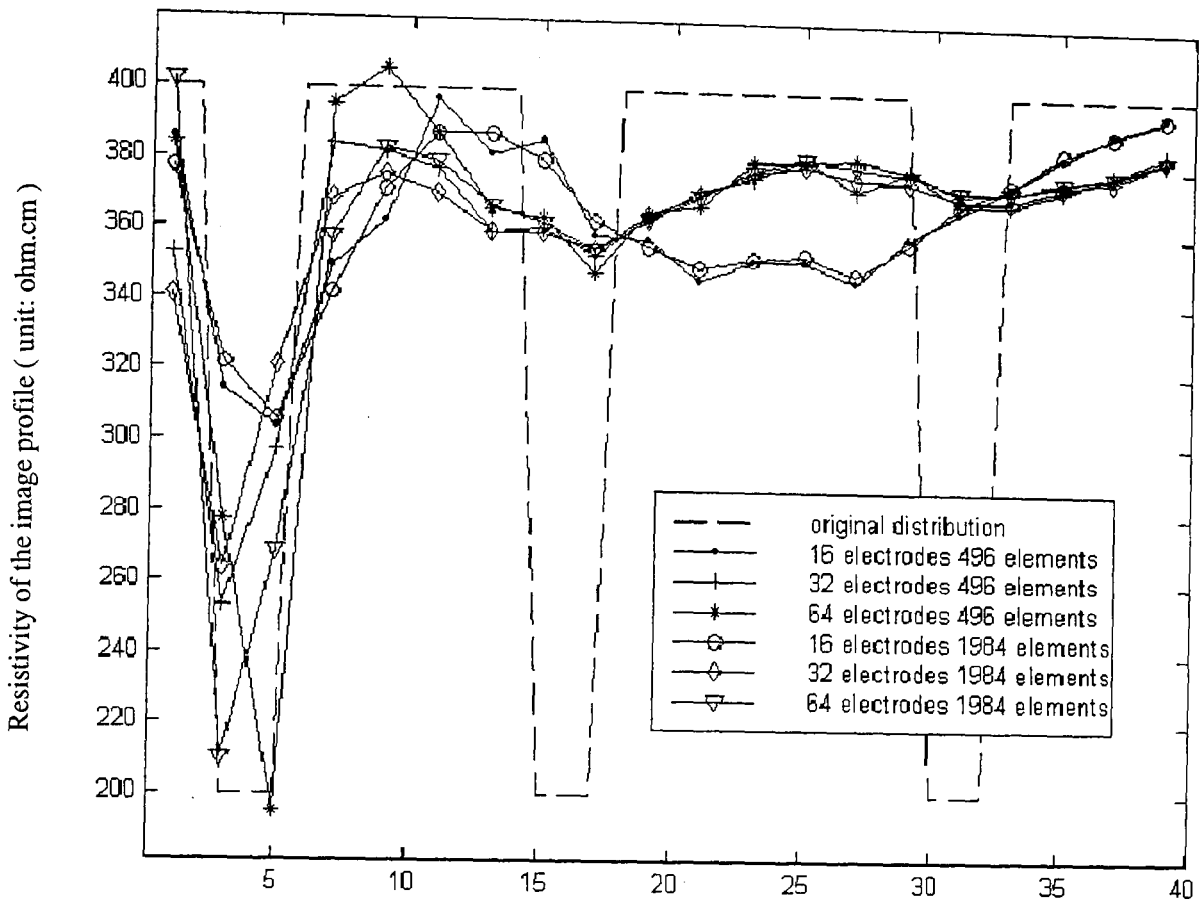

Figure 4.4 Profile across the ROI for different configurations of NOE and NOCBF

Table 4.1. Comparison of the error across the ROI profile

	Errors of Peripheral abnormality		Error of the other 2 abnormalities	
	496 Elements	1984 Elements	496 Elements	1984 Elements
16 Electrodes	0.2367	0.2411	0.2297	0.2301
32 Electrodes	0.2016	0.2149	0.2163	0.2172
64 Electrodes	0.1154	0.1197	0.2131	0.2147

4.5.2 Discussion

From the results obtained the following comments are made:

When *m=n=496* and *m* is increased

When *m=n=496* (32 electrodes and 496 elements), and *m* is increased to 2016 (64 electrodes), there is a significant improvement in singular values, as shown in Figure 4.2. This suggests a significant improvement in the ill-posed condition. This improvement is mainly due to 1) the increase in *m* brings more independent information; 2) more electrodes for the current source are able to produce a closer approximation to the trigonometric current patterns. So the imaging results have a significant improvement as well, shown in Figure 4.3 (b)(c). Firstly, there is a significant reduction of the noise in the image; secondly, the conductivity value of the peripheral abnormality is much closer to the real distribution. Another improvement is that the two abnormalities near the image centre, which cannot be distinguished clearly when *m=496*, are clearly distinguished when *m=2016*. As we said before, improvement in the singular values earlier in the series results in more improvement in the image periphery and later in the series results in more improvement in the image centre. Although from Figure 4.2 it seems all the singular values were improved, only those which are above the regularization level count. Due to the fact that this is a very ill-posed problem and most of the singular values are below the regularization level (here the regularization parameter is 0.005% of the biggest singular value), only the effects of the improvement in the first few singular values are seen. Therefore there is more improvement at the image periphery than in the image centre. This can be reflected by the errors of the conductivity profile across the ROI. The errors of both the peripheral abnormality and the other two abnormalities decreased. For the peripheral abnormality, there is a great error decrease from 0.1816 to 0.1154, but for the other two abnormalities near the image centre, the decrease is marginal, from 21.63 to 21.31.

When *m=n=496* and *n* is increased

When *m=n=496* (32 electrodes and 496 elements) and *n* is increased to 1984, from Figure 4.2 we can see there is a very marginal improvement in the singular values. On the other hand, because the total number of singular values equals the number of elements and the number of basis images, the total number of singular values increased to 1984 as well. Therefore, in one sense the ill-posed condition is worsened in this case. However, because increasing *n* results in the solution of the problem being sought in a much finer subspace and there is some marginal improvement in the singular values, this suggests some marginal improvements, mainly about the shape of the abnormality, can be expected near the image periphery. As shown in Figure 4.3 (b)(e), the shape of the peripheral abnormality is slightly improved, but the resistivity value goes farther from the real value. The error across the peripheral abnormality in this case increased from 0.2016 to 0.2149, which reflected more about the resistivity value deterioration than the shape improvement. The nearer it is to the image centre, the more it depends on the prior information in the regularization. Since in this case the prior information is that conductivity distribution σ is small, which is not proper prior information, the image centre has no improvement. The error across the 2 abnormalities near the image centre slightly increased from 0.2163 to 0.2172.

When *m=120, n=1984*, and *m* is increased

When *m=120* (16 electrodes) << *n=1984*, and *m* is increased to 496, a significant improvement in the singular values is found. When *m* is further increased to 2016, there is another significant improvement in the singular values. This suggests a significant improvement in the ill-posed condition in this case, and can be seen in is the final images shown in Figure 4.3 (d)(e)(f). The error across the peripheral abnormality decreased greatly from 0.2411 to 0.2149 by the first increase of *m* and to 0.1197 by the second increase of *m*, wile the error across the other 2 abnormalities near the image centre decreased from 0.2301

to 0.2172 by the first increase of m, and further decreased to 0.2147 by the second increase of m. This suggests that both the periphery and the centre of the image are improved. Similarly, there are more improvements near the periphery than near the image centre.

When *n=496, m=2016*, and *n* is increased

When $n=496 << m=2016$, and n is increased to 1984, a significant improvement in the singular values is found, however in a sense the ill-posed condition becomes worse when n is increased. Under such conditions, improvements in the shape of the abnormality may be expected near the image periphery, but the image centre has no significant improvement other than being more affected by the regularization. As we can see from Figure 4.3, with the increase of n, the shape of the peripheral abnormality became closer to the true distribution, but the conductivity value actually went slightly farther from the true value. This is reflected by the errors across the ROI profile. For the peripheral abnormality, the error increased slightly from 0.1154 to 0.1197, while for the other 2 abnormalities, the error also increased slightly from 0.2131 to 0.2147.

Table 4.2. Comparison of image reconstruction time per iteration step

	496 Elements	1984 Elements
16 Electrodes	8.7320	86.815
32 Electrodes	24.615	193.65
64 Electrodes	92.453	707.49

(unit: second)

The time spent in image reconstruction increases significantly when NOE or NOCBF is increased. Table 4.2 shows the time requirement of a single iteration for different NOE and NOCBF configurations.

4.6 Conclusions:

Based on the above study, the following conclusions can be drawn:

1) Changing 2 factors, NOE and NOCBF in image reconstruction, is able to affect the singular values of matrix $J^T J$ and therefore the ill-posed condition in EIT. However, because EIT is a seriously ill-posed problem and regularization must be involved, only a small part of the singular values actually affects the image reconstruction results;

2) For a circular plane object with electrodes evenly distributed around the boundary, increasing the NOE is able to improve the ill-posed condition and hence improve the image. Generally more improvement is expected near the image periphery than in the image centre. This improvement also has some conditions, which are 1) The relative noise level in the measurements is fixed; 2) Trigonometric current patterns are used;

3) In the case of breast imaging particularly, in order to improve the image quality near the centre which is the high incidental area for breast cancer, as many as possible electrodes should be used, provided that the electrodes are placed in a 2D ring around the breast;

4) It should also be noted that increasing the NOE results in some practical problems such as the complexity of electrode placement. Given limited space available for placing electrodes, increasing the number of electrodes results in decrease in electrode size, which may increase the contact impedance. Furthermore, the trigonometric current patterns require more current sources when the number of electrodes increases, which raises the cost of the system.

Whether or not the same conclusion can be drawn for pair current injection is still an open question;

5) Increasing the NOCBF generally worsens the ill-posed condition. However, increasing NOCBF enables the solution to be sought in a finer subspace, which can make a closer approximation to the real solution. the image periphery may be improved by increasing NOCBF because the image periphery depends more on the first certain number of singular values. This improvement is mainly to the shape of the abnormality, and the conductivity value usually goes farther from the true value. When the position of the abnormality moves from the periphery to the image centre, the result depends more on the prior information incorporated in the regularization. In all the cases in this study a slight deterioration was observed near the image centre when NOCBF is increased;

6) For breast imaging, since the incident of cancer near the periphery area is low, it is not necessary to use a large NOCBF as only the periphery area of the image can benefit from that.

4.7 Summary

In this chapter two important factors in EIT image reconstruction: the number of electrodes (NOE) and the number of conductivity basis functions (NOCBF), are discussed. The image reconstruction was analysed with different combinations of NOE and NOCBF using Singular Value Decomposition (SVD) and spectrum expansion theory. The analysis corresponds well to the imaging results obtained. This work provides insights into the effects of these two important factors on EIT image reconstruction and represents a significant contribution in this area. A final suggestion is given on which configuration offers better image quality in breast imaging.

CHAPTER 5 SELECTING COMPATIBLE PRIOR INFORMATION IN EIT IMAGE RECONSTRUCTION

This chapter describes the investigation regarding compatibility of different types of prior information and its effect on an iterative image reconstruction algorithm, based on which a new method is proposed to improve EIT image quality by selecting compatible prior information.

In section 5.1, a brief introduction is given to prior information and a currently existing problem is raised. Then a new method to select compatible prior information is proposed in section 5.2. The principle is explained. In section 5.3 simulation studies for implementing this new method are described, followed by section 5.4 where the simulation results utilizing this new method are presented and discussed. Finally a summary is given in section 5.5.

5.1 Introduction

Prior information is important in EIT image reconstruction, which is commonly referred to as the information known about the imaged object and imaging setup before the image reconstruction. It can be information about the shape, internal structure, conductivity distribution of the object and positions of electrodes.

EIT is ill-posed and the image resolution is low [Wheeler *et al* 2002]. It is necessary and useful to apply physiologically meaningful prior information into an ill-posed inverse problem like EIT [Bertero *et al* 1998]. Such prior information can usually be obtained by utilizing information from other sources. For a general example, the boundary shape and internal structure of most parts of human body can be obtained in advance from CT and MRI scan [Bayford *et al* 2001][Borsic *et al* 2001].

For breast imaging, the breast can be easily deformed to get a regular boundary shape. Due to the fact that adipose tissue has a much higher impedance value and that the relative ratio of adipose tissue against stroma in breast generally decreases from boundary to centre, the impedance distribution within breast gives rise to a gradient which is pointing to the centre of breast. This gradient can be estimated according to clinical knowledge and used as a type of internal structure prior information which could be applied to breast imaging.

However, there are still many problems in applying this kind of prior information. For the structure information from CT or MRI, it is bothersome and expensive to let every patient take CT or MRI first before he/she takes EIT. Furthermore, aligning CT or MRI image of every specific patient to EIT image reconstruction is tedious work and experience. Simply using a uniform setting for all patients will produce errors as the shape and structure of the imaged part change from person to person. For thorax imaging, another problem is that the boundary shape of the thorax, lung and heart may change during the measurements.

For breast imaging, although the breast can be easily deformed to a regular shape, due to the volume difference for different people, the three dimensional boundary shape of the breast is still hard to measure accurately. In addition the impedance gradient which could also be used as prior information is only an estimation and could be far from accurate. Applying incompatible prior information in image reconstruction causes errors, many of which are detailed in section 5.2.

However, although the prior information changes from time to time and from person to person, the changes are limited anatomically and physiologically. Therefore, it is possible that the prior information including any possible changes can be presented in a number of variational forms. For example we can define, according to clinical & physiological knowledge, a number of different and representative shapes and internal structure for different part of human body such as thorax, head, and breast.

Then the next question is, which form of prior information is most compatible for a specific subject at the time of imaging?

The following study proposes a new method to deal with this problem. In the proposed method, according to various forms of prior information available, several image reconstruction configurations are designed. Then through monitoring the convergence behaviours through iterative image reconstruction, the configuration with compatible prior information can be found among those different configurations. In order not to lose generality, this method is illustrated with 2 general examples, one was object boundary shape, and the other is the internal structure of the object.

5.2 Principle

5.2.1 Image reconstruction and its sensitivity to noise.

In EIT image reconstruction, one step methods may be used to obtain a difference/static image [Avis *et al* 1995][Cheney *et al* 1999][Le Hyaric *et al* 2000][Tang *et al*, 1998], or an iterative procedure can be used to update the conductivity distribution to obtain a more precise static image [Jain *et al* 1997][Vauhkonen *et al* 2001]. For the iterative method, one step of the image reconstruction can be written as:

$$\rho_{k+1} = \rho_k + \Delta\rho$$
$$\Delta\rho = R \cdot (u - F(\rho_k)) = R \cdot \Delta u \qquad (5.1)$$

Here ρ_k is the estimated conductivity at iteration k. $\Delta\rho$ is a vector of conductivity distribution which updates ρ_k to ρ_{k+1}. R is the image reconstruction matrix, which can be formed differently by different algorithms. u is the boundary measurements. F is the forward solver which calculates the boundary voltages given the conductivity distribution.

The matrix R is the key part of the image reconstruction and is generally the inversion of an ill-conditioned matrix such as a Jacobian matrix or a sensitivity matrix. Generally the

Jacobian or sensitivity matrix is extremely ill conditioned [Tang *et al* 2002] as in EIT the boundary measurements are much more sensitive to the conductivity changes near the electrodes than that near the centre. Therefore in the inverse problem when the Jacobian/sensitivity matrix is inversed, the image near the centre will be extremely sensitive to and greatly affected by noise and errors in the boundary measurements. In practice inversion of the Jacobian/sensitivity matrix cannot be done without any regularization. Regularization is able to make the matrix less ill-conditioned, but the image centre will be more affected by the regularization rather than the data so some information could be lost. Therefore regularization has to be used cautiously so that a balance can be reached between the image resolution and the sensitivity of the system to noise. In such conditions, generally speaking, the reconstructed image is still sensitive to noise.

5.2.2 Errors introduced by incompatible prior information

In EIT image reconstruction, when incompatible prior information is applied, errors occur. The following examples give us some idea of the size of the errors when the boundary shape & internal structure settings in image reconstruction are incompatible with the real imaged object. However, before discussing the errors caused by incompatible prior information, we need to introduce the conductivity basis functions and meshes used in EIT.

For image reconstruction a set of conductivity basis functions need to be defined. In EIT the conductivity distribution of the imaged object is sought numerically in a subspace with a certain number of dimensions. This subspace can be defined by a group of conductivity basis functions. Then the conductivity distribution can be written as:

$$\rho = \sum_{i=1}^{m} c_i \omega_i(x, y) \tag{5.2}$$

Here ρ is the conductivity distribution, m is the number of dimensions, and ω is the

basis function of the conductivities. If these functions are defined as piecewise constant, which is consistent with other studies [Vauhkonen *et al* 1997][Vauhkonen *et al* 1998][Jain *et al* 1997][Wang *et al* 2001], the solution subspace corresponds to a finite element mesh. The dimension of the subspace, or the number of basis functions, equals the number of the elements in the mesh. In this mesh different prior information can be incorporated including the shape and internal structure of the object.

It should be noted that in EIT image reconstruction usually two meshes are involved. The first is the mesh mentioned above, which defines the conductivity basis functions and is usually coarse. The second mesh is a much finer mesh which is used by FEM to calculate the voltage distribution. The reason for this is that the finer mesh for FEM can produce a more accurate voltage distribution, while the coarse mesh for image reconstruction can reduce the dimensions of the problem and greatly ease the computing load. The finer mesh should match the structure of the coarse mesh and before voltage calculation, the conductivity distribution based on the coarse mesh needs to be mapped onto the fine mesh. In the following study, we use the term "coarse mesh" to refer to the mesh corresponding to the conductivity basis functions, while the term "fine mesh" is used to refer to the mesh for calculating the voltage distribution. In general practice the fine mesh is obtained by splitting every element of the coarse mesh so that the two meshes match each other very well.

In the following study, some incompatible prior information is applied to the coarse mesh and then the magnitude of the resulting error is calculated with the fine mesh. In order to show the relative magnitude, firstly the error in the boundary measurements caused by electrode positioning errors was calculated as a reference.

1) Errors caused by the change of electrode position

A circular homogeneous object was made, and the Finite Element Method (FEM) was used to calculate the boundary voltages. The finite element mesh (fine mesh) being used

here has 4608 triangle elements, 2401 nodes, and a diameter of 15cm. 16 electrodes were evenly attached to the circular boundary. The so-called complete electrode model [Cheney *et al* 1999] is used in the calculation. Because the study is in two dimensions, the electrodes only have length, which is 1cm. Currents are injected in trigonometric patterns and the voltage difference between any adjacent 2 electrodes, which is called adjacent measurement, is measured. For 16 electrodes the measurement is a vector of 16*16 = 256, although not all of them are independent. When a complete set of measurements are taken, one of the 16 electrodes is moved along the boundary by a relatively small step of 2.5mm, compared to the diameter (15cm) and the electrode length (1cm) of the object. Then the adjacent measurements were taken again and another vector of 256 measurements were obtained. The difference between the 2 sets of measurements represents the errors caused by the change of electrode position and is also a vector of 256. Instead of using all the 256 elements, the following ratio was used as the indicator of the magnitude of the errors.

$$\text{Ratio} = \max | \text{Meas1} - \text{Meas2} | / \max | \text{Meas2} | \qquad (5.3)$$

Here Meas1 denotes the boundary measurements after the change of electrode position, while Meas2 denotes that before the change.

The calculated results showed that the maximum difference between the two sets of measurements were 0.330 v, while the maximum measurement was 4.65 v. Therefore the error in ratio was 7.09%.

2) Incompatibility in the object boundary shape

As an example a homogeneous simulation, an elliptical object is made with an eccentricity (the ratio of the minor and major axis length) of 0.95, which is close to a circle. The term "Distribution-O" is used to denote the conductivity distribution of this object. Then for image reconstruction, a coarse mesh with a circular boundary is made whose diameter equals the major axis of the simulation elliptical object. If this circular coarse

mesh is used to reconstruct the image of the elliptical object, we can say the mesh has incompatible shape information. The errors caused by this incompatibility are the boundary voltage differences between Distribution-O and a distribution which is based on the circular mesh and is able to best approximate the distribution of the elliptical target. By "to best approximate the distribution" it is meant that the distribution is such that the difference in boundary measurements between it and the Distribution-O is a minimum. The term "Distribution-B" is used to denote this best approximation distribution.

Next, by assuming that this Distribution-B is a homogeneous distribution based on the circular mesh with the same conductivity value as Distribution-O, the differences in the boundary voltages between Distribution-O and Distribution-B, i.e., the error caused by the said incompatibility can be easily calculated.

To calculate the boundary voltages, given the conductivity distribution, the Finite Element Method is used. In this case 32 electrodes were used with trigonometric current patterns and adjacent measurements. A fine circular mesh and a fine elliptic mesh are designed, which correspond to Distribution-O and Distribution-B respectively. Both of the fine meshes have 4608 triangle elements and 2401 nodes. The elliptic mesh is made by compressing the y-coordinates of the circular mesh. The ratio defined in equation (5.3) is still used as the indicator of the magnitude of the errors but this time Meas1 denotes the boundary measurements of Distribution-B, while Meas2 denotes that of Distribution-O.

The calculated error is 4.9%, which is at roughly the same level as that caused by a change in electrode position (7.09%).

It should be noted that the elliptic mesh used was made by compressing the y-coordinates of the circular mesh. Therefore some of the electrode lengths and the spaces between electrodes change after the compression, although the change is limited to 5% maximum. This might make the calculated error larger than it really is. However, the result, 4.9%, is determined by the maximum magnitude of the errors which in this case was found on the measurement involving 2 electrodes on the bottom of the mesh. These two

electrodes are least affected by the compression in geometry, therefore the calculated error of 4.9% was caused primarily by the shape difference.

3) Incompatibilities in the internal structure of the object

In order to calculate the error caused by incompatibilities in the object internal structure, firstly a simulation circular object is designed with a square inhomogenity in a uniform background as shown in Figure 5.1(a). The size of this inhomogenity is 1/256 of the object. The term "Distribution-O" is used to denote this simulation distribution. A circular coarse mesh with 256 elements is designed whose boundary is the same but, whose internal structure cannot match the inhomogenity very well. Specifically, the size of the inhomogenity matches the size of one element in the mesh but their positions have a two-third overlap vertically, as shown in Figure 5.1. Here the term "Element-B" is used to denote this element in the coarse mesh and this Element-B is shown in Figure 5.1(b) and (c). If this mesh is used to reconstruct the image of Distribution-O, the mesh is said to have incompatible prior information. Similarly, the errors caused by this incompatibility are the boundary voltage differences between Distribution-O and a best approximation distribution, which is denoted by the term "Distribution-B".

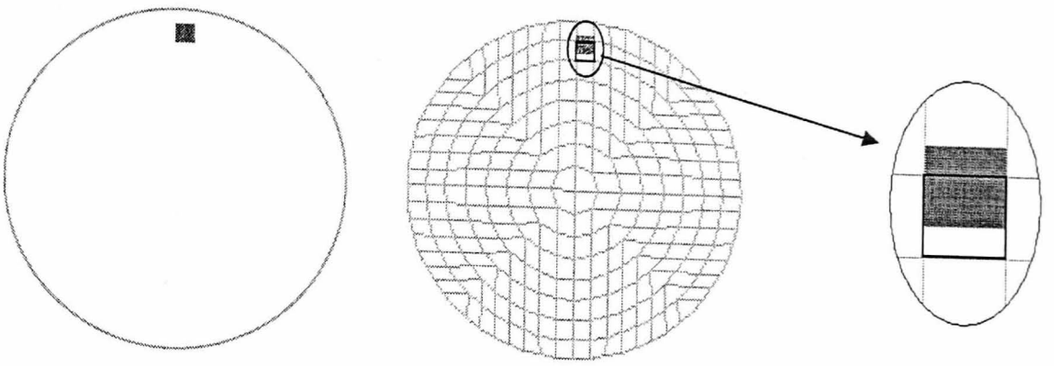

(a) (b) (c)

Figure 5.1. Simulation object and the incompatible mesh

(a) Simulation circular object with a inhomogeneity, Background: 200 Ω.cm, inhomogeneity: 400 Ω.cm;

(b) An incompatible mesh for the simulation object. Greyed square shows the position of the inhomogeneity in (a)

(c) The detail of the incompatibility between the object and the mesh, the square with black boundary indicates the "Element-B"

Due to the fact that Element-B has the most overlap with the inhomogeneity in the simulation object, it is assumed that the said Distribution-B has a square inhomogenity in the position of Element-B in a uniform background with the same conductivity as Distribution-O. The position of Element-B and the relationship with the inhomogeneity in Distribution-O are shown in Figure 5.1(c). It is then relatively easy to calculate the differences in the boundary measurements between Distribution-O and Distribution-B, i.e., the error caused by the said incompatibility.

The finite element method was used to calculate the boundary voltages. In this case 32 electrodes were used with trigonometric current patterns and adjacent measurements. A circular fine finite element mesh is used which has 4608 triangle elements and 2401 nodes. This mesh matches both Distribution-O and Distribution-B.

Again the ratio defined in equation (5.3) is used as the indicator of the magnitude of errors.

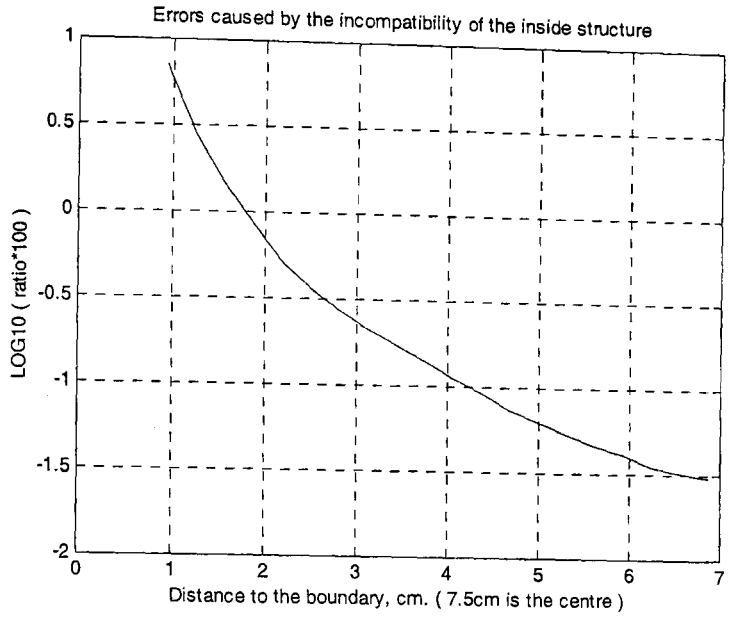

Figure 5.2. Errors caused by the incompatibility of the internal structure of the coarse mesh The y-coordinate shows the logarithm of the percentages of the error. In x-coordinate 0 corresponds to the boundary and 7.5 corresponds to the centre.

It should be noted that in EIT, the sensitivity of the boundary measurements to the changes in conductivity is position-dependent. Near the boundary the sensitivity is high but near the centre it is low. Therefore, the errors calculated are also position-dependent. The errors were calculated when the position of the inhomogenity in Distribution-O and the position of the Element-B in Distribution-B move from the periphery to the centre. Figure 5.2 shows the logarithm of the percentage ratio of the errors. As can be seen from Figure 5.2 the error can be as high as 7% of the maximum measurement near the boundary and as low as 0.03% of the maximum measurement near the centre. The error decreases rapidly when the position is moving towards the centre and is about 0.1% in the middle of the radius.

In conclusion, the results indicate that incompatible prior information can cause significant errors.

It should be noted that in 2) and 3), a best approximation was assumed and in fact it is not the real "best", therefore the errors calculated by the assumptions could be bigger than they really are. However, it is considered that the results from the assumptions are accurate enough to give a representative estimate of the size of the errors caused by such incompatibilities.

5.2.3 Convergence behaviour of the algorithm.

For iterative image reconstruction, the result should generally converge to a best estimation in several steps. As the iteration proceeds step by step, the magnitude of the update conductivity value $\Delta\rho$ should decrease gradually.

As previously reported, the image reconstruction is greatly affected by noise and error in the data. Both noise and data error are able to affect the convergence behaviour of the image reconstruction iterations. More specifically, as seen later in this study, increase of noise and data errors results in an increase in the magnitude of the update conductivity value $\Delta\rho$ in equation (5.1) as the iterations proceed.

It was also previously shown that the application of incompatible prior information was able to cause significant errors in image reconstruction. As a result, the compatibility of the prior information can be reflected by the convergence behaviour of the image reconstruction, unless the errors caused by the incompatibility are much smaller than the system noise or other errors. As shown in the previous part, the errors caused by incompatibilities can be as much as 7% of the maximum measurement, hence these errors are able to play an important role in the behaviour of the image reconstruction algorithm. This phenomenon, therefore, can be used as a criterion to judge whether the prior

information applied in the image reconstruction is compatible with the imaged object.

5.3 Simulation Study

5.3.1 Simulation objects

In this section two simulation objects; A and B are designed, which are shown in Figure 5.3. Object A has three inhomogenities in a uniform elliptic background with an eccentricity of 0.951, while object B also has three inhomogenities but in a uniform circular background. Object A is for studying incompatibility of the boundary shape, while Object B is for studying incompatibility of the internal structure.

In the following study for both objects, the inhomogeneity near the periphery is termed "peripheral inhomogeneity", that in the middle of the radius "middle inhomogeneity", and that near the centre "central inhomogeneity".

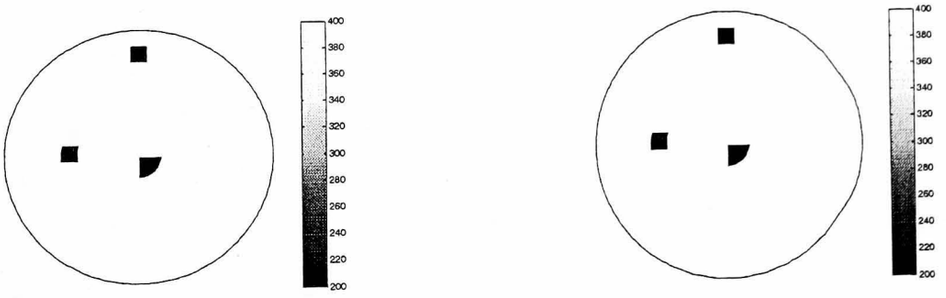

(a) *(b)*

Figure 5.3 Two simulation objects

(a) Simulation elliptic object A with eccentricity of 95.1%. Background: 200 Ω.cm, inhomogeneities: 400 Ω.cm;

(b) *Simulation circular object B. Background: 200 Ω.cm, inhomogeneities: 400 Ω.cm.*

5.3.2 Coarse mesh design

For each of the simulation objects, a set of coarse meshes are designed in which different prior information regarding the object internal structure or shape is incorporated. These meshes have differing degrees of compatibility with the simulation objects.

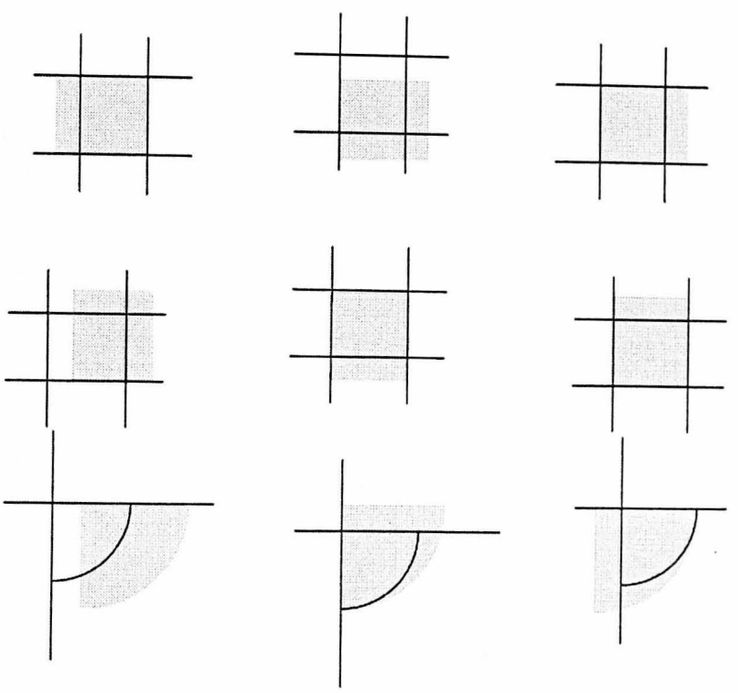

Figure 5.4 The levels of match between simulation B and the 3 coarse meshes
The 1st , 2nd , and 3rd columns show the level of match between the object B and the 1st , 2nd , and 3rd coarse mesh; The 1st , 2nd , and 3rd rows show the level of match between the objects and the coarse meshes at the position of periphery, middle, and central inhomogeneities respectively.

According to simulation object A, three elliptic coarse meshes are designed with an eccentricity of 0.97, 0.95, 0.93 respectively. Although none of these three elliptic meshes can match the boundary object A, the one with an eccentricity of 0.95 is the best approximation to object A which has an eccentricity of 0.951.

According to simulation object B three circular coarse meshes are designed. Every mesh has some level of compatibility to the 3 inhomogeneities in object B. The detail of how the 3 meshes match the 3 inhomogeneities is shown in Figure 5.4. In Figure 5.4 we can see that the 1st mesh and the 3rd mesh match the peripheral inhomogeneity better than the 2nd mesh. The 2nd and the 3rd mesh match the middle inhomogeneity better than 1st mesh. For the central inhomogeneity, the 2nd and the 3rd meshes match it better than the 1st mesh.

5.3.3 *CF* index

In order to monitor the convergence behaviour of the image reconstruction, an index called Change Factor is introduced to reflect the conductivity changes during image reconstruction. This is defined as:

$$CF(j) = \frac{1}{m-1}\sum_{i=2}^{m} \frac{cha(i,j) - \min(cha(i,1 \sim n))}{\max(cha(i,1 \sim n)) - \min(cha(i,1 \sim n))} \qquad (5.4)$$

m: the number of iterations

j: 1 ~ n (n is the number of coarse meshes in image reconstruction)

$cha(i,j)=mean(abs(\Delta\rho(i,j))))$,

$\Delta\rho(i,j)$ is the conductivity update vector for the i^{th} iteration and the j^{th} coarse mesh.

This *CF* index normalizes the conductivity changes during every iteration so that the effect of different iterations is removed and only the conductivity changes during each iteration are taken into account. The change parameter *CF* has n values corresponding to n coarse meshes. By comparing them we are able to choose the most compatible one accordingly.

In practice, when calculating *CF* only the conductivity changes after a certain number of iterations are taken into account, because generally in the first few steps the conductivity

has relatively big changes and for the compatible mesh it may change more. Here in this study we started calculating the *CF* index from the 3rd iteration.

5.3.4 Forward problem

Calculation of the boundary voltages, which is called the forward problem, is needed in both simulation measurement generation and image reconstruction.

For the case of simulation object A, because there are 1 simulation object and 3 coarse meshes and they have difference eccentricities, a total of 4 elliptic fine meshes were designed for the forward problem. All of these 4 fine meshes have 4608 elements and 2401 nodes but different eccentricities, according to the eccentricities of the simulation object and 3 coarse meshes. These fine meshes match their corresponding coarse mesh.

For the case of simulation object B, although there are 1 simulation object and 3 sets of coarse meshes, all of them have the same circular boundary. In this case only one fine mesh was designed for the forward problem, which matches both the boundary and the internal structure of the simulation object as well as the coarse meshes. This fine mesh has 4608 elements and 2401 nodes.

In this study trigonometric current patterns are applied and adjacent voltage measurements are made.

5.3.5 Image reconstruction

Image reconstruction was carried out with noise-free and noise-added data in the EIDORS-2D system, which is a Matlab toolbox to reconstruct two-dimensional EIT images [Vauhkonen 2001]. This system uses the Modified Newton-Raphson algorithm which involves calculating the Jacobian matrix. A simple identity matrix is used to regularize the

ill-posed condition in image reconstruction. It was found that the image reconstruction could get better results if the regularization parameter, which determines the depth of the regularization, started from a slightly larger value and decreases after each iteration [Vauhkonen *et al* 1998]. Therefore in this study, the regularization parameter starts at 0.01 and decreases by a factor of 10 for the first few iterations, and then remains the same for the remaining iterations. There are a total of 4 groups of image reconstruction involving 2 simulation objects and 2 noise levels. For the same group the same regularization configurations are used so that the results are comparable. The regularization details are shown in the Figure 5.5-5.8.

The noises added in the data are normally distributed noises with a STD of 0.1% of the maximum adjacent measurement.

For the simulation study, we define the image reconstruction errors as follows:

$$Error = mean\left(\left| (\rho_i - \rho_{0i})/\rho_{0i} \right| \right) \qquad (i = 1 \sim N) \qquad (5.5)$$

Here ρ is the reconstructed conductivity distribution, ρ_0 is the real conductivity distribution. This error is calculated with the fine mesh, which matches both the simulation objects and the coarse meshes. N is the number of elements in the fine mesh.

5.4 Results

5.4.1 Noise free simulation results

For the simulation object A, 3 images were reconstructed corresponding to the 3 sets of coarse meshes. There are 8 iterations in every image reconstruction. The mean of the conductivity changes cha(i,j) in equation (5.4) for 3 coarse meshes and 8 iterations are shown in Table 5.1. The change factor for each coarse mesh is also shown in the Table 5.1.

Table 5.1. The conductivity changes during image reconstruction of A (noise free)

	Ecc*=0.97	Ecc=0.95	Ecc=0.93
1st iteration	*45.5636*	*45.9907*	*46.1252*
2nd iteration	*17.8538*	*5.5025*	*20.3168*
3rd iteration	*8.6029*	*1.3697*	*11.6317*
4th iteration	*6.8658*	*0.8224*	*8.9872*
5th iteration	*7.4673*	*0.6067*	*8.2509*
6th iteration	*7.7591*	*0.4854*	*6.9927*
7th iteration	*7.3322*	*0.4114*	*5.1237*
8th iteration	*6.0560*	*0.3654*	*3.7385*
Change factors	**0.7632**	**0**	**0.7383**

**Ecc: eccentricity defined by the coarse meshes*

From the Table 5.1 it can be seen that:

a) Generally speaking, as the iteration continues, the conductivity changes decrease.

b) From the 2nd step on, the most compatible coarse mesh, which has an eccentricity of 0.951, shows a significantly smaller value in conductivity changes than the other 2 sets.

c) The change factor for the mesh with eccentricity of 95.1% is 0, while for the other two meshes, the change factors are 0.7632 and 0.7383. These results strongly support the compatible mesh as opposed to the incompatible ones.

Figure 5.5 shows 2 images which correspond to the 2 coarse meshes with eccentricities of 95.1% and 97%. The other image looks similar to Figure 5.5(b) and in order to save

space, it is omitted. It can be seen that the best image quality was obtained when the mesh has an eccentricity of 95.1%, which is most compatible with the object A. The image reconstruction errors are 0.0280, 0.1342, and 0.1466. These results show that the proposed method is able to select, from 3 candidate coarse meshes which have different shape information, the most compatible one.

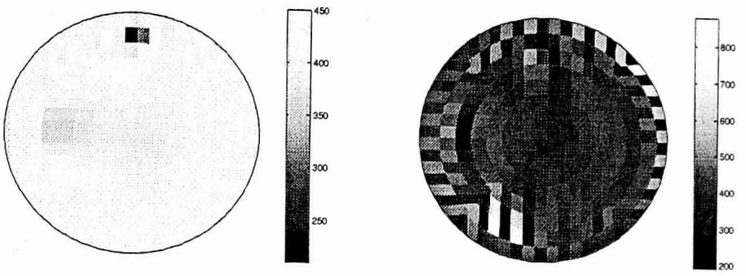

(a) *(b)*

Figure 5.5: The imaging results of simulation object A, noise free.
(a) Result of the mesh with eccentricity of 95%., regularization level=1e-3
(b) Result of the mesh with eccentricity of 97%., regularization level=1e-3

There are significant errors in Figure 5.5(b) which are due not only to the error caused by the incompatible shape, but also to the electrode positioning errors when the eccentricity of the mesh is changed, as mentioned in section 2. Here the question why the image is not usually so noisy in practice even when the shape or position of electrodes is wrong can be posed. It is considered that it is mainly because of the regularization level. Here the same regularization level is maintained for all the 3 image reconstructions so that their results are comparable. In practice when the shape or electrode position is wrong we usually use more strict regularization so that the image still appears reasonable.

For the simulation object B, 3 images were reconstructed as well. The mean of the conductivity changes cha(i, j) for 3 coarse meshes and 8 iterations are shown in Table 5.2. The change factors are also shown in the Table 5.2.

From Table 5.2 a similar result can be seen:

a) Generally speaking, as the iteration continues, the conductivity changes decrease. The only increase in step 3 is due to the decrease of the regularization parameter.

b) From the 2nd step on, the 2nd mesh shows a significantly bigger value in conductivity changes than the other 2 meshes, even though the 2nd mesh matches the middle and central inhomogeneities better than the 1st mesh. This is because this mesh cannot match the peripheral inhomogeneity of object B and the incompatibility near the periphery causes bigger errors than that near the centre.

c) Although as shown in Figure 5.4 that the 1st mesh and the 3rd mesh have the same compatibility for the peripheral inhomogeneity in object B, the 3rd mesh matches the middle inhomogeneity better than the 1st mesh, therefore the final change factors suggest that the 3rd mesh is the most compatible mesh for simulation distribution B.

Table 5.2 The conductivity changes during image reconstruction of B (noise free)

	1st mesh	2nd mesh	3rd mesh
1st iteration	47.9338	48.9849	47.9537
2nd iteration	3.1833	6.1311	3.0982
3rd iteration	4.1522	9.8419	3.5604
4th iteration	2.2071	5.7348	1.6576
5th iteration	1.5259	4.2152	1.0828
6th iteration	1.0432	3.5346	0.7903
7th iteration	0.7910	3.0886	0.6208
8th iteration	0.6497	2.7556	0.5047
Change factors	**0.0851**	**0.857**	**0.000**

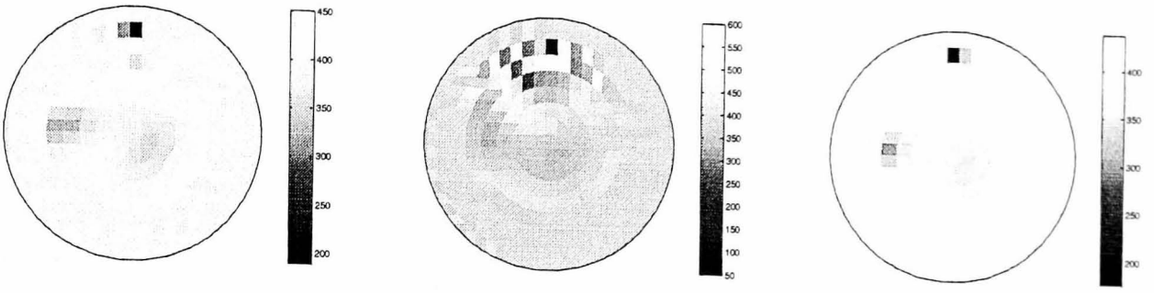

(a) *(b)* *(c)*

Figure 5.6: The imaging results of simulation object B, noise free.

(a) Result of the 1st mesh, regularization level=1e-5

(b) Result of the 2nd mesh, regularization level=1e-5

(c) Result of the 3rd mesh, regularization level=1e-5

Figure 5.6 shows the 3 images which had been reconstructed. It can be seen that the image quality is best for the most compatible mesh. The 1st mesh also produced good image quality. The quality of the three images corresponds well to the change factors. The image reconstruction errors for the 3 images are 0.0334, 0.0729, and 0.0278 respectively.

These results show that the proposed method does not treat the internal structure fairly. It favours the periphery over the centre area. In this case it recognized the mesh which least matches the periphery of the object, although it matches the other 2 inhomogineities well. This is a limitation of the proposed method when it is used to select the compatible information of the internal structure of the object. However, as far as the image quality is concerned, the proposed method is still successful as it selected the mesh which produced the best image. Furthermore, the proposed method could be especially useful, for example, in head imaging to select a best match for the structure of skull.

5.4.2 Simulation with noise added

For the simulation distribution A, 3 images were reconstructed with 3 corresponding coarse meshes. The mean of the conductivity changes cha(i, j) for the 3 coarse meshes and 8 iterations are shown in Table 5.3. The change factors are also shown in Table 5.3.

Table 5.3. The conductivity changes during image reconstruction of A (0.1% noise)

	Ecc*=0.97	Ecc=0.95	Ecc=0.93
1st iteration	45.5422	45.9692	46.1036
2nd iteration	17.7839	5.7952	20.6187
3rd iteration	9.1210	2.0499	11.9680
4th iteration	8.0542	1.4186	9.4359
5th iteration	9.2212	1.1087	8.5615
6th iteration	9.1851	0.9365	6.9552
7th iteration	7.2417	0.8285	5.0054
8th iteration	4.9670	0.7574	3.6207
Change factors	**0.7915**	**0**	**0.7114**

From the Table it can be seen that:

a) Similar to that in noise-free case, as the iteration continues, the conductivity changes generally decrease;

b) From the 2nd step on, the most compatible coarse mesh with an eccentricity of 0.95 still has the smallest conductivity changes;

c) The change factors for the 3 coarse meshes are 0.7915, 0, and 0.7114 respectively, which still strongly identifies the most compatible one.

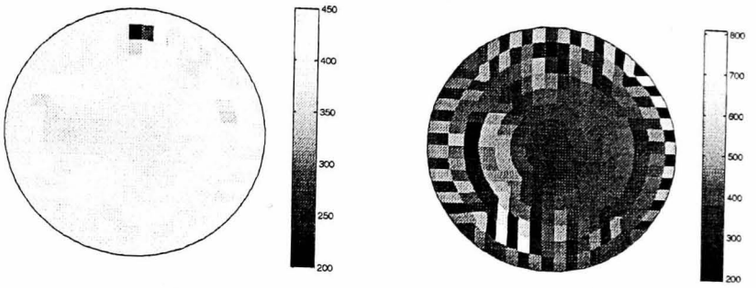

(a) *(b)*

Figure 5.7: The imaging results of simulation object A, 0.1% noise.

(a) Result of the mesh with eccentricity of 95%., regularization level=1e-3

(b) Result of the mesh with eccentricity of 97%., regularization level=1e-3

Figure 5.7 shows 2 images, which corresponds to the eccentricity of 0.95 and 0.97. The image reconstruction errors for the 3 images are 0.0390, 0.1472, and 0.1508 respectively.

For simulation distribution B, 3 images were reconstructed with 3 corresponding coarse meshes. The mean of the conductivity changes cha(i, j) for the 3 coarse meshes and 8 iterations are shown in Table 5.4. The change factors are also shown in Table 5.4.

Table 5.4 The conductivity changes during image reconstruction of B (0.1% noise)

	1st mesh	2nd mesh	3rd mesh
1st iteration	47.9285	48.9893	47.9437
2nd iteration	1.8965	3.1081	2.0655
3rd iteration	1.1449	1.8192	1.2204
4th iteration	0.9704	1.4291	0.9880
5th iteration	0.8560	1.2110	0.8498
6th iteration	0.7758	1.0688	0.7582
7th iteration	0.7105	0.9624	0.6990
8th iteration	0.6572	0.8817	0.6493
Change factors	**0.0217**	**0.8571**	**0.0215**

From the Table 5.4 it can be seen that:

a) Similar to that in noise-free case, as the iteration continues, the conductivity changes generally decrease;

b) From the 2nd step on, the change factor is still able to pinpoint the most incompatible coarse mesh. However, because the incompatibility degree for the inhomogenity near the periphery is the same for both cases, the change factors for the 1st mesh and 3rd mesh are very close, which are 0.0217 and 0.0215. This suggests that in the presence of 0.1% noise, the errors caused by the structure incompatibility in the position of the middle abnormality cannot make enough difference to clearly distinguish the 2 coarse meshes.

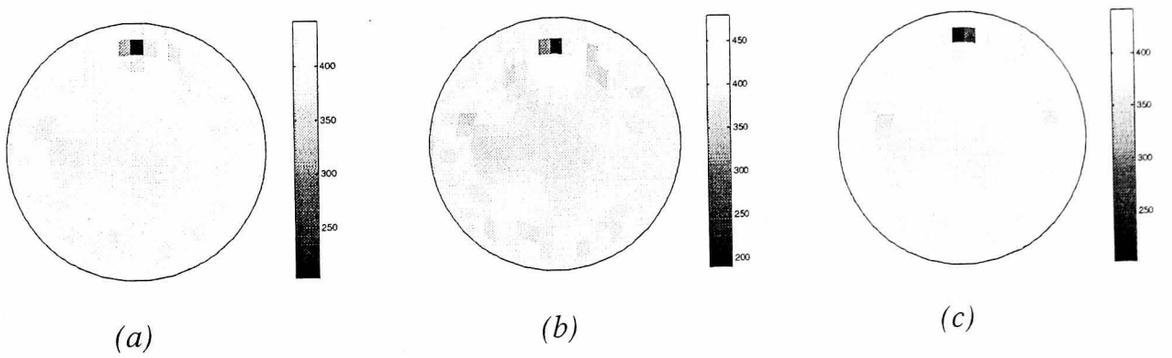

Figure 5.8: The imaging results of simulation object B, 0.1% noise.

(a) Result of the 1st mesh, regularization level=1e-3

(b) Result of the 2nd mesh, regularization level=1e-3

(c) Result of the 3rd mesh, regularization level=1e-3

Note: The image in Figure 5.8(b) with noise-added data looks better than Figure 5.7(b) with noise-free data. This is because of the different regularization level.

Figure 5.8 shows the 3 images which had been reconstructed. The image reconstruction errors for the 3 images are 0.0359, 0.0456, and 0.0356 respectively.

In summary, although the noise affected the imaging results and the change factors, in this case the change factor is still able to indicate which mesh(es) is(are) relatively compatible and which mesh(es) is(are) not.

5.5 Discussion and Conclusion

In this chapter a method has been proposed to select conductivity basis functions (coarse mesh) with compatible prior information, based on the principle that incompatible prior information will bring more noise to the image reconstruction and change its convergence behaviour.

The simulation study shows the effectiveness of this method. It is shown that the errors caused by incompatible prior information can be as high as several percents of the largest measurement made. The simulation has shown that this level of errors is enough to change the convergence behaviour of the Modified N-R algorithm. In the experiments in this study the proposed method has successfully pinpointed the coarse mesh most compatible to the object shape. Regarding information of the internal structure of the object, this method is successful in the sense that it has selected the coarse mesh best matched to the object structure near the periphery and produced the best image quality. The problem with the approach is that it does not treat the internal structure fairly and favours compatibility in the periphery over the centre. However, the method can still be useful, for example, in head imaging to select a best match for the structure of skull which is near the periphery. Furthermore, one can ease this imbalance of the influence of the incompatibility by making the peripheral elements smaller and the central elements larger in the coarse mesh. An example of such a mesh can be found in [Tang *et al* 1998], in which the size of the elements increases from boundary to centre. At the same time, several other factors affect the magnitude of the errors caused by the incompatibility of the internal structure. These

factors include the size and the conductivity contrast of the mismatched part.

It can be argued that the effect of the incompatibility with the internal object structure can be attenuated by applying a fine mesh as the basis functions for image reconstruction. This is true but it should be noted that an important point of applying prior information to EIT image reconstruction is to reduce the dimension of the problem and lead the result to the real solution. Applying a fine mesh greatly increases the dimension of the problem as well as the computation load.

There are 2 other factors which affect the performance of this proposed method. One is the relative ratio of the errors caused by incompatibility and the system noise. The other is the regularization level in image reconstruction. If the system noise is high, then the errors caused by the incompatibility will play a less important role in the convergence behaviour of the image reconstruction algorithm. It is important that regularization should be set at the right depth. Too little regularization results in huge conductivity changes and this could pose problems to the proposed method, while too much regularization results in the decrease of sensitivity of small incompatibilities.

The method reported requires several images to be reconstructed, which costs more time. In the example presented, it compares results of 3 meshes and takes twice more as long as that for a single mesh. However, the time required can be shortened. As shown in the four Tables, after the 2nd ~ 3rd step, some of the most incompatible meshes show significant changes in the conductivity. Therefore in this case, it is not necessary to continue reconstructing their images. Thus the time required can be significantly reduced.

Further studies are needed to investigate how to generate appropriate candidate sets of basis functions according to different part of the human body and different prior information available.

In principle this method can be applied to prior information other than boundary shape and internal structure. For example, several candidate configurations may be designed

concerning electrode positions. Then by applying this method it might be able to find the best configuration. This needs to be further studied.

This method could be well applied for breast imaging. One application is the 3D boundary shape of the breast, where a series of typical shapes can be designed. By applying the proposed method a compatible shape can be obtained. Another application is the said impedance gradient distribution in breast. A series of the gradient distribution can be designed and applied as a constraint in image reconstruction. This needs to be further investigated.

5.6 Summary

In this chapter a comprehensive investigation is reported regarding compatibility of different types of prior information and its effect on an iterative image reconstruction algorithm, based on which a novel method is proposed to improve EIT image quality. This method selects compatible prior information by observing the convergence behaviour of an image reconstruction algorithm. The principle, implementation, and results are detailed. Preliminary results indicate that the proposed method is effective, in the case when prior information is not accurate but can be presented in a number of variational forms, to improve image quality by choosing compatible prior information. Significant improvements in image quality can be achieved by applying this novel method.

CHAPTER 6 AN ELECTRICAL IMPEDANCE MAMMOGRAPHY SIMULATION SYSTEM AND PRELIMINARY RESULTS

In this chapter, an Electrical Impedance Mammography (EIM) simulation system has been developed. Simulation breasts under certain pathological conditions are designed and impedance images are reconstructed and analysed.

Section 6.1 is a general introduction. In Section 6.2 clinical *in vitro* tissue measurement and Cole-Cole model are described, based on which simulation 2D models of normal & abnormal breast are described in Section 6.3. Image reconstruction results of the simulation models of the breast are shown in Section 6.4. In Section 6.5, analysis on the Region Of Interest (ROI) of the reconstructed images is described, followed by a conclusion Section 6.6 and summary in Section 6.7.

6.1 Introduction

To facilitate research in EIT breast imaging, it is necessary to set up an imaging software system which is able to offer the basic functions such as collecting data, reconstructing different type of images (static, difference etc.), and analysing images and ROI. Furthermore, in order to investigate the feasibility of applying EIT in breast cancer detection, it is desirable to begin with conducting a simulation study on simulation breast models, which could offer some perspective and guidelines for further study of imaging real breasts.

In this study, an EIT simulation system for breast imaging has been developed. This system offers four main functions: 1) construction of different breast models based on age or racial group; 2) the development of boundary measurements according to the given

number of electrodes and their configuration; 3) image reconstruction with selected algorithm from different algorithms and image visualization; 4) Cole-Cole parameter fitting for the ROI in the reconstructed images.

This system can provide comprehensive simulation of different aspects of actual Electrical Impedance Mammography (EIM) images from the hardware system performance to image analysis. Furthermore, this system is able to help evaluate image reconstruction techniques.

To construct a simulation breast model, knowledge of the electrical impedance properties of different types of breast tissue is required. This knowledge can be obtained through *in vitro* tissue impedance measurement and modelling, which is described firstly in the following section 6.2 before introducing the simulation system in the subsequent sections.

6.2 Clinical *in vitro* measurement and Cole-Cole model

6.2.1 Clinical *in vitro* measurement

Clinical *in vitro* measurements of breast tissue were conducted in Glenfield General Hospital in Leicester. Impedance spectra of different breast tissue were collected by an HP4194A impedance analyser within 3 hours after the tissue was excised from patients undergoing breast surgery. A small cylindrical tube was connected to the HP4194A to carry out the standard 4-electrodes impedance measurements, as shown in the following Figure 6.1. The specimen being measured was cut and put to the said cylindrical tube. The size of these specimens was 8mm in diameter and 5mm in length. In order to keep good contact between the tissue and all the 4 electrodes, saline was used to fill all the space left in the tube. Data were collected on 16 frequency points ranging from 1 Hz to 5 MHz.

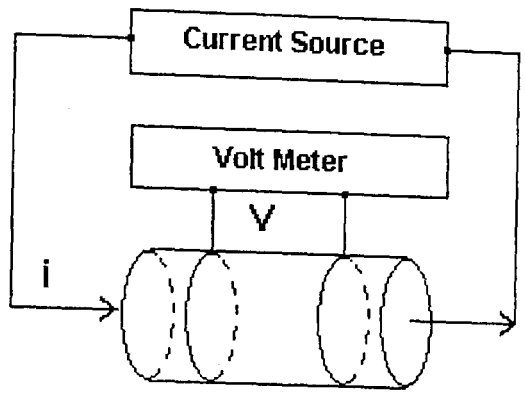

Figure 6.1: Diagram for in vitro impedance measurement

Because the impedance measurement is sensitive to temperature changes, the temperature of the tissue was strictly controlled at 37 C° during the measurement by keeping the tube in water bath.

In this study, 17 patients with age of 57.81 ± 13.19 (mean ± SD) were selected and a total of 32 impedivity spectra were collected. These include 11 fat tissues, 12 tumour tissues (stage 2 and stage 3 Infiltrate ductal carcinoma (IDC)), and 9 pure stroma tissues. As a result, a total of 32 impedance spectra were obtained.

6.2.2 Cole-Cole model

Modelling the tissue impedance measurements and extracting meaningful parameters are essential for characterising and analysing the electrical properties of tissue.

Different tissue has different electrical properties. For a fixed current frequency, this property appears as the impedance of the tissue. When the current frequency changes, the impedance also changes, which can be well modelled by a generally-accepted Cole-Cole equation [Cole K S 1940][Cole K S 1941] as follows:

$$Z = R_\infty + (R_0 - R_\infty) / (1 + (jf/Fr))^{(1-\alpha)} \qquad (6.1)$$

Here R_∞ is the resistance of the tissue when frequency moves to infinite, R_0 is the resistance of the tissue when frequency is zero. Fr is the dispersion frequency of the tissue. α is the so-called relaxation factor.

Usually this equation is written as the following, corresponding to the three-element electrical equivalent circuit (Figure 6.2) for tissue:

$$Z=R\cdot S/(R+S) + (R - R\cdot S/(R+S)) / (1 + (jf/Fr))(1-\alpha) \qquad (6.2)$$

Where R equals to R_0, the parallel of R and S equals to R_∞

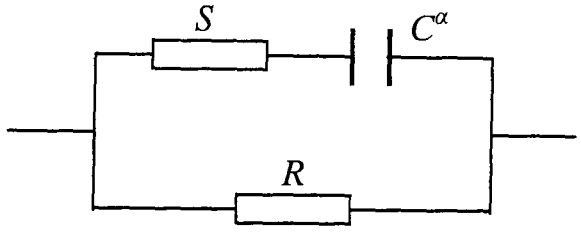

Figure 6.2: A three-element Cole-Cole model

To make the parameters independent of the dimensions of tissue, the resistance R_0&R_∞ or R&S should be normalised by the size of the tissue and become resistivity. Besides, EIT images show the resistivity (or impedivity) distribution as well. Therefore, in the following study the resistivity is used as the unit for parameter R and S except for otherwise stated.

All the 32 impedance spectra of breast tissues obtained from *in vitro* measurements were then fitted to Cole-Cole model by a Powell method (For more description of the algorithm

please see [Lu *et al* 1995]). As a result, 32 sets of Cole-Cole parameters were obtained. The statistic figures of the 32 sets of parameters are shown in Table 6.1.

Table 6. 1 Cole-Cole parameters from in vitro measurement (mean ± SD)

	R (Ωm)		*S(Ωm)*		*Fr(Hz)*		*α*	
	Mean	Std	Mean	Std	Mean	Std	Mean	Std
Fat	15.074	6.1157	0.3794	0.1439	1.4785e6	4.0721e5	0.0923	0.0216
Stroma	1.6371	0.6061	2.9562	1.2630	2.1170e6	8.0545e5	0.1583	0.0487
Carcinoma	2.0159	0.7402	0.0060	0.0029	1.1296e6	4.3731e5	0.3996	0.1548

6.3 Simulation breast model

6.3.1 Construction of breast models with the generated Cole-Cole parameters.

The system has functionality for setting up any Cole-Cole parameter distribution within a two-dimensional (2D) circular boundary to simulate the electrical property distribution within the human breast, under normal and pathological conditions. The distribution is age dependent in that the breast tissue distribution itself varies depending upon the relative prevalence of adipose and stromal tissues. To simplify the complicated anatomical cases two breast models were developed to reflect both younger and older, post-menopausal, women.

For the young group, generally accepted as < 50yrs, the ratio of fatty tissue against stroma decreases from 90% near the boundary to 10% in the middle of the breast, as shown in Figure 6.3(a)(b). The plane of measurement is at an assumed level half way from chest wall to nipple. For the senior group, generally accepted as >50yrs, stromal tissues are replaced with adipose tissue and breasts in this group consist of much more fatty tissue at

the periphery than the younger group, as shown in Figure 6.3(c)(d). Based on these two models, abnormalities were added at two positions in both groups as shown in Figure 6.3. The diameter of the model is 10cm, a reasonable diameter if gentle centralized compression is applied. In this 2 dimensional simulation, the size of the abnormality is approximately $1cm^2$. Figure 6.3 has the grey scales artificially adjusted for enhanced visualization.

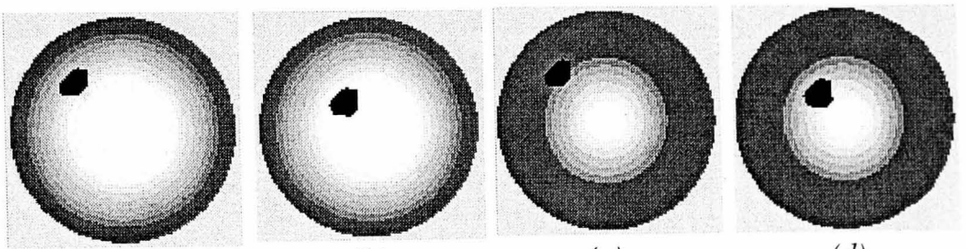

(a) (b) (c) (d)

Figure 6. 3 Breast models

(a) Young group with Carcinoma (IDC II) in position1;

(b) Young group with Carcinoma (IDC II) in position2;

(c) Senior group with Carcinoma (IDC II) in position1;

(d) Senior group with Carcinoma (IDC II) in position2;

6.3.2 Development of boundary voltages using FEM method

The boundary measurements can be generated by FEM method with multi-frequency current injection.

The first step is the selection of a number of frequencies from which impedance measurements can be obtained. The selection used for the presented example of the system is: 1kHz, 2kHz, 5kHz, 10kHz, 20kHz, 50kHz, 100kHz, 200kHz, 500kHz, 1MHz, 2MHz, 3MHz.

The next step is the development of the boundary voltages from impedance distribution

corresponding to each frequency. This is done by a forward problem solver which uses FEM, given the settings of the electrodes and currents. In this study 32 electrodes (16 drivers and 16 receivers) with interlaced adjacent configuration were used for the simulation. Currents are injected through 2 adjacent driver electrodes and voltages are measured on 2 adjacent receiver electrodes. The current injection and voltage detection scheme used is, however, fully user selectable. To simulate the practical situation, different levels of random noise can be added. In the subsequent examples normally distributed noise is used with amplitudes of 1% and 5% of the minimum values of the boundary measurement. This is to represent the potential noise levels of the De Montfort Mk2B EIM system [Wang *et al* 1998].

6.4 Image reconstruction results

Both the real and imaginary part of the differential impedance distribution can be reconstructed with three different algorithms which had been introduced previously in Chapter 3: Newton-Raphson (N-R) based algorithm, Equi-Potential Back-Projection algorithm, and General Inverse algorithm. For the N-R algorithm, static images can be produced. The other two algorithms produce difference images with respect to a reference data set. For difference images, the first frequency data set is used by default as the reference data set. The results of the following study are those of N-R algorithm.

6.4.1 Static imaging results

In Figure 6.4, two different frequency images are represented for two different age groups and two different abnormality positions with same order in each raw as shown in Figure 6.3. Note that all the images here are conductivity images.

It can be seen that the static images show better separation from the carcinoma in

periphery area (Figure 6.4(a)(c)) than in central area (Figure 6.4(b)(d)) in both age groups. The reason is twofold. One is that impedivity/conductivity between carcinoma and boundary tissue (mainly fatty tissue) is much more different than that of carcinoma and tissue near central region (mainly stroma tissue). The other is that central image quality is generally poorer than in the periphery area due to the ill-posedness of the image reconstruction. In addition, it appears that better separation is achieved in the higher frequency range in all cases.

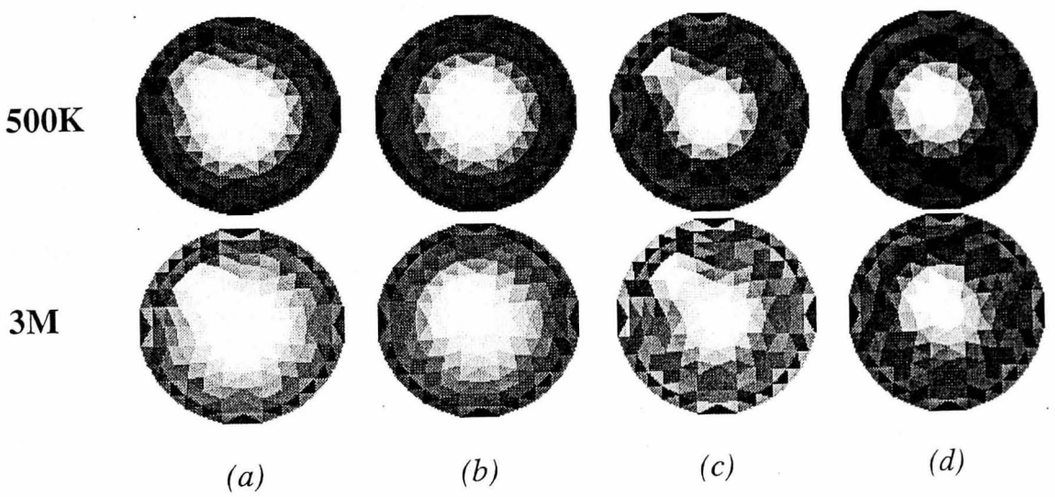

Figure 6.4 Noise-free static images for the four groups
(a) Younger women, position 1; (b) Younger women, position 2
(c) Senior women, position 1; (d) Senior women, position 2

It can be summarized that the static imaging has produced good differentiation of carcinoma from normal surrounding tissue when carcinoma is located near the periphery for all group. However, it is fairly difficult to separate the carcinoma from the stroma in central region which has the high incidence.

6.4.2 Difference imaging results

The images shown in Figure 6.5 are called "difference images" (DI) which show the difference of impedance distribution between two frequencies.

From the results shown in Figure 6.5, the DI method can be seen to provide much better separation of the carcinoma from the surrounding normal tissue in all cases. It can be seen that the "difference" images can produce high sensitivities in detection of carcinoma for both young group and senior group.

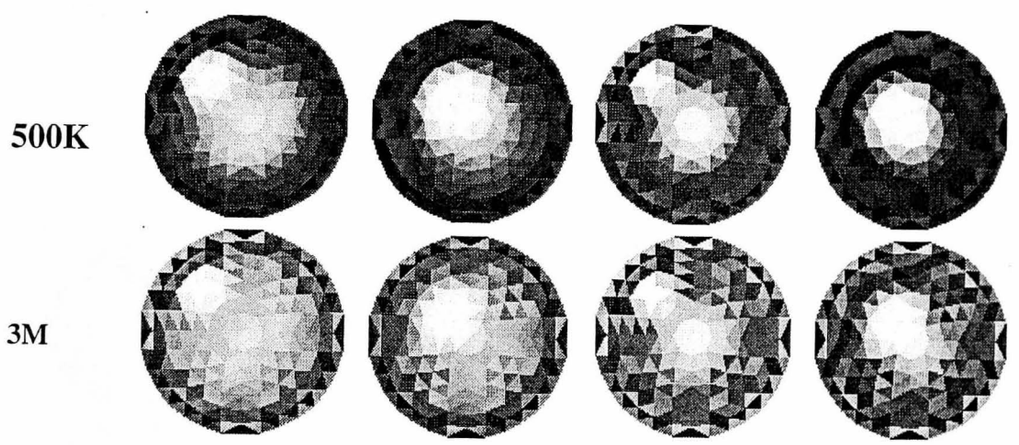

Figure 6.5 Noise-free "difference" images (Difference from 1kHz image)
(a) Younger women, position 1; (b) Younger women, position 2
(c) Senior women, position 1; (d) Senior women, position 2

In order to simulate practical cases of noise contamination in the data, three different levels of noise have been added to the data. Image reconstruction results are shown in Figure 6.6 and Figure 6.7 with noise levels of 0 %, 1% and 5% of the smallest measurement. It can be seen from Figure 6.6(b), (e) and 6.6(c), (f) that noise levels can affect detection/imaging carcinoma in low frequency bandwidth due to the less difference

in impedivity/conductivity below 500KHz.

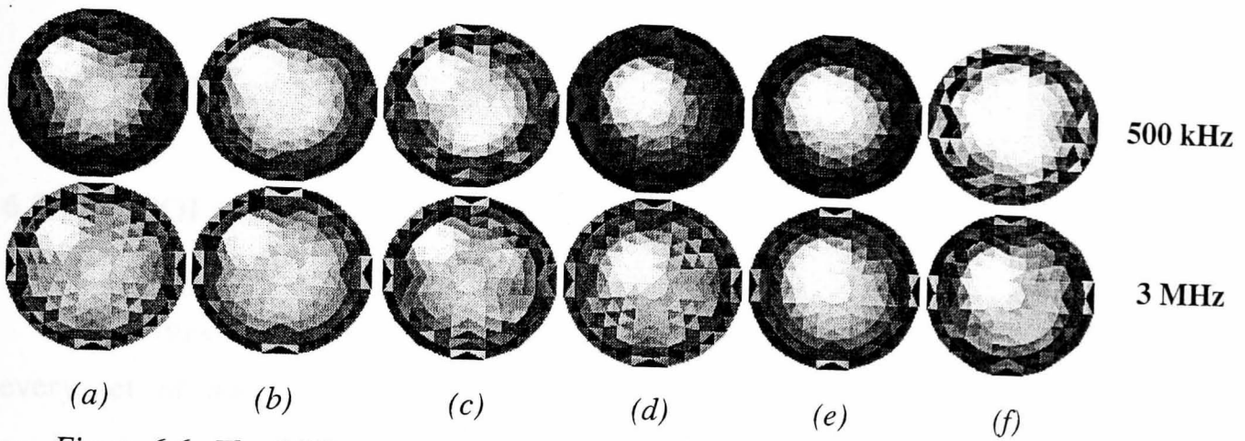

Figure 6.6 The "difference" image with varying noise levels (young group)
(a) 0% ; (b) 1% and (c) 5% with an IDC in position1
(d) 0% ; (e) 1% and (f) 5% with an IDC in position2

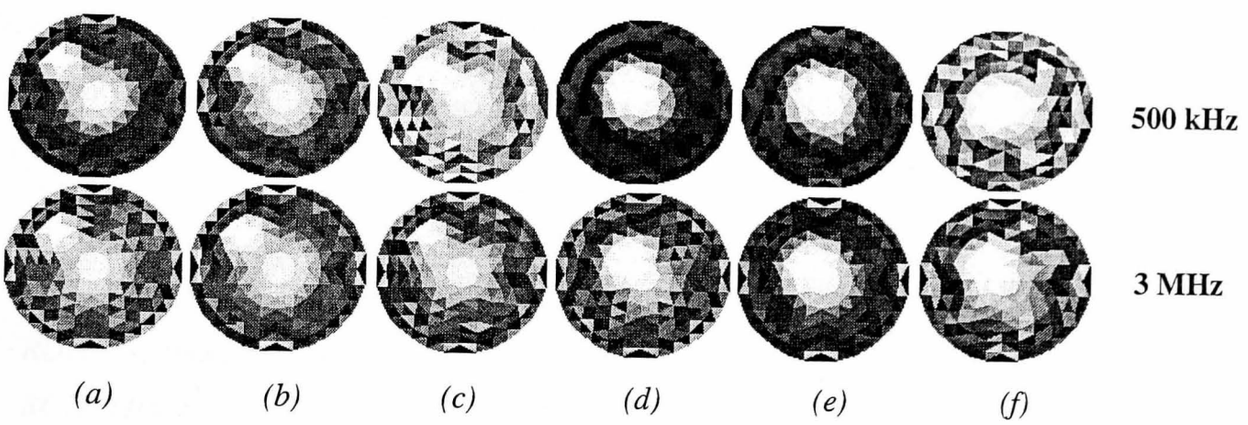

Figure 6.7 The "difference" image with varying noise levels (senior group)
(a) 0% ; (b) 1% and (c) 5% with an IDC in position1
(d) 0% ; (e) 1% and (f) 5% with an IDC in position2

In summary, the difference image can provide much better detectability in EIM system. This is because higher frequencies will provide better differentiation in between normal and abnormal tissue due to the large impedivity/conductivity changes in higher frequency

bandwidth. A noise level of 5% of the minimum measurement is an acceptable level, provided that adjacent current injection and measurement are used.

6.5 ROI analysis

6.5.1 ROI setting

Static images of N-R algorithm were used to calculate the Cole-Cole parameters. For every set of data, 12 static images, corresponding to the selected frequencies, were produced. In each of these images, several Regions of Interest (ROI) were chosen from among the 6 arbitrary ROIs given in Figure 6.8.

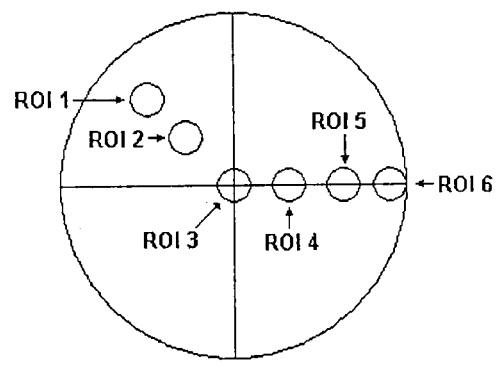

Figure 6.8 Selected Regions of Interest

ROI1: 1st abnormality (IDC); ROI2: 2nd abnormality (IDC); ROI3: Stroma;

ROI4: Mixed tissue (mix-1) at same distance from centre as ROI2;

ROI5: Mixed tissue (mix-2) at same distance from centre as ROI1; ROI6: Fat.

As shown in Figure 6.8, these 6 ROIs correspond to the positions of different tissue type. ROI 1 and 2 correspond to the two abnormalities (tumour), ROI 3 corresponds to stroma, ROI 4 and 5 correspond to the tissue mixture at the same distance from the centre as ROI 2 and ROI 1 respectively, and ROI 6 corresponds to fat.

For this ROI setting, comparing ROI 1, 3, 5, and 6 shows the difference between stroma, fat, tumour near the periphery, and the tissue mixture which is near the periphery as well. Similarly, comparing ROI 2, 3, 4, and 6 shows the difference between stroma, fat, tumour near the centre, and the tissue mixture which is near the centre as well.

For each of the ROIs, an impedance spectrum can be obtained from the static images of 12 frequencies. These spectra can be analysed for the purpose of identifying tissue within the ROI. Details of this analysis is shown in the following sections.

6.5.2 ROI analysis results

The ROI impedance spectrum of two groups with two different tumours positions have been shown in Figure 6.9(a)-(d) respectively. It should be noted that the ROI results shown in Figure 6.9 are resistivity, which is measured from the static images. Static images have to be used to extract all 4 Cole-Cole parameters of ROI.

From the results shown in Figure 6.9, it can be seen that:

1) Comparing the ROI curves between two IDC positions in both groups, cancer in Position1 (ROI 1 in Figure 6.9 (a)(c)) can be easily detected than in Position2 (ROI 2 in Figure 6.9 (b)(d)) in low frequency bandwidth; i.e. the tumour in periphery area can be easily detected than in central areas of the image plane;

2) Comparing the ROI curves in two different age groups, it seems that the cancer can be easier differentiated from senior group in low frequency bandwidth than young group in all cases;

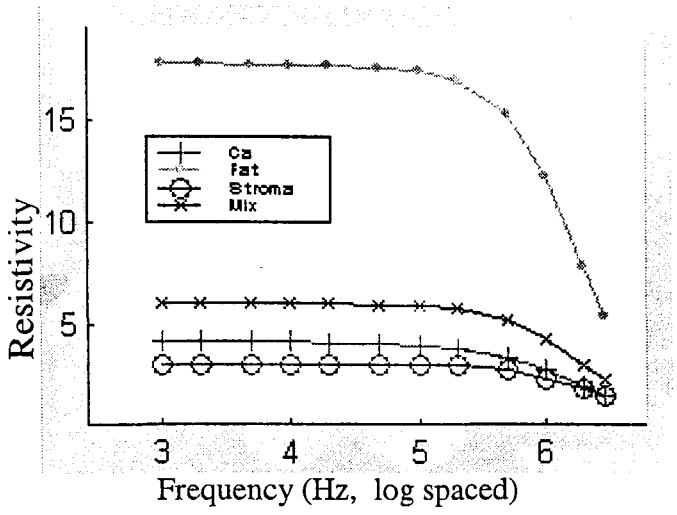

(a)

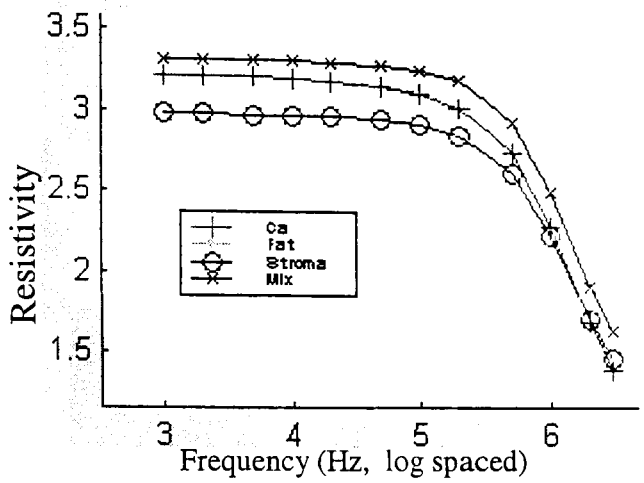

(b)

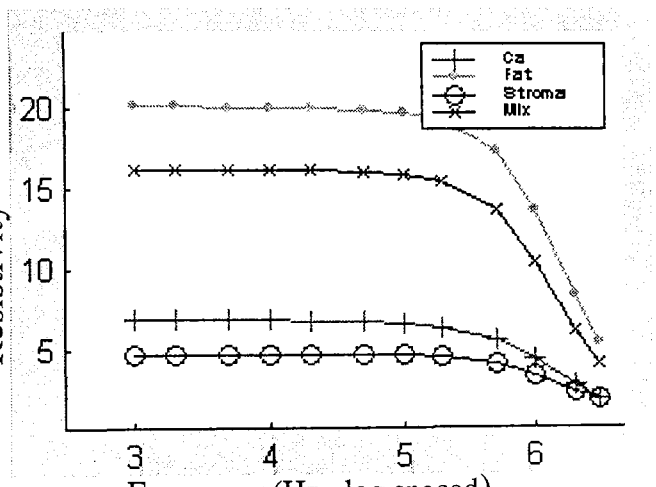

(c)

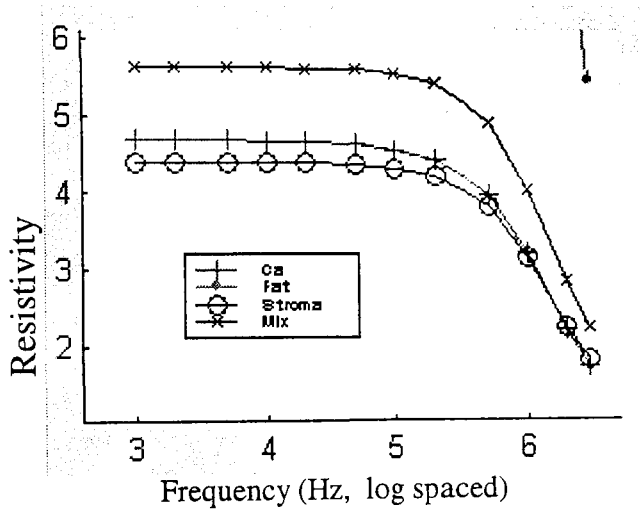

(d)

Figure 6.9 ROI impedance spectrum with noise free model

(a) Young group: Cancer in position1; other ROI with same positions;

(b) Young group: Cancer in position2; other ROI with same positions(no fat);

(c) Senior group: Cancer in position1; other ROI with same positions;

(d) Senior group: Cancer in position2; other ROI with same positions(no fat).

(Note: in the Figure 6.9(b)(d), the curve of ROI with fat were omitted due to its much higher resistivity. It is omitted in order to show the difference among other ROI curves.)

Each ROI curve can then be fit into the Cole-Cole model to extract the parameters of intro- and extra cellular information for ROI analysis. All the parameters of different ROI were generated and are shown in Figure 6.10.

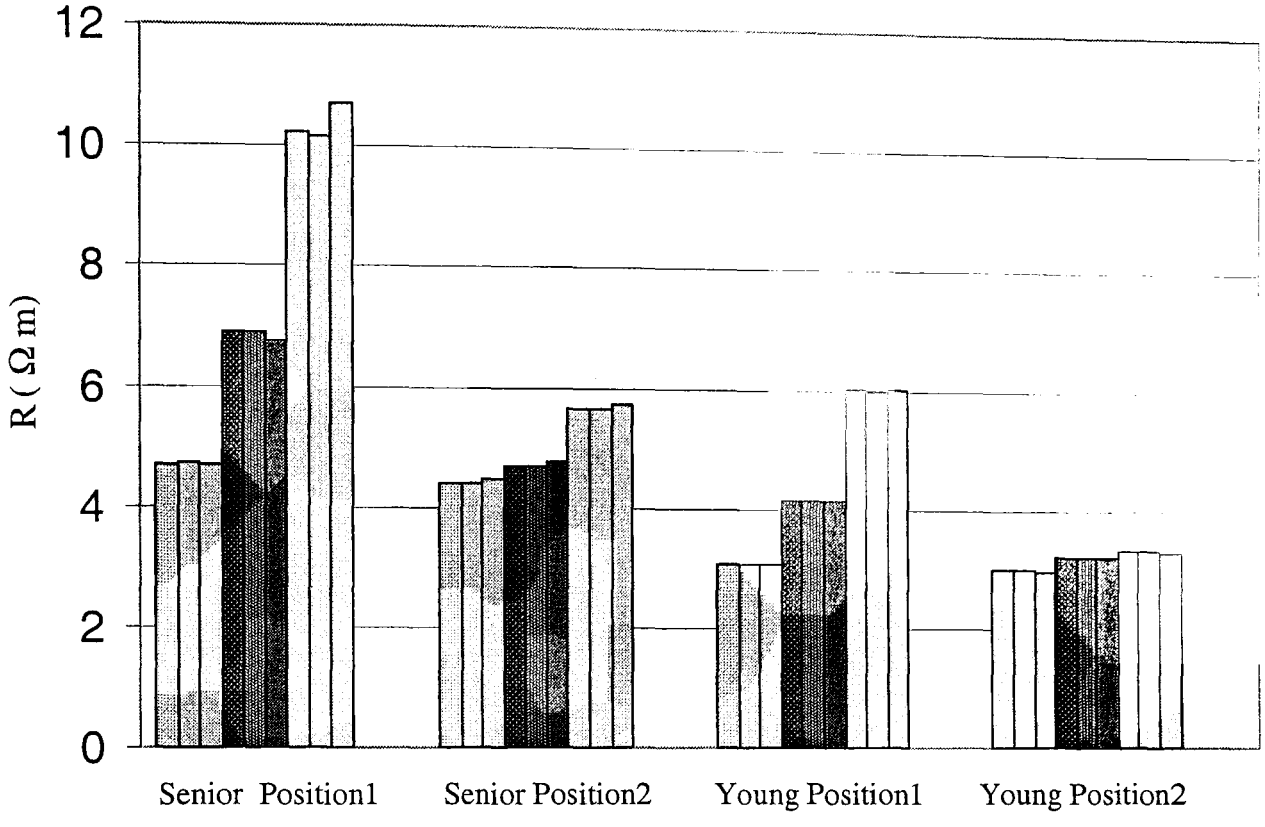

(a) Parameter R

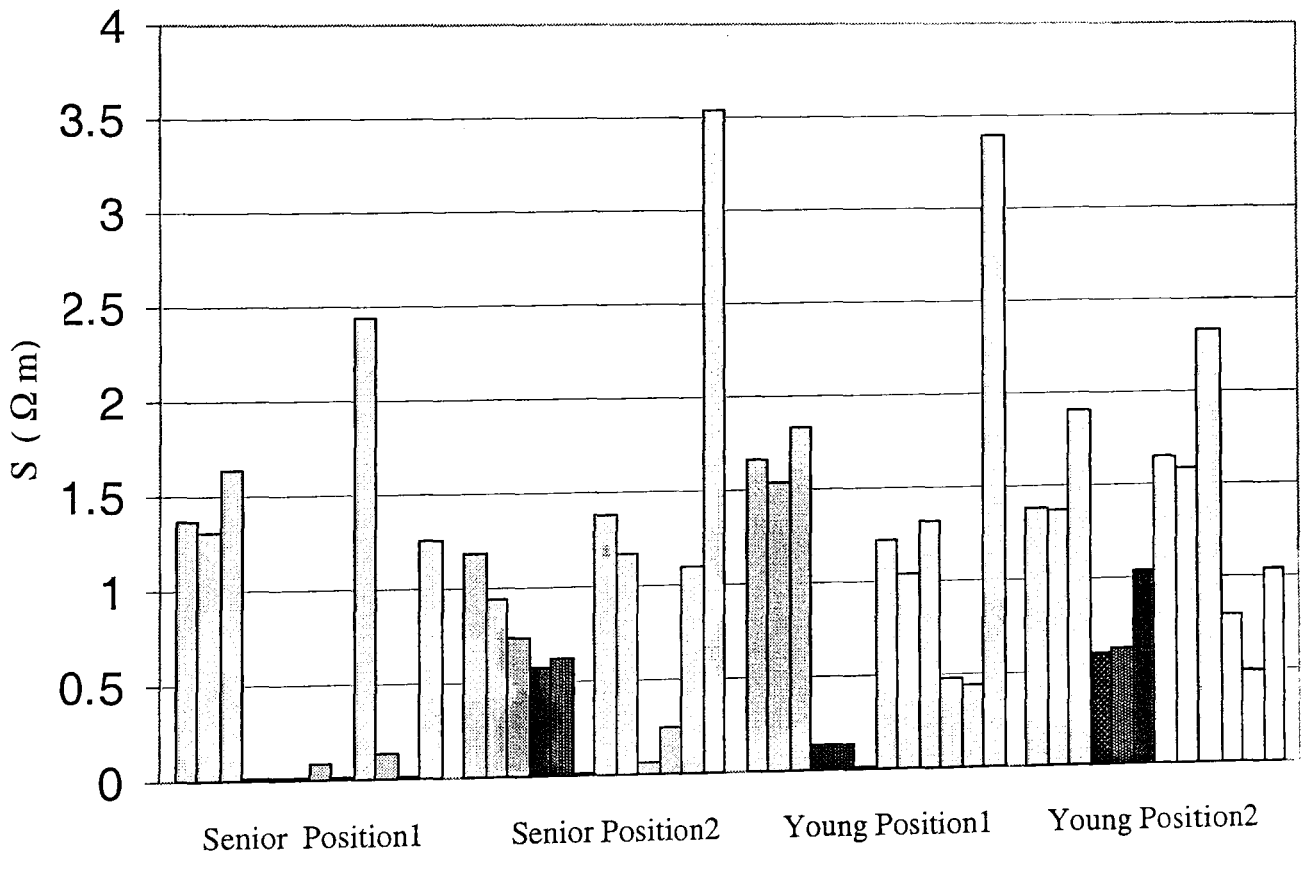

(b) Parameter S

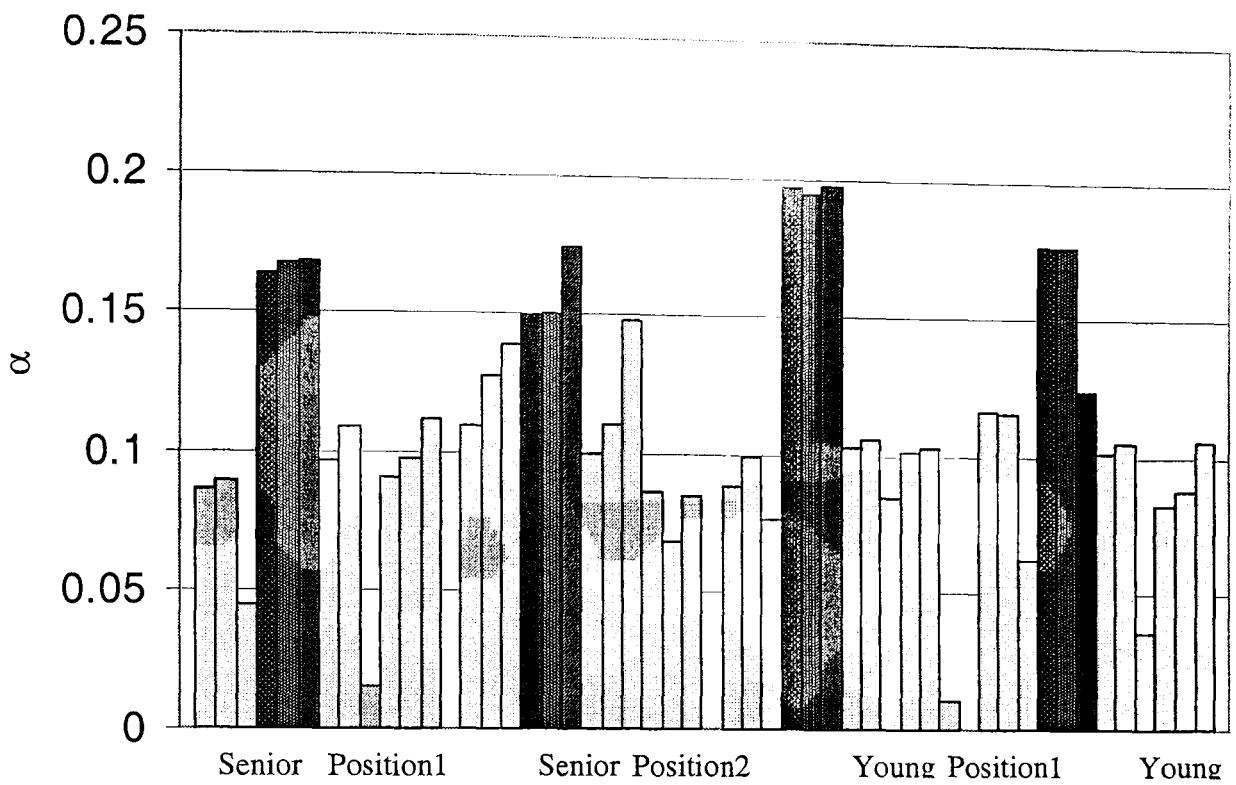

(c) *Parameter α*

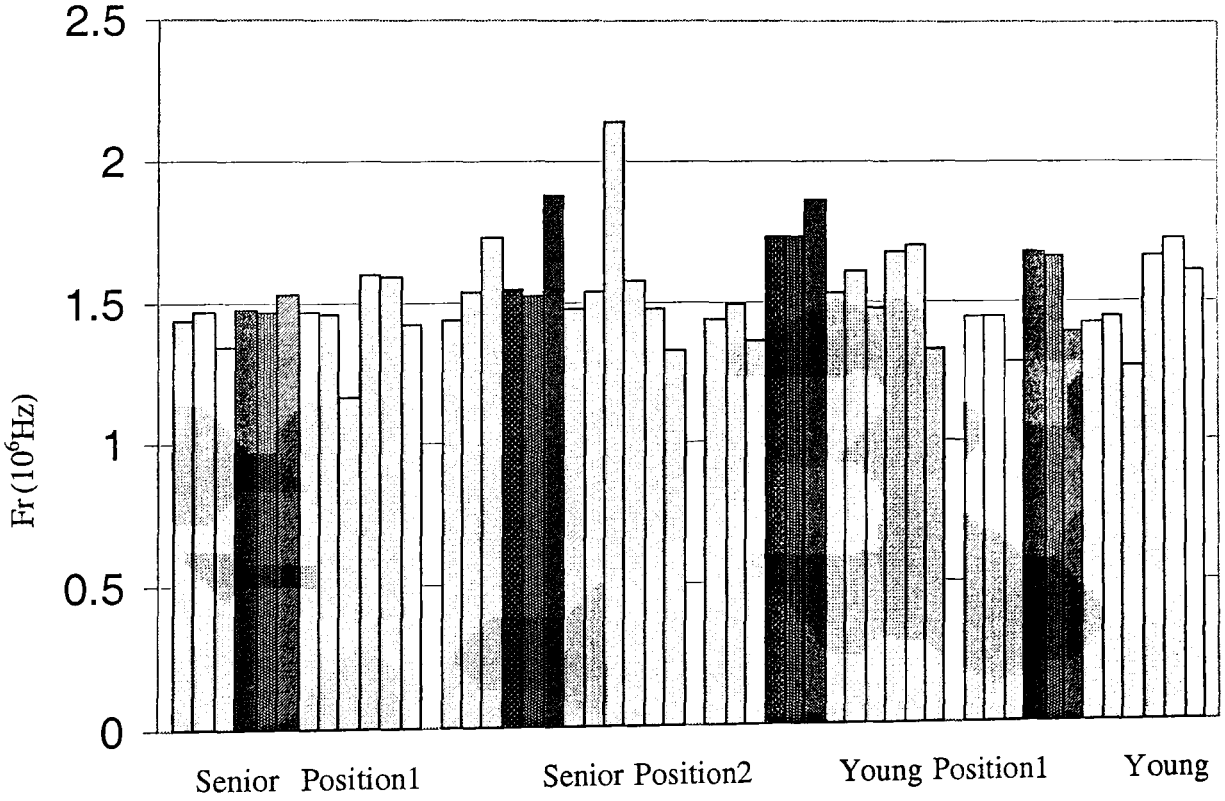

(d) Parameter Fr

Figure 6.10 The parameters of ROI (parameters of ROI with cancer are shown in dark color) (a) Parameter R; (b) Parameter S; (c) Parameter α; (d) Parameter Fr.

Every figure has 4 groups of bars in sequence: 1) Senior model, abnormal position 1; 2) Senior model, abnormal position2; 3)Young model, abnormal position 1; 4)Young model, abnormal position2.

Each Group has 12 bars in sequence, from left to right: 1)Stroma noise-free, 2)stroma 1% noise, 3)stroma 5% noise, 4)cancer noise-free, 5)cancer 1% noise; 6) cancer 5% noise; 7)mixture noise-free, 8) mixture 1% noise; 9) mixture 5%noise; 10)fat noise-free; 11) fat 1% noise; 12)fat 5% noise

(Note: in the Figure 6.10(a), in order to show the difference among other ROI parameters, the parameters of ROI with fat were omitted due to their high values.)

From the results from Figure 6.10, the following points can be discussed:

1) Parameter R of ROI with cancer is bigger than stroma and smaller than mixture tissue around it in all cases, which suggests this parameter as a possibly good indicator for tissue identification;

2) Parameter S of ROI with cancer is the smallest in all cases. However, 5% noise can cause great errors in S.

3) The α of ROI with cancer is the biggest in all cases, which suggest this parameter as a possibly good indicator for cancer identification;

4) No significant difference between ROI with cancer and other tissue in Fr can be observed.

5) 5% noise caused much smaller errors in parameter R than S, a, and Fr.

In this study, all the parameters derived from ROI cannot correspond to the original

value in Table 6.1, this is partly because the mixture feature of every ROI. Every ROI contains more than a single type of tissue. So actually all the Cole-Cole parameters will be affected and presented as an 'average value' of several different kinds of tissue. Another reason is the image reconstruction errors, especially near the central area of the image.

6.6 Conclusions

It has been shown that the simulation imaging system offers a wide range of capabilities. The system is able to give a good estimation of the capabilities that can be expected in real imaging. It is able to provide a number of quality estimators to indicate the necessary bandwidth and noise levels that can be accepted by the image reconstruction algorithms.

Results from simulation show that static imaging cannot provide good visual differentiation between tumour and stroma based on the parameters given in Table 6.1. However it has been shown that the use of "difference imaging" can provide a good visual differentiation between the tissue types, and this method appears robust to noise, as visual differentiation is still possible at 5% noise levels.

The initial results of static and difference images have demonstrated that it is possible to identify the breast cancer in both senior group and young women group (Figure 6.4 ~ Figure 6.7). The use of the ROI facility permits the system to extract useful parameters from the images. These parameters can be used for the purpose of identifying specific breast abnormalities in an early stage. This study indicates the potential of parameters R, α, and S for cancer detection.

More clinical *in vitro* and *in vivo* measurements are needed. Hopefully with these studies, more valuable information can be obtained for the differentiation of carcinomas from the normal background and benign diseases in the near future.

Some systematic errors have been identified in ROI information in this study due to the mixture feature of every ROI, the mismatch between imaging objects and reconstruction mesh, and image reconstruction errors.

6.7 Summary

In this chapter a computer simulation system for breast impedance imaging and analysis system is described. To demonstrate the functionalities of this system several breast models with different physiological and pathological conditions were made based on clinical *in vitro* measurements. Images with different current frequencies were reconstructed and the Region Of Interests were analysed. Preliminary results indicate that EIM has the potential for detection of breast carcinoma.

CHAPTER 7 THREE DIMENSIONAL ELECTRICAL IMPEDANCE TOMOGRAPHY AND ELECTRODE PLACEMENT

In this chapter three-dimensional EIT is studied. The principles and implementation are described followed by a simulation study comparing two types of electrode placement for breast imaging.

Section 7.1 gives a brief introduction. Section 7.2 details the three-dimensional finite element method for solving the forward problem. In Section 7.3 a three-dimensional image reconstruction algorithm is introduced. Section 7.4 describes the analysis of the sensitivity distribution in a cylindrical object with 2 different types of electrode placement. 3D images of simulation objects are shown. Section 7.5 is a brief summary.

7.1 Introduction

2D EIT assumes that all the current is confined in the 2D plane, while actually the current flows in a 3D manner. This introduces errors into the image reconstruction. At the same time, two dimensional electrode placement limits the number of electrodes which can be used and therefore limits the information in the measurements. In contrast, three-dimensional EIT not only avoids the errors caused by the assumptions, but also enables the use of more electrodes with more flexible placement and may contribute more independent information.

Although studies in three-dimensional EIT started in 1990 [Goble *et al* 1990] and more and more groups are involved in this area, unlike 2D EIT for which there is already a free imaging software package EIDORS2D [Vauhkonen *et al* 2001], no such software package

is available. To catch up in this area, the Medical Imaging group saw the provision of dedicated three-dimensional EIT imaging system software as highly desirable.

In the following study, firstly the principle and implementation of 3D FEM for solving the forward problem are briefly introduced, and then a 3D version of the modified N_R algorithm follows. Based on the 3D FEM forward solver, a sensitivity analysis of a cylinder is conducted with 2 types of electrode placement which are currently used for breast imaging. Images are reconstructed with both electrode placements and the results of the sensitivity analysis are compared. This was done to facilitate the choice of an optical driving & measuring strategy for breast imaging.

7.2 Three dimensional FEM forward solver

The forward problem solver is an integrated part of EIT image reconstruction. The following section describes the principles and implementation of the 3D FEM forward solver.

7.2.1 Principles

The three dimensional electric field is governed by the same equation as mentioned in Chapter 3:

$$\nabla \cdot \sigma \nabla u = 0 \tag{7.1}$$

with boundary conditions

$$u = \bar{u} \qquad \text{voltage distribution on } \partial A \tag{7.2}$$

$$\sigma \frac{\partial u}{\partial n} = J \qquad \text{current density on } \partial A \tag{7.3}$$

Here σ is the conductivity distribution within whole volume Ω, u is the voltage distribution, and J is the current density. ∂A is the boundary of the region.

In the FEM method, the variational form of equation (7.1) can be written as:

$$B(u, v) = f(v) \tag{7.4}$$

Where $u,v \in H^1(\Omega)$, $H^1(\Omega)$ is the associated Sobolev space. In the previous equation:

$$B(u, v) = \iiint_{\Omega} \sigma \nabla u \cdot \nabla v \; dxdydz \tag{7.5}$$

$$f(v) = \int_{\partial A} J \; v \; ds \tag{7.6}$$

FEM is used to turn the continuous problem given above into a discrete formulation. Firstly, the solution domain Ω is discretised into small elements and thereby a mesh is obtained. A typical mesh can be found in Chapter 2.

The potential distribution u within the object is approximated with the finite sum:

$$u(x, y, z) = \sum_{i=1}^{N} u_i \Psi_i(x, y, z) \tag{7.7}$$

where the functions ψ form a basis for the finite dimensional subspace H' of $H^1(\Omega)$, N is the dimension of the finite subspace H' and u_i is the discretised potential distribution. Here if the domain is discretised into N tetrahedrons, then u_i is the potential on every node of the tetrahedrons. The FEM basis function $\psi_i(x,y,z)$ equals zero in the most of the domain and only has non-zero values in the tetrahedrons connected to node i.

The same is true for the function v

$$v(x,y,z) = \sum_{j=1}^{N} v_j \Psi_j(x,y,z) \tag{7.8}$$

By inserting these 2 approximation functions into the variational equation, given that $B(u,v)$ and $f(v)$ are both linear, the following expression can be obtained:

$$\sum_{i=1}^{N} v_i [\sum_{j=1}^{N} u_i \; B(\Psi_i, \Psi_j) \; - \; f(\Psi_i) \;] = 0 \tag{7.9}$$

Because v_i can be chosen arbitrarily,

$$\sum_{j=1}^{N} u_i \; B(\Psi_i, \Psi_j) \; = \; f(\Psi_i) \tag{7.10}$$

Therefore, a system of equations is obtained that can be written in matrix form as

$$K\,U = I \tag{7.11}$$

where

$$\begin{aligned} K\,(i,j) &= B(\Psi_i, \Psi_j) \\ U &= u_i \;\; I=1\sim N \\ I \;\; &= f(\Psi_i) \end{aligned} \tag{7.12}$$

The next step is to calculate the matrix K and I.

7.2.2 For the matrix *K*

Matrix *K* is defined as:

$$K(i,j) = B(\Psi_i, \Psi_j) = \iiint_{\Omega} \sigma \quad \nabla\Psi_i \cdot \nabla\Psi_j \; dxdydz \qquad (7.13)$$

For the basis functions Ψ_i, it only has none-zero values within the mesh elements which are connected to node *i*. Therefore, *K(i,j)* can only have none-zero value in those elements which are connected to both node *i* and node *j*. Therefore when calculating *K(I,j)*, it is only necessary to integrate over the relative elements.

In order to easily implement this integration in computer terms the calculation proceeds element by element. In the three dimensional case, for every element which has 4 nodes *i,j,k,l* (if I<j<k<l), a 4 by 4 matrix can be calculated which is:

$$\begin{matrix} K(i,i) & K(i,j) & K(i,k) & K(i,l) \\ K(j,i) & K(j,j) & K(j,k) & K(j,l) \\ K(k,i) & K(k,j) & K(k,k) & K(k,l) \\ K(l,i) & K(l,j) & K(l,k) & K(l,l) \end{matrix} \qquad (7.14)$$

The 4 by 4 sub-matrix formed is inserted into the overall matrix, *K*, the location in the matrix being determined by the coordinates *i, j, k*, and *l*.

Changing the coordinate in the integration

The integration of each element is different, as both the shape and the position of the elements are different. In order to proceed easily, a common way is to change the coordinates, so that the integration can be calculated using a standard element. The standard

element is shown in Figure 7.1 and the resulting unified approach is formulated in equation 7.15.

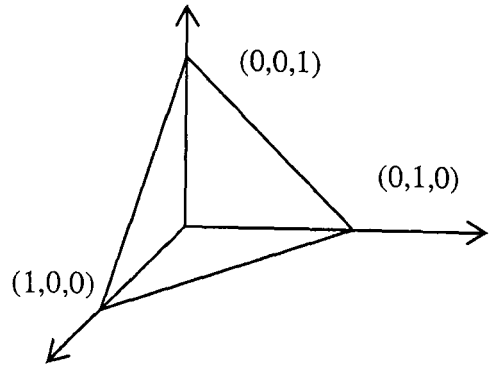

Figure 7.1 Standard element

After the change of the coordinate, for one element Ω_e, equation (7.13) can be rewritten as

$$K(i,j) = B(\Psi_i, \Psi_j) = \iiint_{\Omega_1} \sigma_e \nabla\Psi_i \cdot \nabla\Psi_j \left|J\right| d\lambda_1 d\lambda_2 d\lambda_3 \quad (7.15)$$

The integration of every element can be calculated in this standard element Ω_1. The next question is how to calculate $\nabla\Psi_i$ and $\nabla\Psi_j$.

For $\nabla\Psi_i$,

$$\nabla\Psi_i = \frac{\partial\Psi_i}{\partial x} + \frac{\partial\Psi_i}{\partial y} + \frac{\partial\Psi_i}{\partial z} \quad (7.16)$$

For the tetrahedral element with 4 nodes as *i,j,k,l,* the linear polynomial of the basis function Ψ on node *i* can be written as:

$$\Psi_i(x,y,z)=\frac{1}{|J|}(E-Ax+By-Cz) \tag{7.17}$$

$$J=\begin{vmatrix}1 & x_i & y_i & z_i\\ 1 & x_j & y_j & z_j\\ 1 & x_k & y_k & z_k\\ 1 & x_l & y_l & z_l\end{vmatrix} \tag{7.18}$$

And

$$A=\begin{vmatrix}1 & y_j & z_j\\ 1 & y_k & z_k\\ 1 & y_l & z_l\end{vmatrix} \qquad B=\begin{vmatrix}1 & x_j & z_j\\ 1 & x_k & z_k\\ 1 & x_l & z_l\end{vmatrix} \qquad C=\begin{vmatrix}1 & x_j & y_j\\ 1 & x_k & y_k\\ 1 & x_l & y_l\end{vmatrix} \tag{7.19}$$

Therefore,

$$\frac{\partial\Psi_i}{\partial x}=-\frac{A}{|J|} \quad \frac{\partial\Psi_i}{\partial y}=\frac{B}{|J|} \quad \frac{\partial\Psi_i}{\partial z}=-\frac{C}{|J|} \tag{7.20}$$

The same calculation applies to $\frac{\partial\Psi_j}{\partial x}$.

As can be seen, in our case, $\nabla\Psi_i$ and $\nabla\Psi_j$ are not functions of either (x,y,z) or $(\lambda_1,\lambda_2,\lambda_3)$, therefore, they can be moved outside the integration together with $|J|$ and σ_e. Actually there is nothing left in the integration and consequently equation 7.15 can be written as:

$$K(i,j)=B(\Psi_i,\Psi_j)=\frac{1}{6}\sigma_e\,\nabla\Psi_i\cdot\nabla\Psi_j\,|J| \tag{7.21}$$

$$\iiint_{\Omega_l} d\lambda_1 d\lambda_2 d\lambda_3 = \frac{1}{6}$$

where Ω_l is the standard element, which is shown in Figure 7.1.

If much higher precision is needed, non-linear basis functions can be used. However this not only increases precision but computing loads.

7.2.3 For the matrix I

The matrix I can be calculated as follows:

$$I = f(\Psi_i) = \int_{\partial A} J \Psi_i \, ds \tag{7.22}$$

To simplify the problem here the electrode is simply considered as a point. Consequently current is injected through a point(s) into the volume and the potential is measured on these points. The position of these points is considered as the boundary nodes in the finite element mesh. Under such assumption the vector I can be easily obtained as follows:

$I = 0$, *for all the nodes which are not for current injection*
$I = Current$, *for the nodes at which current is injected*

7.2.4 Solving the equation in the forward problem

So far, to solve the forward problem, a group of equations have been obtained which can be written as:

$$K U = I \tag{7.11}$$

Here K is the coefficient matrix, U is the potential vector being sought, and I is the current vector for all the nodes.

There are many ways to solve this linear equation group to get the voltage distribution U. One easy way to solve this equation in Matlab, as used by this study, is to calculate the inversion of matrix K, K^{-1}. Then:

$$U = K^{-1} I \tag{7.23}$$

It should be noted that the dimension of matrix K is generally much higher than that in a 2D FEM solver, due to the many more nodes being involved in the 3D mesh. This has greatly increased the requirement of computer resources.

7.3 Image reconstruction algorithm

To solve the inverse problem, the Modified Newton-Rahpson (Gauss-Newton) algorithm was chosen. The 2D version of this algorithm has been detailed in chapter3, therefore a brief description is given of the 3D version due to the similarity.

The algorithm seeks to solve the conductivity distribution $\sigma(x,y,z)$ by minimising the following squared error function:

$$Min \; || F(\sigma) - v_0 ||^2 \tag{7.24}$$

In equation (7.24), F is the function that maps a conductivity distribution σ into a set of boundary voltage measurements, i.e. the forward solver. The forward problem solver is here the FEM solver and forms an integral part of the image reconstruction. v_0 is the real boundary voltage measurements on the electrodes.

In the Gauss-Newton algorithm, the estimation of the conductivity distribution is updated by the following equation:

$$\sigma_{k+1} = \sigma_k + \Delta\sigma_k \tag{7.25}$$

where

$$\Delta\sigma_k = -[[F'(\sigma_k)]^T F'(\sigma_k)]^{-1} [F'(\sigma_k)]^T [F(\sigma_k) - u_0] \tag{7.26}$$

Here F' is the derivative of F with respect to the conductivity distribution σ. In a discrete form, F' is the Jacobian matrix. In this study the Jacobian matrix F' is calculated based on the theorem by Geselowitz [Geselowitz *et al* 1971]:

$$S_{ijk} = -\iiint_{\Omega_k} \nabla u_i \cdot \nabla v_j \, dxdydz \tag{7.27}$$

Here ∇u_i is the potential gradient that is generated within the element Ω_k when a unit current is driven between the ith driving pair electrodes and ∇v_j is the potential gradient which is generated in the same element if a unit current is driven between the jth receiving pair electrodes.

In EIT, the inverse problem is extremely ill-posed, and the discrete form of the problem is ill-conditioned. Therefore regularization has to be used. A typical Tikhonov-regularized version of the EIT inverse problem can be written in the form [Vauhkonen *et al* 1998]:

$$Min \{ || F(\sigma) - v_0||^2 + \alpha||L\sigma||^2 \} \tag{7.28}$$

Where α is the regularization parameter and L is the regularization matrix.

7.4 Sensitivity analysis: a comparative study between two electrode placement configurations

In 3D EIT, two types of electrode placement are generally used, especially for breast imaging. One is the ring placement where layers of rings of electrodes are placed around the object to be imaged [Metherall *et al* 1996][Blue *et al* 2000][Vauhkonen *et al* 1999][Le Hyaric *et al* 2001]. The other is the plane placement where electrodes are placed in a flat plane on the surface of the object to be imaged [Mueller *et al* 2001][Cherepenin *et al* 2001].

The purpose of this study is to compare the 2 different types of electrode placement on the same imaged object in three-dimensional EIT. The long-term goal of this study is to apply three-dimensional EIT to the early detection of breast cancer with an optimal electrode placement strategy. A cylindrical simulation object is made. Sensitivity of different regions within the object is calculated and analysed for the 2 types of electrode placement. The FEM is used to solve the forward problem and three-dimensional images are then reconstructed.

7.4.1 Simulation study

A three-dimensional mesh of a cylindrical shape was made, as shown in Figure 7.2. The size of the cylinder is 0.1167m in height, and 0.2m in diameter. The mesh has 6048 tetrahedrons. The mesh was such that the maximum difference in volume between any 2 tetrahedrons is less than 0.4%. Based on this mesh, a computer simulation object was made, with an initial conductivity distribution shown in Figure 7.3. The simulation object has 16 abnormalities in a uniform background. These 16 abnormalities are distributed in the first 4 layers of the cylinder. Every such layer has 4 abnormalities being located at different position between the boundary and the centre. Based on this mesh the forward problem is solved. For the image reconstruction, another mesh with 2016 pentahedrons was made by

grouping the tetrahedrons of the previous mesh. More specifically, every 3 tetrahedrons are grouped to form a pentahedron.

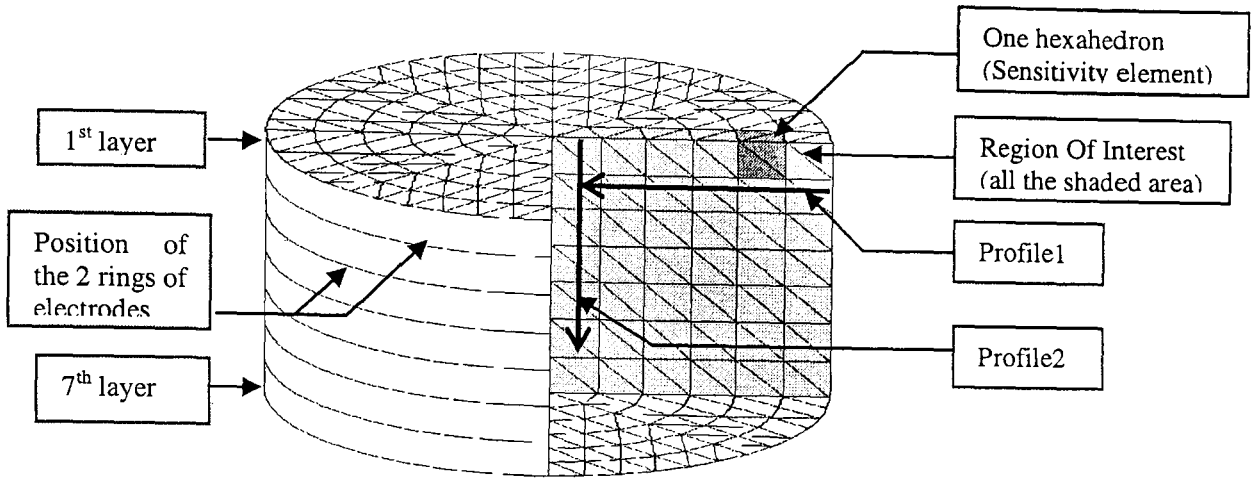

Figure 7.2. The 3D cylindrical mesh

In this study, 48 electrodes are used in total for both current injection and voltage measurements. These electrodes can be arranged in ring placement or plane placement. For the ring placement, 48 electrodes are divided into 2 rings, with 24 electrodes in each ring. The position of the 2 rings is shown in Figure 7.2. For the plane placement, all the 48 electrodes are placed in a flat plane on the top of the cylinder. These configurations are generally used for breast imaging. In three dimensions, there are numerous possibilities for current injection and consequent voltage measurement. In this study, for both electrode placements, we used a similar pattern to the 2D adjacent configuration [Barber *et al* 1984], which is termed the adjacent configuration in 3D. This adjacent configuration not only makes the comparison between the results of the 2 types of electrode placement relatively fair but is consistent with the most current EIT systems that use only pair electrodes for current injection and voltage measurements. The same configuration is used for both current injection and voltage measurement. Figure 7.4(a) shows the configuration for the ring electrode placement, while Figure 7.4(b) shows that for plane electrode placement. So

for both cases, there are a total of 48*48= 2304 measurements in a complete measurement set, although only part of them are independent [Paulson *et al* 1993].

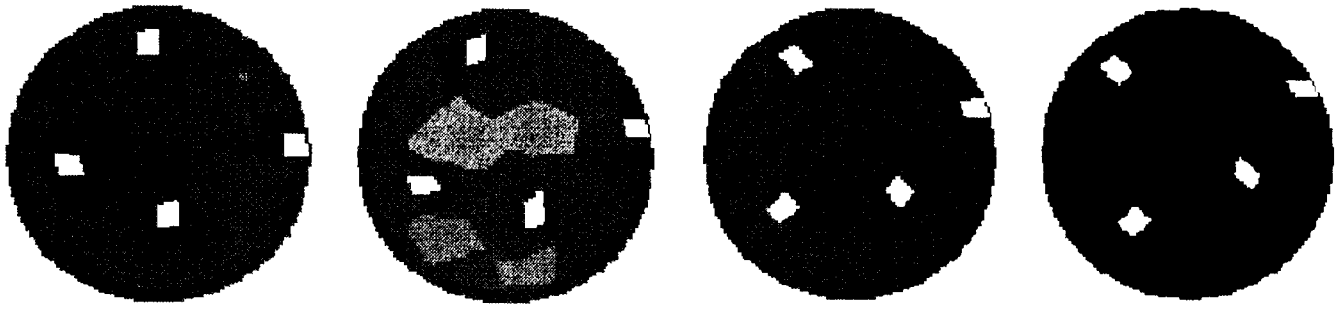

Figure 7.3 The conductivity distribution of the computer simulation object

Background conductivity 0.5 sm^{-1}, all abnormalities: 0.55 sm^{-1}

From left to right: 1st layer, 2nd layer, 3rd layer, 4th layer.

The conductivity distribution for 5th ~7th layers is homogeneous, 0.5sm^{-1}.

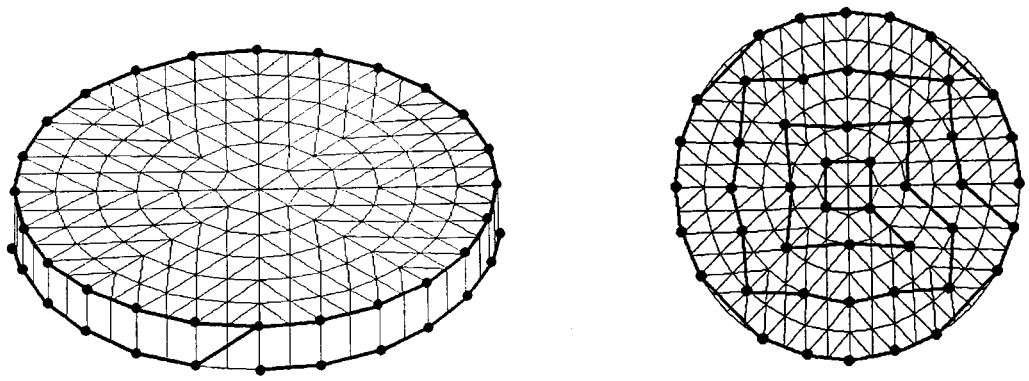

(a) (b)

Figure 7.4 The 2 types of electrode placement and their driving & measuring configurations.

The black points indicate the positions of electrodes; the thick connecting line between any two of the points indicates one driving or measurement on the 2 electrodes.

(a) Ring electrode placement; (b) Plane electrode placement.

The sensitivity distribution in the ROI (shown in Figure 7.2) was calculated and compared between ring and plane electrode placement. The ROI was divided into 6×7=42 hexahedrons each of which was formed by grouping 2 pentahedrons and called a sensitivity element. One such sensitivity element (hexahedron) is shown as the dark shaded area in Figure 7.2. The sensitivity for each hexahedron was calculated by equation (7.26). For a certain current injection and voltage measurement and one sensitivity element, one sensitivity value can be calculated. For all the possible current injection and voltage measurements, a sensitivity element has a vector of 48*48 sensitivity values. In this study the L2 norm of this vector is used as a quantified index for the sensitivity of the corresponding hexahedron. Hereafter this index is termed the "sensitivity" of the sensitivity element.

Images were reconstructed using both ring and plane electrode placements. For image reconstruction, both noise-free and noise-contaminated data were used. In the case of noise-contaminated data, Gaussian noise was directly added on the simulation data. The standard deviation of the noise is 0.1% of the mean value of the simulation data.

As the ill-conditioned problem is very serious in EIT, regularization plays an important role in image reconstruction. To make the comparison between different image reconstruction as fair as possible, the regularization parameter in this study is quoted as the percentage of the biggest singular value of the matrix to be regularized. The choice of the regularization parameter value depends on the noise level in the data. The larger the value of the regularization parameter the more stable the solution but this is at the expense of losing more detailed information. Obviously the choice of a smaller value results in more detailed information in the image but the image is noisier. Choosing the parameter is usually quite empirical and in this study an empirically chosen regularization parameter of α=1.11e-4 is used for the noise-contaminated data and α=1e-8 for the noise-free data.

7.4.2 Results of sensitivity analysis

Sensitivity for ring electrode placement

The sensitivity distribution of the Region Of Interest was calculated by equation (7.26) when the 48 electrodes were arranged in 2 rings around the cylinder. The positions of the 2 rings are shown in Figure 7.2. Figure 7.5 shows the logarithm of the sensitivity distribution in the Region Of Interest. The x coordinate refers to the distance between the centre of sensitivity element and the centre of the corresponding layer.

The following points can be addressed from Figure 7.5.

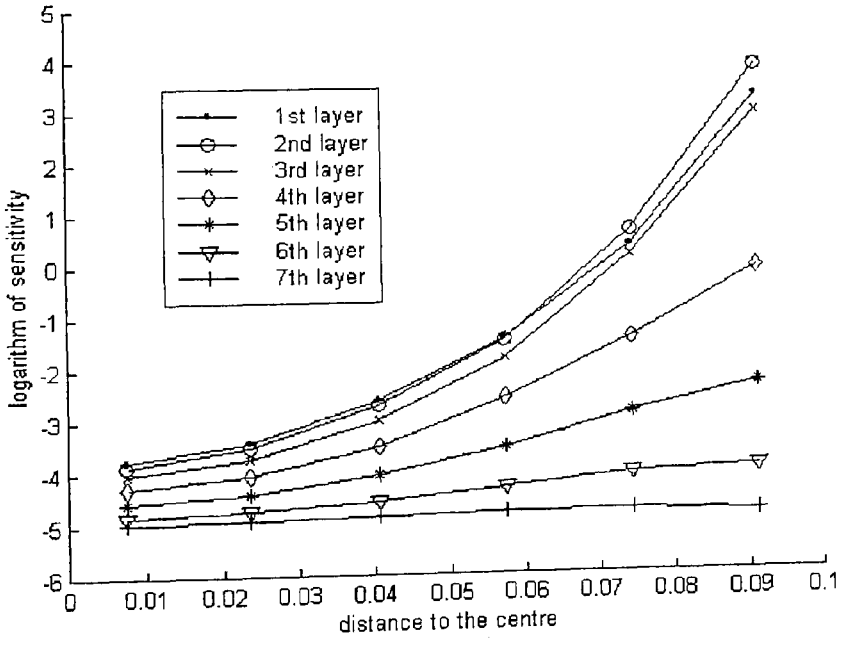

Figure 7.5 Sensitivity distribution for the ring electrode placement

The sensitivity distribution within most layers decreases from the curved boundary of the cylinder to the centre. The nearer the layer is to the electrode planes which are at the both end of the 2nd layer, the more dramatic is the decrease of the sensitivity from the

curved boundary to the centre. For the lowest layer, there is an exception where a small decrease in sensitivity is found near the boundary, which may suggest less current passing through this region.

Overall, the 2nd layer has the largest sensitivity and the sensitivity of the layers decrease as distance to the electrode planes increases. The decrease is more dramatic nearer the boundary. However, for the top layer, there is another exception as the sensitivity near the centre is higher than for the 2nd layer. This is marginal and a possible reason is that the top layer has no upper neighbour and therefore more current is confined in this layer, especially in the centre of this layer and this gives rise to a higher sensitivity in this region.

The detection of a sensitivity element, i.e. a hexahedron like that shown in Figure 7.2, could be extremely difficult when the hexahedron is near the centre of the cylinder. For the layer near the electrode plane, the sensitivity of the central hexahedron is nearly 100000000(1e8) times lower than that of the boundary hexahedron.

Sensitivity for plane electrode placement

The sensitivity distribution of the ROI was also calculated when the 48 electrodes were arranged as a plane on the top of the cylinder. The position of the electrodes was shown in Figure 7.4. Figure7.6 shows the sensitivity distribution in the ROI.

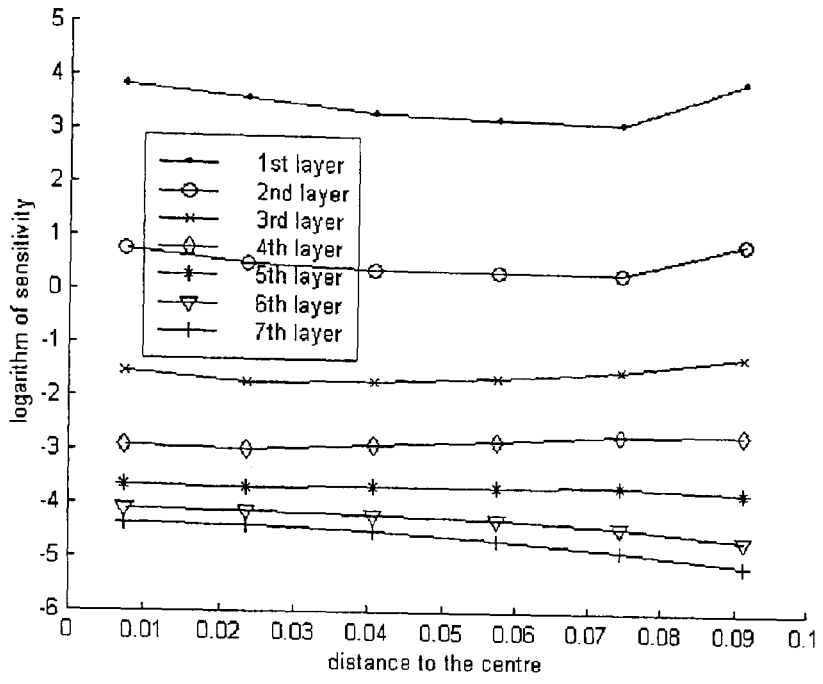

Figure 7.6 Sensitivity distribution for the plane electrode placement

From Figure 7.6 the following points can be addressed:

For each layer, the sensitivity distribution changes slightly from the cylinder centre to the curved boundary. The patterns of change for different layers are slightly different. For the upper 4 layers, sensitivity is higher at both the centre and the boundary than in between. The higher sensitivity in the centre suggests a higher current density in this region. The higher sensitivity on the boundary also suggests a higher current density in this region, which may be caused by the lack of a neighbouring layer on one side. For the lower 3 layers, the sensitivity tends to decrease from the centre to the boundary, which suggests that when the layer is relative far from electrode plane, more current flows in the central area than near the curved boundary. It is also of note that although the electrodes should be evenly distributed in the plane, they are not and this consequently affects the sensitivity distribution.

It is noted that the sensitivity of the layers decreases as the distance to the electrode plane, which is at the top of the cylinder, increases. The sensitivity decrease from one layer to the layer below is more dramatic when the 2 layers are near the electrode plane. For example, the sensitivity decrease from the 1st layer to the 2nd layer is more than that from the 2nd layer to the 3rd layer.

Finally, the detection of a hexahedron in this case could also be extremely difficult when the hexahedron is far from the electrode plane. For the 6th layer, the sensitivity of the central hexahedron is nearly 100000000(1e8) times lower than that in the 1st layer.

Comparison between ring and plane electrode placement

The following Figure 7.7 shows the comparison of the sensitivity between the 2 types of electrode placement. For the ring electrode placement, the sensitivity on "profile 1" in Figure 7.2 was calculated, while for the plane placement, the sensitivity on "profile 2" in Figure 7.2 was calculated.

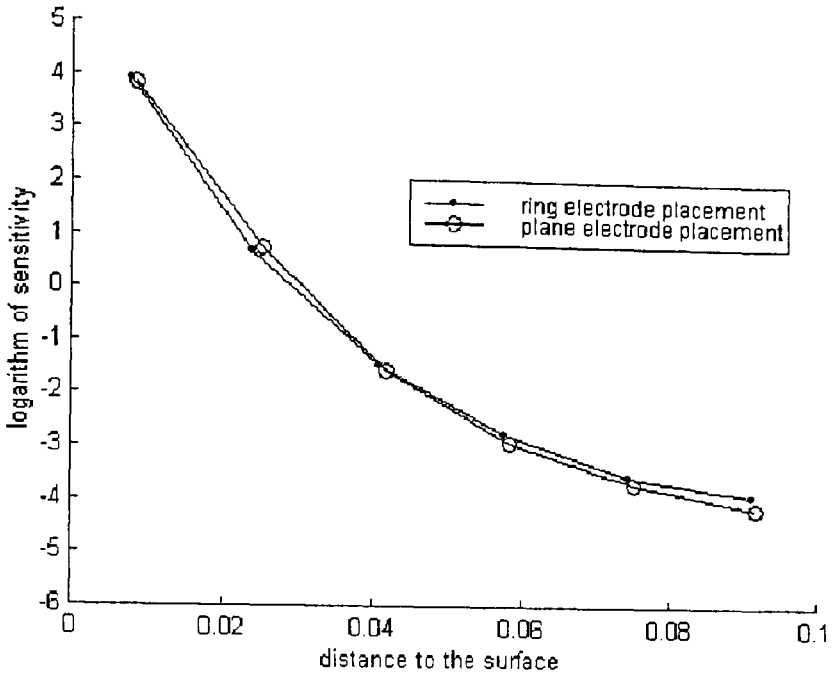

Figure 7.7 The sensitivity comparison between 2 kinds of electrode placement.

The overall sensitivity for both ring and plane electrode placement is at the same level. The two curves shown in Figure 7.7 have the similar shape and position. However, there is one cross point. For ring electrode placement, the position of this point is about 0.04m away from the nearest curved boundary of the cylinder, while for the plane electrode placement, the position is about 0.04m away from the top of the cylinder. Here the "distance to the surface" is used to denote 1) the distance between the point to the nearest curved boundary of the cylinder for ring electrode placement; 2) the distance between the point to the nearest point on the top of the cylinder for plane electrode placement. When the distance to the surface is less than 0.04m, the sensitivity for the plane electrode placement is slightly higher than that for the ring electrode placement. When the distance to the surface is more than 0.04m, the reverse is observed.

7.4.3 Results of image reconstruction

Figure 7.8 shows imaging results for the simulation object shown in Figure 7.3.

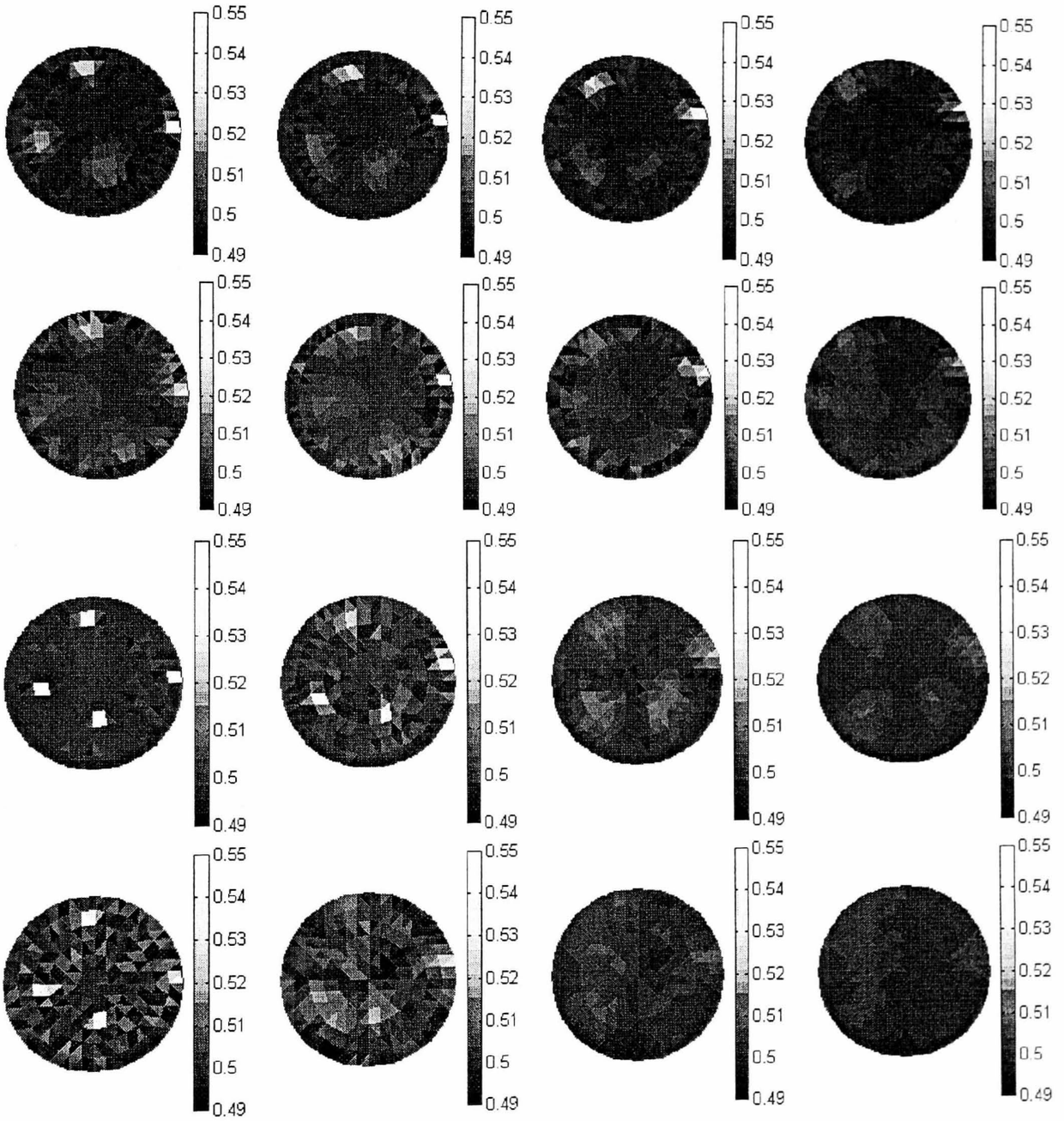

Figure 7.8 Image reconstruction results.
Column from left to right: 1st layer, 2nd layer, 3rd layer, 4th layer. Raw from top to bottom: Ring electrode placement, noise-free data; Ring electrode placement, noisy data; Plane electrode placement, noise-free data; Plane electrode placement, noisy data.

For the reconstructed images with the ring electrode placement, the abnormalities near the curved boundary of the cylinder are more easily detected than those near the centre, and the abnormalities near the electrodes planes (the both ends of 2nd layer) are more easily detected than those far from the electrodes planes. These correspond to the sensitivity analysis carried out.

For the reconstructed images with the plane electrodes placement, the abnormalities near the electrode plane, which is the top of the cylinder, are more easily detected than those far away. For the abnormalities in the same layer but different position, no significant difference has been found in the images. These also correspond to the above sensitivity analysis.

For images with noise-contaminated data, the detectability for the abnormalities far from the electrodes is greatly decreased. From the noisy images in Figure 7.8 it is seen that: 4 abnormalities in the 4th layer cannot be detected with the plane electrodes placement, while the 4 abnormalities near the centre of the cylinder cannot either be detected with the ring electrodes placement.

7.4.4 Discussion and conclusions

The study shows that for both types of the electrode placement, the sensitivity distribution has a similar gradient when the position moves away from the electrodes. However, because of the difference in the electrode placement, the high sensitivity region for each electrode placement has a different shape. This shape should be in parallel with the direction of the electrode array. In this case, for example, for the ring electrode placement, the high sensitivity region covers those areas near the electrode and has a ring shape, while for the plane electrode placement, the high sensitivity region covers those areas near the electrode plane and has a flat cylinder shape.

The sensitivity difference between the high sensitivity area and low sensitivity area is so large that the mathematic approach, such as a better image reconstruction algorithm or an optimal current pattern, has to be combined with an optimal electrode-breast interface to obtain satisfactory images.

Optimal Electrode Placement

With regard to the question: which type of electrode placement is optimal, it seems we have an obvious answer: the electrode placement should be as close as possible to the region of interest.

For breast imaging, because the breast can be easily deformed, to achieve the optimal electrode placement, the following issues should be considered:

1) With the help of mechanical pressure, the region of interest should be as close as possible to the breast surface. This pressure can be achieved by using a rigid flat board (possibly with mounted electrode arrays). However, this need must be a compromise with respect to the discomfort which is imposed on patients;

2) The electrodes should be arranged in such a way that the density of electrodes near the region of interest is as high as possible to achieve best sensitivity.

According to the results in this study, it is also suggested that using EIT to image some organs close to the body surface would be more promising. One such example is the imaging of the prostate.

For the lung and head imaging, it is relatively more difficult, as the Region Of Interest is generally not near the body surface.

Others

It should be noted that the small sensitivity of some region makes the abnormality in this region more difficult to detect. However this does not mean that abnormalities in this region are undetectable. The detectability of an abnormality depends not only on the sensitivity in the region, but also on the size and the conductivity of the abnormality. Abnormality with a larger size and a higher conductivity contrast to the background can be more easily detected.

Many factors that may contribute to the sensitivity are not discussed in the study. These factors include the current injection & voltage measurement patterns and the number and density of the electrodes. A discussion about the number of electrodes can be found in Chapter 4. The value of the study done is to control these factors in the study to be as similar as possible for both electrode placements so that the results can be effectively compared.

It should also be noted that the mesh construct in this study is quite coarse and in the FEM solver linear basis functions were used. This results in numerical errors in the computed results [Vauhkonen *et al* 1999]. Furthermore, the sensitivity is analysed using a rather large element (the hexahedron) and this may also introduce errors into the results.

Conclusions

The following conclusions can be drawn from the study:

1) In EIT there are huge differences in sensitivity between areas near electrodes and areas far from electrodes;

2) The sensitivity difference is so large that the mathematic approach, such as a better image reconstruction algorithm or an optimal current pattern, has to be combined with an optimal electrode-object interface to obtain satisfactory images;

3) The optimal electrode-object interface should be such that high density of electrodes should be placed as close as possible to the region of interest;

4) Applying EIT to imaging breast is more promising due to the fact that the breast is near the body surface and can be easily deformed so that electrodes can be near the region of interest.

7.5 Summary

In this chapter, three-dimensional EIT, including both forward problem and inverse problem, is studied. Then sensitivity distribution for 2 different types of electrode placement is investigated, which serves the long-term goal of applying optimum electrode placement for 3D breast imaging.

The sensitivity study, for the first time in this area, quantitatively disclosed the three-dimensional sensitivity distribution within a cylinder in EIT. It is shown that the sensitivity near the electrodes is much higher than that far from electrodes and the huge difference of sensitivity makes an optimal electrode-breast interface highly desirable if good results are to be obtained. Suggestions are given on the optimal electrode-breast interface for EIM. The study offers vital guidance for designing the next generation of EIM system and is expected to make a significant step forward for the clinical applications of the EIM technique.

CHAPTER 8 CONCLUSIONS AND FUTURE WORK

This chapter concludes the research conducted and provides suggestions for future work.

8.1 Conclusions

The research described in this thesis has been directed at:

1) Investigating methods for improving EIT image quality;

2) Investigating the feasibility of applying EIT in breast cancer detection.

In this thesis the investigation of methods for improving EIT image quality can be concluded from the following aspects:

As a preparation and foundation for subsequent studies, several image reconstruction algorithms were firstly introduced and implemented. Their performance was compared according to the requirement by breast imaging. Results showed that modified N_R algorithm had advantages over other algorithms. This algorithm was therefore chosen as a suitable algorithm for the following study.

In-depth understanding has been gained regarding the effects of two important factors in EIT, the number of electrodes (NOE) and the number of conductivity basis functions (NOCBF), on EIT image reconstruction and resulted image quality. This is achieved by analysing image reconstruction with different combination of NOE and NOCBF using Singular Value Decomposition (SVD) and spectrum expansion theory. Results suggest that under certain conditions, a) Increasing NOE improves condition of the image reconstruction matrix and therefore improves the whole image quality, although image periphery benefits more than image centre; b) Increasing NOCBF helps

little with image quality near the centre; c) For breast imaging, NOE should be as many as possible while NOCBF should be kept in a moderate level. This study provides insights into the effects of these two important factors on EIT image reconstruction and resulted image quality and represents an original contribution in this area.

Another original contribution of this study is that it fully investigated and provided comprehensive insights into compatibility of different types of prior information and its effects on an iterative image reconstruction algorithm. It was shown that incompatible prior information causes significant errors and EIT image reconstruction is sensitive to errors. Therefore the compatibility of prior information can be reflected by the convergence behaviour of iterative image reconstruction using such prior information. A novel method was proposed which utilises this phenomenon, when prior information can be presented in a group of variational forms, to select compatible prior information. The simulation studies have shown the effectiveness of this method by its having successfully pinpointed the most compatible prior information from others regarding boundary shape and peripheral structure of the object. By doing so the image reconstruction quality is greatly improved.

3D EIT techniques are developed consisting of a 3D FEM forward solver and a 3D image reconstruction algorithm, based on which two different electrode placements for a cylindrical object were investigated and compared in terms of sensitivity and image quality. This is to serve the long-term goal of applying optimum electrode placement for 3D breast imaging. Sensitivity analysis indicated that boundary measurements were much more sensitive to impedance changes in the near-electrode region than those regions far from electrodes. The reconstructed images corresponded well to the sensitivity analysis, where high-sensitivity regions had much better image quality than low-sensitivity regions. It can be concluded that in order to gain better sensitivity and image quality of the Region Of Interest (ROI), it is essential to ensure that the electrodes are as close as possible to the ROI. For breast imaging, this can be achieved by an optimal electrode-object interface, by which the breast is deformed with pressure

in a manner to give the best sensitivity to the ROI. The study offers vital guidance for designing the next generation of EIM measurement system and is expected to make a significant step forward for the improvement of EIT image quality and the development of EIM technique.

For the feasibility study of applying EIT to breast imaging, an original contribution of this study is the design of a breast impedance imaging simulation system, which aims at offering useful perspectives and guidelines for real breast imaging. Using this system breast models with different physiological and pathological conditions were made. This was based on the clinical *in vitro* measurements of breast tissue and Cole-Cole modelling. Images with different current frequencies were reconstructed and the ROIs were analysed. Preliminary results indicate that the difference between normal and abnormal tissue with a size of 10 mm in both young and senior women group can be shown in reconstructed images as well as the extracted Cole-Cole parameters, which suggests the potential of using EIM for detection of breast carcinoma.

8.2 Further Work

The studies conducted to date have answered many questions but have also prompted many more. This section identifies areas where further profitable research may be conducted resulting from and building on the progress reported above.

1) Appropriate electrode placement for different applications and corresponding current & voltage patterns;

As suggested by the sensitivity study in Chapter 7, it is important that the electrode placement is such that it gives the best sensitivity of the ROI. The optimal placement should be further investigated according to different applications and different purposes. For breast imaging, research on optimal placement is especially interesting and promising as breasts can be easily deformed so there could be enormous ways of placing electrodes. Another relative study will be to decide the optimal current injection & voltage measurement patterns according to different electrode placements.

2) Incorporating prior information in EIT breast imaging

Prior information can be used to reduce the ill-posedness of the problem and lead the image reconstruction to the real solution. There is yet any systematic report, to the author's knowledge, on how to incorporate different prior information into EIT breast imaging. Further study is needed on methods to obtain and apply anatomically (breast shape and internal structure) as well as physiologically meaningful prior information in EIT breast imaging.

3) A more precise 3D breast forward model;

The precision of the forward model is vital for real imaging. Although some studies have been done in this area, further studies specifically for breast imaging are still needed to improve the precision. These primarily consist of three aspects. Firstly, 3D modelling of the chest & body on which breasts are attached needs to be further studied, as ignoring or wrongly modelling them can cause significant errors

in imaging the breast, even though the chest and body are not of our primary interest. Secondly further studies are needed for 3D modelling of the breast shape for different individuals at the time of imaging. This is because that different people have different breast structure and shape. Even the breast shape of the same person may change at the time of imaging due to the body position and the operator. A way needs to be found to precisely model the imaged breast on the spot. Finally, more studies are needed on modelling the electrode-skin interface. Although the so-called Complete Model was claimed to be the best model for electrode-skin interface, there are still discrepancies between real and predicted measurements. Further study is still needed in this area.

4) An appropriate regularization level

In EIT image reconstruction, a compromise can be obtained between the overall image noise and the fine details of the image by adjusting regularization level. However, no precise recipe for choosing such a regularization level has been discovered which could be used for any problem, although there are some methods being used in different situations. It is therefore very helpful to conduct research on obtaining an appropriate regularization level to reach the said compromise in EIT breast imaging.

REFERENCES

Allers A and Santosa F (1991) Stability and resolution analysis of a linearized problem in electrical impedance tomography *Inverse Probl.* **7**(4) 515-33.

Alveryd A, Andersson I, Aspegren K, Balldin G, Bjurstam N, Edstrom G, Fagerberg G, Glas U, Jarlman O, Larsson SA, Lidbrink E, Lingaas H, Lofgren M, Rudenstam C M, Strender L, Samuelsson L, Tabar L, Taube A, Wallberg H, Akesson P, Hallberg D (1990) Lightscanning versus mammography for the detection of breast cancer in screening and clinical practice: a Swedish multicenter study *Cancer* **65** 1671-77

Assenheimer M, Laver-Moskovitz O, Malonek D, Manor D, Nahaliel U, Nitzan R and Saad A (2001) The T-SCAN (TM) technology: electrical impedance as a diagnostic tool for breast cancer detection *Physiol. Meas.* **22** (1) 1-8

Avill R, Mangnall F, Bird N C, Brown B H, Barber D C, Seagar A D, Johnson A G and Read NW (1987) Applied potential tomography. A new non-invasive technique for measuring gastric emptying *Gastroenterology* **92** 1019-26.

Avis N J and Barber D C (1995) Incorporating A-priori information into the sheffiled filtered backprojection algorithm *Physiol. Meas.* **16** (Suppl. 3A) A111-A122

Barber D C, Brown B H and Freeston I L (1983) Imaging spatial distributions of resistivity using applied potential Tomography *Electronic Letters* **19** 933-35

Barber D C and Brown B H (1984) Applied potential tomography *Journal of Physics* E: Scientific Instruments **17** 723-33.

Barber DC and Seagar AD (1987) Fast reconstruction of resistance images *Clin. Phys. Phys. Meas.* **8**(Suppl A) 47-54

Reference

Barber D C, Brown B H and Avis N J (1992) Image reconstruction in Electrical impedance Tomography using filtered Back-Projection *IEEE EMBS annual conference*, 0-7803-0785-2/92$03.00 1691-92

Bayford R H, Gibson A, Tizzard A, Tidswell T and Holder D S (2001) Solving the forward problem in electrical impedance tomography for the human head using IDEAS (integrated design engineering analysis software), a finite element modelling tool *Physiol. Meas.* **22** (1) 55-64

Bertero M (1998) Introduction to inverse problems in imaging. Bristol, Institute of Physics Publishing ISBN 0750304391

Blue R S, Isaacson D and Newell J C (2000) Real-time three-dimensional electrical impedance imaging *Physiol. Meas.* **21** (1) 15-26

Boas D A, Brooks D H, Miller E L, DiMarzio C A, Kilmer M, Gaudette R J and Zhang Q (2001) Imaging the body with diffuse optical tomography *IEEE Signal Proc. Mag.* **18** (6): 57-75

Borsic A, McLeod C, Lionheart W and Kerrouche N (2001) Realistic 2D human thorax modelling for EIT *Physiol. Meas.* **22** (1): 77-83

Breckon W R and Pidcock M K (1988) Some Mathematical Aspects of Impedance Imaging, Mathematics and Computer Science in Medical Imaging, Ed Viergever and Todd-Pokropek *NATO ASI series F* **39** Springer

Cheney M and Isaacson D (1992) Distinguishability in impedance imaging *IEEE Trans. Biomed. Eng.* **39** 852-60

Reference

Cheney M, Isaacson D and Newell J C (1999) Electrical Impedance Tomography *SIAM Review* **41**(1) 85-101

Cheng K-S, Isaacson D, Newell J C and Gisser D G (1989) Electrode models for electric current computed tomography *IEEE Trans. Biomed. Engr.* **36** 918-24.

Cherepenin, V., Karpov, A., Korjenevsky A., Kornienko V, Mazaletskaya A, Mazourov D and Meister D (2001) A 3D electrical impedance Tomography system for breast cancer detection *Physiol. Meas.* **22**(1) 9-19

Cherepenin VA, Karpov AY, Korjenevsky AV, Kornienko VN, Kultiasov YS, Ochapkin MB, Trochanova OV and Meister JD (2002) Three-dimensional EIT imaging of breast tissues: System design and clinical testing *IEEE Trans. on Med. Imag.* **21** (6) 662-667

Cole K S (1940) Permeability and impermeability of cell membranes for ions. Cold Spring Harbor Symp. *Quant. Biol.* **8** 110-22

Cole K S and Cole R H (1941) Dispersion an absorption in dielectrics *J.Chem.Physics* **9** 341-51

Dobson D C and Santosa F (1994) Resolution and stability analysis of an inverse problem in electrical impedance tomography: Dependence on the input current patterns *SIAM J. Appl. Math.* **54**(6) 1542-60

Edic P M, Isaacson D, Saulnier G J, Jain H and Newell J C (1998) An iterative Newton-Raphson method to solve the inverse admittivity problem *IEEE Trans. on Biomed. Eng.* **45** (7) 899-908

England T S and Sharples N A (1949) Dielectric properties of the human body in the microwave region of the spectrum *Nature*(London) **163** 487

Reference

Epstein S S, Bertell R and Seaman B (2001) Dangers and unreliability of mammography: Breast examination is a safe, effective, and practical alternative *Int. J. Health. Serv.* **31** (3): 605-615

Eyuboglu B M, Brown B H, Barber D C and Seagar A D (1987) Localisation of cardiac related impedance changes in the thorax *Clin. Phys. Phys. Meas.* **8** (Suppl A) 167-73

Foster K R and Schwan H P (1989) Dielectric properties of tissues and biological materials: A critical review *Crit. Rev. Biomed. Eng.* **17** 25-104

Fricke H and Morse S (1926) The electric capacity of tumors of the breast *Journal of Cancer Research* **10** 340

Geselowitz D B (1971) *IEEE Trans. on Biomed. Eng.* **18** 38-41

Gisser D G, Isaacson D and Newell J C (1990) Electric-current computed-tomography and eigenvalues *SIAM J Appl. Math.* **50** (6): 1623-34

Goble J and Isaacson D (1990) Fast reconstruction algorithms for three-dimensional Electrical Impedance Tomography. *Proceeding of annual international conference of IEEE EMBS.* (Philadelphia, USA) **12**100-101

Griffiths H and Ahmed A (1987) Applied potential Tomography for non-invasive temperature mapping in hyperthermia. *Clin. Phys. Phys. Meas.* **8(Suppl. A)** 147-53

Griffiths H and Zheng Z (1989) A Dual-Frequency Electrical Impedance Tomography system. *Phys. Med. Biol.* **34** 1465-76

Hahn G, Sipinkova I, Baisch F and Hellige G (1995) Changes in the thoracic impedance distribution under different ventilatory conditions, *Physiol. Meas.* **16** (Suppl. 3A) A161-73

Reference

Harris N D, Suggett A J, Barber D C and Brown B H (1987) Application of applied potential tomography(APT) in respiratory medicine. *Clin. Phys. Phys. Meas.* **8**(Suppl. A) 155-66

Harris JR, Hellman S, Henderson I C and Kinne D W (1991) *Breast diseases*, 2nd edition, ISBN:0-379-51079-9, J.B. Lippincott Company

Hartov A, Kerner T E, Markova M T, Osterman K S and Paulsen K D (2001) Dartmouth's next generation EIS system: preliminary hardware considerations. *Physiol. Meas.* **22**(1) 25-30

Henderson R P and Webster J G (1978) An impedance camera for spatially specific measurements of the thorax. *IEEE Trans. on Biomed. Eng.* **25** 250-54

Holder D S (Ed) (1993) Clinical and physiological applications of Electrical Impedance Tomography. UCL Press. June ISBN 1-85728-164-0

Isaacson D (1986) Distinguishability of conductivities by electric-current computed-tomography, *IEEE Trans. on Med. Imag.* **5** (2) 91-95

Jain H, Isaacson D, Edic P M and Newell J C (1997) 'Electrical Impedance Tomography of complex conductivity distributions with noncircular boundary' *IEEE Trans.on Biomed.Eng.* **44**(11) 1051-60

Jossinet J (1988) A hardware design for imaging the electrical impedance of the breast. *Clin. Phys. Physiol. Meas.* **9** (Suppl A) 25-8

Reference

Jossinet J and Trillaud C (1991) High frequency imaging of capacitive targets. *IEEE EMBS proceedings of the 13th annual international conference* 18-9.

Jossinet J (1998) The impedivity of freshly excised human breast tissue *Physiol. Meas.* **19** (1) 61-75

Kerner T E, Paulsen K D, Hartov A, Soho S K, Poplack S P (2002), Electrical impedance spectroscopy of the breast: Clinical imaging results in 26 subjects, *IEEE Trans. on Med. Imag.* **21** (6): 638-45

Kopans D B (1998) Breast imaging, 2nd ed. , Philadelphia, Pa. : Lippincott-Raven Publishers, 1998. ISBN: 039751302x

Lamont G L, Wright J W, Evans D F and Kapila L A (1988) An evaluation of applied potential tomography in the diagnosis of infantile hypertrophic pyloric stenosis. *Clin. Phys. Phys. Meas.* **9**(Suppl A) 65-69

Le Hyaric A L and Pidcock M K (2000) A one step image reconstruction algorithm for electrical impedance tomography in three dimensions *Physiol. Meas.* **21** (1) 95-98

Le Hyaric A L and Pidcock M K (2001) An image reconstruction algorithm for three-dimensional electrical impedance Tomography. *IEEE Trans. On Biomed. Eng.* **48**(2) 230-35

Lionheart W R B, Lidgey F J, McLeod C N, Paulson K S, Pidcock M K and Shi Y (1997). Electrical impedance tomography for high speed chest imaging, *Physica. Medica.* **13**(Suppl. 1) 247-49

Lionheart W R B, Kaipio J and McLeod C N (2001) Generalized optimal current patterns and electrical safety in EIT *Physiol. Meas.* **22** (1) 85-90

Reference

Lu L, Brown B H, Barber D C and Leathard A D (1995) A fast parametric modeling algorithm with the powell method *Physiol. Meas.* **16** (Suppl. 3A) A39-A47

McArdle F J, Brown B H, Pearse R G and Barber D C (1988) The effect of the skull of low-birthweight neonates on applied potential tomography imaging of centralised resistivity changes. *Clin. Phys. Phys. Meas.* **9**(Suppl. A) 55-60

Metherall D C, Barber D C, Smallwood R H, and Brown B H (1996) Three-dimensional electrical impedance Tomography *Nature* **380** 509-12

Mitchell A R, and Wait R (1977) The finite element method in partial differential equations. Wiley-Interscience Publication, ISBN 0 471 99405 7

Mueller J L, Isaacson D and Newell J C (1999) A reconstruction algorithm for electrical impedance tomography data collected on rectangular electrode arrays. *IEEE Trans. on Biomed. Eng.* **46**(11) 1379-86

Mueller J L, Isaacson D and Newell J C (2001) Reconstruction of conductivity changes due to ventilation and perfusion from EIT data collected on a rectangular electrode array. *Physiol. Meas.* **22** 97-106

Murphy D, Burton P, Coombs R, Tarassenko L and Rolfe P (1987) Impedance imaging in the newborn. *Clin. Phys. Phys. Meas.* **8**(Suppl. A) 131-40

Newell J C, Blue R S, Isaacson D, Saulnier G J and Ross A S (2002) Phasic three-dimensional impedance imaging of cardiac activity, *Physiol. Meas.* **23**(1) 203-9

Nowakowski A (1995) *Proceeding of the 9th International Conference on Electrical Bioimpedance* 434-35

Osterman K S, Kerner T E, Williams D B, Hartov A, Poplack S P and Paulsen K D (2000) Multifrequency electrical impedance imaging: preliminary in vivo experience in breast. *Physiol. Meas.* **21** (1) 99-109

Ortega J M and Rheinbolt W C (1970) Iterative solutions of nonlinear equations in several variables. New York: academic.

Paulson K, Lionheart W R B and Pidcock M (1993) Optimal experiments in electrical-impedance tomography *IEEE Trans. on Med. Imag.* **12** (4) 681-686

Quinn M, Babb P, Brock A, Kirby L, and Jones J (2001) Cancer Trends in England and Wales 1950-1999: 1950-1999, *National Statistics*, JAN, ISBN: 0116213930

Rao A L, Ti H Q and Holder D S (1996) Imaging of somatosensory and visual evoked responses by electrical impedance tomography in the anaesthetized rabbit *Journal of Physiology-London* **494** 8-9

Sahalos J N, Vlachogiannis E, Koukourlis C, Kyriacou G and Batas K (1992) Electrical impedance measurements for pulmonary disease diagnosis. *Clin. Phys. Phys. Meas.* **13**(Suppl. A) 171-74

Schweiger M and Arridge S R (1999) Optical tomography reconstruction in a complex head model using a priori region boundary information *Phys. Med. and Biol.* **44**(11) 2703-21

Smit H J, Vonk Noordegraaf A, Roeleveld R J, Bronzwaer J G F, Postmus P E, Vries P and Boonstra A (2002) Epoprostenol-induced pulmonary vasodilatation in patients with pulmonary hypertension measured by electrical impedance tomography *Physiol. Meas.* **23**(1) 237-43

Reference

Surowiec A J, Ssuchly S S, Barr J R and Swarup A (1988) Dielectric-properties of breast-carcinoma and the surrounding tissues. *IEEE Trans. on Biomed. Eng.* **35** (4) 257-63

Tang M, Dong X, Qin M, Fu F, Shi X and You F (1998) Electrical impedance tomography reconstruction algorithm based on general inversion theory and finite element method *Med.& Biol. Eng. & Comput.* **36** (4) 395-98

Tang M, Wang W, Wheeler J, McCormick M and Dong X (2002) The number of electrodes and basis functions in EIT image reconstruction *Physiol. Meas.* 23(1) 129-40

Tarassenko L, Rolfe P, Bristow C J and Weindling A M (1984) Use of digital-techniques to process cerebral electrical-impedance signals in the newborn *Med. & Biol. Eng. & Comput.* **22** (1) 55-62

Tidswell A T, Gibson A, Bayford R H and Holder D S (2001) Electrical impedance tomography of human brain activity with a two-dimensional ring of scalp electrodes. *Physiol. Meas.* **22**(1) 167-75

Vauhkonen M, Kaipio J P, Somersalo E and Karjalainen P A (1997) Electrical impedance tomography with basis constraints, *Inverse Probl.* **13** (2) 523-530

Vauhkonen M, Vadasz D, Karjalainen P A, Somersalo E and Kaipio J P (1998) tikhonov regularization and prior information in Electrical Impedance Tomography *IEEE Trans. Med. Img.* **17**(2) 285-93

Vauhkonen M, Lionheart W R B, Heikkinen L M, Vauhkonen P J and Kaipio J P (2001) A MATLAB package for the EIDORS project to reconstruct two-dimensional EIT images *Physiol. Meas.* **22** (1) 107-11

Reference

Vauhkonen P J, Vauhkonen M, Savolainen T and Kaipio J P (1999) Three-dimensional electrical impedance tomography based on the complete electrode model. *IEEE Trans. Biomed. Eng.* **46**(9) 1150-60

Wang W, Tunstall B, Chauhan D and McCormick M (1998) The design of De Montfort Mk2 electrical impedance mammography system IEEE *EMBS 20th Annual International Conference (HK)*

Wang W, Tang M, McCormick M and Dong X (2001) Preliminary results from an EIT breast imaging simulation system *Physiol. Meas.* **22** (1) 39-48

Watkins D (1991) Fundamentals of matrix computations ISBN 0-471-54601-1

Wheeler J, Wang W and Tang M (2002) A comparison of methods for measurement of spatial resolution in two-dimensional circular EIT images *Physiol. Meas.* **23**(1) 169-76

Wilson A J, Milnes P, Waterworth A R, Smallwood R H and Brown B H (2001) Mk3.5: a modular, multi-frequency successor to the Mk3a EIS/EIT system. *Physiol. Meas.* **22** (1) 49-54

Yorkey T J, Webster J G and Tompkins W J (1987) Comparing reconstruction algorithms for electrical impedance tomography. *IEEE Trans. on Biomed. Eng.* **34**(11) 843-52

Zadehkoochak M, Blott B H, Hames T K and George R F (1991) Spectral expansion analysis in electrical impedance tomography *J. Phys. D: appl. Phys.* **24** 1911-16

Appendix A: Publication list during PhD study

1. **Tang M**, Wang W, Wheeler J, McCormick M and Dong X (2002) Effects of incompatible boundary information in EIT on the convergence behaviour of an iterative algorithm ***IEEE Transaction On Medical Imaging*** 21(6) 620-28

2. **Tang M**, Wang W, McCormick M, Wheeler J and Dong X (2002) The number of electrodes and basis functions in EIT image reconstruction ***Physiological Measurement*** ***(IoP)*** 23(1) 129-40

3. Wheeler J, Wang W and **Tang M** (2002) A comparison of methods for measurement of spatial resolution in two-dimensional circular EIT images ***Physiological Measurement*** ***(IoP)*** 23(1) 169-76

4. Wang W, **Tang M**, McCormick M and X Dong (2001) Preliminary results from an EIT breast imaging simulation system ***Physiological Measurement*** ***(IoP)*** 22 (1) 39-48

5. **Tang M** and Wang W (2002) Determination of optimal regularization level in Electrical Impedance Tomography *2nd European Medical & biological Engineering Conference*, Dec 04-08 Vienna Austria (Accepted for Oral presentation)

6. **Tang M**, Wang W, Dong X, Qin M, Wheeler J and McCormick M (2001) Incorporating more compatible prior information into the image in Electrical Impedance tomography, *Proceedings of XI international conference on electrical bio-impedance* June 17~21 Oslo Norway (Oral presentation)

7. Wheeler J, Wang W and **Tang M** (2001) A new method for measurement of spatial resolution in EIT *Proceedings of XI nternational conference on electrical bio-impedance*, June 17~21 Oslo Norway

8. **Tang M**, Wang W, Dong X, Wheeler J and McCormick M (2001) Two factors in EIT image reconstruction. *Proceedings of the 3rd EPSRC engineering network meeting* April 4th ~6th UCL London, (Oral presentation)

9. **Tang M**, W Wang, X Dong, J Wheeler, M McCormick, A breast imaging simulation system, 2nd EPSRC engineering network meeting, April 4th ~6th 2000, UCL, London, (Oral presentation)